Journal of
Materials Chemistry A

REVIEW

View Article Online
View Journal | View Issue

Cite this: J. Mater. Chem. A, 2019, 7, 21036

Inorganic perovskite solar cells: an emerging member of the photovoltaic community

Jialong Duan,[a] Hongzhe Xu,[a] W. E. I. Sha,[b] Yuanyuan Zhao,[a] Yudi Wang,[a] Xiya Yang[a] and Qunwei Tang*[a]

Received 24th June 2019
Accepted 30th August 2019

DOI: 10.1039/c9ta06674h

rsc.li/materials-a

Perovskite solar cells (PSCs) have attracted tremendous interest because of their rapid improvement in power conversion efficiency (PCE) from the initial PCE of 3.8% for the first prototype to the certified PCE of 25.2% in 2019. However, the inherent chemical instability of organic–inorganic hybrid perovskite halides influenced by moisture, heat and ultraviolet light is still a critical issue for them to meet application-specific requirements owing to the weak-bonded organic components in the hybrid crystal structure. The use of all-inorganic perovskites $CsPbI_{3-x}Br_x$ ($x = 0$, 1, 2, and 3) as light-harvesters by completely substituting organic species with inorganic Cs^+ ions has been recently regarded as a promising solar conversion technology. Since the initial efficiency of 2.9% achieved in 2015, the highest PCE record for inorganic PSCs has risen to 18.4% through structure optimization, compositional engineering, interfacial engineering, solvent control and surface passivation, *etc*. This article is dedicated to providing an up-to-date review on the development of inorganic PSCs tailored by various inorganic perovskite materials with gradually changed optical properties and stability, as well as the film-making methods and interfacial engineering technologies. Their limited efficiencies in theory and recombination mechanisms are also predicted with a detailed balance model. Finally, we focused on the state-of-the-art strategies for enhancing the photovoltaic performance and identified new challenges and outlooks for future studies in this field.

1. Introduction

Solar radiation releases enormous solar energy, accounting for almost 99% of the total energy in the earth. Therefore, the harvesting of solar energy by energy-conversion devices (*i.e.*, photovoltaics or solar cells) is regarded as a promising solution to address the energy and environmental problems. It has been always a hot topic to convert solar energy into electricity by complicated photoelectrical or photoelectrochemical principles since the discovery of the first solar panel in 1954.[1,2] To date, photovoltaics can be divided into three categories according to the photovoltaic materials: (i) crystalline silicon solar cells, (ii) thin-film technologies, and (iii) the emerging solar cells. As emerging photovoltaics in recent decades, dye-sensitized solar cells (DSSCs),[3–10] organic solar cells (OSCs),[11–22] quantum dot-sensitized solar cells (QDSCs),[23–30] and perovskite solar cells (PSCs)[31–37] are regarded as promising candidates due to their remarkable power conversion efficiency (PCE) enhancement and low production costs. Since 2009, organic–inorganic hybrid perovskite light-harvesters have been well-studied in theory, experiment and module production, and the corresponding PSCs have seen a rapid rise in PCE from 3.8% to 25.2% within ten years.[38–47] These hybrid PSCs are always highlighted by some superiorities: (1) the bandgap of $CH_3NH_3PbI_3$ ($MAPbI_3$, 1.55 eV) or $CH(NH_2)_2PbI_3$ ($FAPbI_3$, 1.43 eV) is highly suited for wide-spectral photovoltaics;[48,49] (2) the hybrid perovskites present high extinction coefficient and incident-photon-to-current conversion efficiency (IPCE) in devices;[40] (3) the carrier diffusion length is long in perovskite films.[50,51] *Science Daily* said "There is now an urgent need to tackle the threat of climate change resulting from humanity's overreliance on fossil fuel, and the rapid development of new solar technologies must be part of the plan." Large area, improved stability, high efficiency, and good reproducibility are the critical competitive elements to assess the commercial application of PSCs. Although the state-of-the-art organic–inorganic hybrid PSCs have comparable PCEs to silicon solar cells, organic–inorganic hybrid perovskite films generally suffer from compositional degradation and crystallization destruction under persistent attack by heat, moisture, or ultraviolet (UV) light,[52,53] mainly arising from the inherent instability of organic volatile components, such as MA^+ and FA^+, in thermal and UV conditions. Furthermore, organic MA^+ and FA^+ species are prone to react with water molecules or under sunlight and thermal conditions to form intermediate hydrates, which can lead to serious perovskite degradation and therefore poor device lifetime.[54–57]

---

[a] *Institute of New Energy Technology, College of Information Science and Technology, Jinan University, Guangzhou 510632, PR China. E-mail: tangqunwei@jnu.edu.cn*

[b] *Key Laboratory of Micro-nano Electronic Devices and Smart Systems of Zhejiang Province, College of Information Science and Electronic Engineering, Zhejiang University, Hangzhou, China*

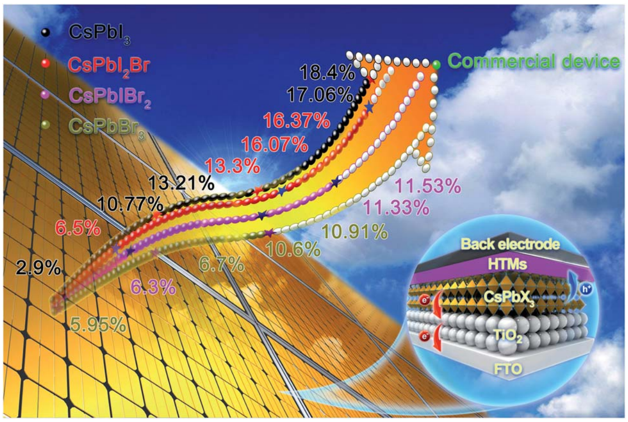

Fig. 1 The best efficiencies for various inorganic PSCs.

In recent works, the substitution of organic counterparts with inorganic cesium cations (Cs^+) is considered an effective approach to improve the environmental tolerance of perovskite films under harsh conditions.[58,59] Full-cesium perovskites have been demonstrated to possess high hole mobility ($\sim$520 cm^2 V s^{-1}) and electron mobility ($\sim$530 cm^2 V s^{-1}) when obtained from the cold-pressed pellets of annealed $CsSnI_3$ polycrystalline material, while an electron lifetime of 2.5 μs and an estimated electron mobility of $\sim$1000 cm^2 V s^{-1} were obtained for $CsPbBr_3$ halide single-crystals.[60,61] Based on these properties, it can be predicted that inorganic perovskites may be another candidate as a light absorber. Since the initial report for fully inorganic cesium lead halides in 1893 and subsequent systematic studies in this field,[62–69] these perovskite halides have been successfully assembled into inorganic PSCs in 2015. To date, enormous efforts have been made to advance the PCE of inorganic devices, Fig. 1 plots the maximized PCEs of inorganic PSCs with $CsPbI_3$, $CsPbI_2Br$, $CsPbIBr_2$, or $CsPbBr_3$ as light absorbers, where the initial PCEs are all lower than 5% but the maximized value to date is more than 18%, thus demonstrating the great potential for their application in the future. In this review, we summarize the recent advances of all-inorganic PSCs by emphasizing their structural phase transformation, tunable optoelectronic properties, environmental stability, film-making methods, interfacial engineering, and their limited efficiency, as well as the challenges still faced by scientists and their future outlooks.

2. Fundamental background

2.1 Crystal structures of inorganic perovskites

The chemical formula ABX_3 [A (+1), B (+2), X (−1)] is always designated for perovskite-structured materials with a similar crystal structure to the mineral $CaTiO_3$. The recently emerging all-inorganic perovskites can also be described by a similar chemical formula $CsMX_3$ ($M = Pb^{2+}$ or Sn^{2+}, $X = I^-$ or Br^-), where Cs^+ occupies a corner of a unit cell with 12-fold coordination, M is a divalent metal cation in general sitting in a body-centered position with 6-fold coordination, and X is a halogen with a face-centred position, as depicted in Fig. 2.[70]

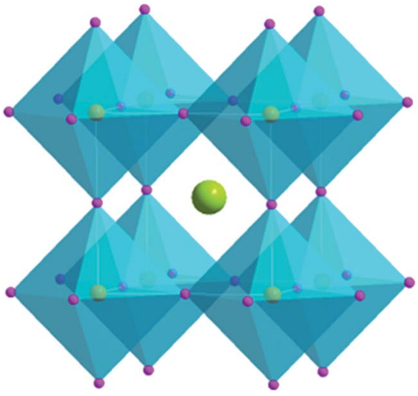

Fig. 2 Unit cell structure of an inorganic $CsMX_3$ perovskite.[70]

There is a lower energy barrier for the intercalation of CsX into $PbBr_2$ frameworks during perovskite formation,[71] arising from the smaller ionic radius of Cs^+ (1.81 Å for Cs^+) than 2.70 Å for MA^+ and 2.79 Å for FA^+. The crystal structure of the perovskite is adjustable in terms of its composition by controlling the tolerance factor (t) and octahedral factor (μ), as proposed by Goldschmidt, in a rational range. Here, t indicates the state of distortion and stability of perovskite structures, and this value can be obtained according to the following formula:[72] $t = (r_A + r_X)/\sqrt{2}(r_B + r_X)$, where r represents the ionic radius of atoms of A, B, and X sites, respectively, μ is defined as a r_B/r_X ratio, which is directly correlated to the formation of a BX_6 octahedron.[25,73,74] Both t and μ are used to predict the formability of a perovskite structure. Typically, stable 3D halide perovskite crystals can be formed under the condition of $0.81 < t < 1.0$ and $0.44 < \mu < 0.90$, an ideal cubic perovskite structure at $0.9 < t < 1.0$, and a tetragonal or orthorhombic structure in the range of $0.81 < t < 0.9$, respectively.[75,76] When $t > 1.0$, a NH_4CdI_3-type crystal structure is usually favored. When $t < 0.8$, a $CsNiBr_3$-type crystal structure is most likely to form.[77] Taking the crystal restrictions, such as the t range and ionic radius of the commonly used Pb^{2+} (1.2 Å), Br^- (1.96 Å) and I^- (2.2 Å) ions into considerations, the ionic radius of the A-site ion should be limited to 2.9 Å. Otherwise, the cubic structure will be distorted and the crystal symmetry will be reduced, leading to forming an unsatisfactory crystal with notorious photovoltaic performance or long-term stability. So the inorganic cations with Cs^+ or Rb^+ cations could lead to a more favorable tolerance factor to facilitate the stabilization of the photoactive perovskite phase in a broader temperature range and to improve their thermal and light soaking stability.

2.2 Stability of inorganic perovskites

The degradation mechanisms of organic–inorganic hybrid perovskites have been widely explored during the past several years. Organic cations, such as MA^+ in $MAPbI_3$, have acidic protons; therefore, the perovskite degradation will be initiated by the reaction between the superoxide and methylammonium moiety under light and oxygen conditions.[78] In this fashion, the use of all-inorganic perovskites free of organic species can improve the tolerance of the perovskite crystal to oxygen and light. Unfortunately, such inorganic perovskites have been demonstrated to be not stable enough under external stimuli, such as moisture, light, heat, and oxygen. To the best of our knowledge, $CsPbBr_3$ has the most superior stability among the different inorganic perovskites, while the I-containing perovskites display inferior long-term stability. Different from hybrid perovskites, the inorganic perovskites are free of hygroscopic organic cations, which are responsible for the hydration-induced degradation. Therefore, polymorphic transition, decomposition, oxidation, or their combinations may be the intrinsic origins of their instability properties.[77] For the state-of-the-art $CsPbI_3$ inorganic perovskite, the phase instability is mainly due to transitions between the desirable photoactive perovskite black phase and the undesirable non-perovskite yellow phase, although transition to the yellow phase is reversible, attributed to the undesirable tolerance factor. Although the polymorphic transition can be significantly suppressed *via* increasing the Br dosage (producing a more stabilized structure with $t > 0.8$ and $\mu > 0.4$), halide segregation may be another issue for the performance degradation under light or an electron beam, especially for perovskites with an I dosage lower than 40%. Based on the above-mentioned discussion, it can be seen that the phase instability of $CsPbX_3$ can be mainly attributed to the polymorphic transition. There are also other inorganic perovskite materials, such as $CsSnX_3$ and $CsGeX_3$, where the facile oxidation of Sn^{2+}/Ge^{2+} to Sn^{4+}/Ge^{4+} in ambient air results in a sluggish efficiency and rapid performance degradation, which will be discussed in the following part.

2.3 Inorganic PSC architectures

Similar to hybrid PSCs, the state-of-the-art all-inorganic devices are generally constructed in a regular n–i–p or inverted p–i–n architectures, as shown in Fig. 3a and c, in which both perovskite layers are sandwiched between an n-type electron-transporting layer (ETL) and a p-type hole-transporting layer (HTL). A mesoporous scaffold, either semiconducting or insulating, is also generally included, as shown in Fig. 3b. In physics, the light absorption of a perovskite is a light–matter interaction process, in which the electrons in the interacting materials resonate with the electric field of the irradiating optical signal and induce polarization. The working principle of a typical PSC is based on the photovoltaic effect of a p–n junction, and the built-in potential is formed at p–n junctions. Upon sunlight irradiation, the atoms in an inorganic perovskite absorb photons to release electrons and subsequently generate electron–hole pairs. The photo-induced electrons are driven to an n-type region and holes are driven to a p-type region under this barrier electric field, and therefore, a photogenerated electric field opposite to the direction of the barrier electric field is formed near p–n junctions. Part of the photogenerated electric field counteracts the barrier electric field and the rest causes electromotive force in the thin layer between the n-type and p-type regions to realize electric power output through an external circuit. In this fashion, the intrinsic mechanism for regular n–i–p or inverted p–i–n architectures is identical except for the charge-carrier transfer direction.

Considering the morphology of a transparent conductive oxide (TCO)-attached charge-contact layer, a mesoporous or planar architecture can be visibly distinguished. To date, both structured PSCs have achieved a high efficiency over 20% based on a hybrid perovskite layer, demonstrating great potential in real application.[79,80] The choice of whether to fabricate a mesoporous or planar architecture is highly dependent on the perovskite film quality and properties. For mesoporous PSCs derived from dye-sensitized solar cells,[81] the perovskite layer can be infiltrated within the scaffold *via* the interconnected channels, resulting in a facile and reproducible device fabrication.[82,83a,b] The concept of a planar device originates from TiO_2- or Al_2O_3-based mesoporous PSCs.[43] In detail, a planar architecture is implemented on a compact charge-transfer layer without pores, on which it is more facile to deposit a perovskite film through vapor-based technologies, which will be discussed in Section 5. Compared to mesoporous devices, the high-quality and smoother perovskite layer plays an important role in obtaining a satisfactory solar-to-electric conversion efficiency. In fact, a much higher photocurrent or photovoltage can be realized based on a planar architecture, but it will suffer from much worse hysteresis, which may arise from insufficient charge extraction rates, therefore leading to charge accumulation.

3. Inorganic perovskites solar cells

Are organic cations essential for high-efficiency PSCs? This urgent question was analyzed by Hodes and Snaith in 2015, although the first report on inorganic $CsPbX_3$ crystal data can be

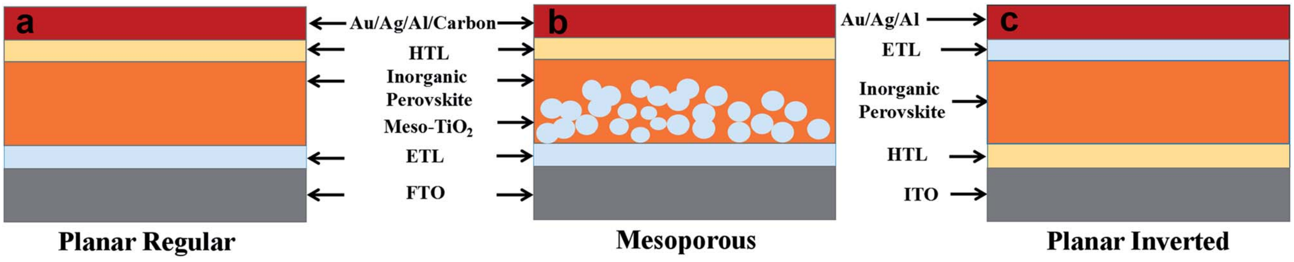

Fig. 3 Device structures of typical PSCs.

traced back to 1893.[62,84,85] Hodes *et al.* demonstrated that the organic cations are not indispensable for high open-circuit voltage (V_{oc}) PSCs through comparing hybrid organic–inorganic methylammonium lead bromide ($MAPbBr_3$) and all-inorganic cesium lead bromide ($CsPbBr_3$) with different HTLs.[84] Through identifying the possible fundamental differences in their structural, thermal, and electronic characteristics, they found that a large V_{oc} profits from the presence of a direct optical bandgap of around 2.3 eV. Simultaneously, the $CsPbBr_3$ halide had higher thermal stability than $MAPbBr_3$. However, its large bandgap limited the PCE enhancement of this type of device. Snaith and co-workers fabricated a $CsPbI_3$-based PSC for the first time *via* a low-temperature phase transition process at room temperature, achieving a PCE of 2.9%.[85] Those works identify that the organic cation is not necessary and this paved the way for further developments of much more thermally stable inorganic perovskites as light absorbers. In this section, the state-of-the-art advances of all-inorganic PSCs engineered from compositional, doping, interfacial, and spectral aspects are systematically demonstrated, and the photovoltaic parameters of typical devices based on various inorganic perovskites are summarized in Table 1.

3.1 Pb-based perovskites

$CsPbX_3$ (X = Br, I, with stoichiometric ratios of 0 : 3, 1 : 2, 2 : 1, and 3 : 0) materials can generally form a cubic phase perovskite structure with intrinsic Goldschmidt's values for the tolerance factor $t = 0.83–0.84$. Inorganic perovskites possess ambipolar behaviors, accompanying unique crystal structures, high absorption coefficients, large exciton diffusion lengths, and excellent charge-transporting properties, indicating that they can cumulatively work as light absorbers and carrier conductors.[145] According to the above-mentioned properties, perovskite films with a thickness of several hundreds of nanometers are enough to realize efficient solar-to-electric conversion.[146–148] $CsPbBr_3$- and $CsPbI_3$-based solar cell models are two types of devices that were first fabricated in the early stage of all-inorganic PSCs development. However, $CsPbBr_3$ is limited by its narrow absorption range and $CsPbI_3$ has thermodynamic phase instability in high-humidity (even in low temperature with zero humidity) and/or high-temperature conditions. To pursue a long-time prosperity for devices, scientists pay great attention and made many innovations to try to overcome these weakness, including tuning the Br : I ratio and doping foreign elements by compositional engineering to modulate the crystal structure, absorption range, and durability.[111,149,150] These findings have led to the further exploration of many new configurations and derivative materials for $CsPbX_3$.[149,151] Fig. 4a shows the absorption spectra evolution of $CsPbI_{3-x}Br_x$ perovskites with various Br dosages, referring to an absorbance onset changing from 540 nm for $CsPbBr_3$ to 718 nm for $CsPbI_3$.[111] In detail, there is a linear relationship between the absorption onset values and Br concentration in inorganic perovskites, as shown in Fig. 4b. In this fashion, the light-harvesting ability of $CsPbI_{3-x}Br_x$ perovskite can be precisely predicted, giving a possibility to obtain an ideal inorganic perovskite material with considerable long-term stability and photovoltaic properties. To date, $CsPbI_3$, $CsPbI_2Br$, $CsPbIBr_2$, and $CsPbBr_3$ films are the main four types of state-of-the-art inorganic perovskites and their Shockley–Queisser (S–Q) limit efficiencies are 28.9%, 24.4%, 22.1%, and 15.9% in photovoltaic devices, respectively. As shown in Fig. 4c, all the perovskites can form a typical perovskite phase with diffraction peaks at around 14.62°, 20.65°, and 28.94°, corresponding to the (100), (110), and (200) planes, respectively. These characteristic peaks shift to higher angles with increasing the Br dosage owing to the contraction of the crystal lattice upon the partial substitution of I atoms with Br atoms. From the external quantum efficiency (EQE) characterizations (Fig. 4d), it can be seen that the light response range can be extended to 620 nm (2.05 eV for $CsPbIBr_2$), 700 nm (1.9 eV for $CsPbI_2Br$), and then 740 nm (1.73 eV for $CsPbI_3$) from 540 nm (2.3 eV for $CsPbBr_3$), in accordance with the absorption spectra. It should be noted that the high trap-state density from the thermal dynamical instability of the black α-$CsPbI_3$ perovskite phase to the δ-$CsPbI_3$ non-perovskite phase delivers the lowest PCE and EQE values in the early stage.[111]

A high PCE and improved stability are equally significant to promote the commercialization of all-inorganic PSCs. However, the light-harvesting ability and their tolerance to the environment of these inorganic perovskites in ambient conditions is dramatically adverse. As shown in Fig. 4e, the normalized photovoltaic performance of the corresponding device degrades significantly following the order of $CsPbI_3$ > $CsPbI_2Br$ > $CsPbIBr_2$ > $CsPbBr_3$, demonstrating the incompatible power out ability and long-term stability. While $CsPbBr_3$ perovskite is relatively stable without changes in either color or shape in 40% RH and 25 °C over 3 h as shown in Fig. 4f, $CsPbIBr_2$, $CsPbI_2Br$, and $CsPbI_3$ present rapid decomposition by moisture attack. Therefore, how to simultaneously compromise the light-harvesting ability and stability is a great challenge in the field of inorganic PSCs.

To better understand the properties of light absorbers, which is crucial for the fabrication of high-performance inorganic PSCs, we summarize various Pb-based inorganic perovskite materials that have been used as photoactive layers in this section.

3.1.1 $CsPbBr_3$. Early work on $CsPbBr_3$, which presents an orthorhombic phase at room temperature and transforms to a tetragonal phase at 88 °C and to the "orange" cubic perovskite phase at 130 °C, was pioneered by Wells in 1893,[62] but did not attract much more concerns until the early 21st century. Its estimated electron mobility was reported to be as high as $\sim$1000 $cm^2\ V\ s^{-1}$ with an electron lifetime of 2.5 μs,[61] which were also cross-checked by Ghosh.[152] From those excellent parameters, it is clear that the charge carrier within $CsPbBr_3$ has great potential to obtain long diffusion or drift lengths to ensure a sufficient thickness of perovskite film to suit photovoltaic devices.

One of the outstanding properties of inorganic $CsPbBr_3$-based PSCs is their high open-circuit voltage owing to possessing a semiconductor bandgap of 2.3 eV (optical absorption range of 300–540 nm), as shown in Fig. 5a. Hodes *et al.* employed $CsPbBr_3$ as a light harvester to fabricate a typical

Table 1 Summary of device performances for various inorganic PSCs

Formula	Device structures	PCE	Operation conditions	Ref.
$CsPbBr_3$	FTO/m-TiO_2/$CsPbBr_3$/Au	5.47%	Ambient	**84**
	FTO/m-TiO_2/$CsPbBr_3$/Spiro-OMeTAD/Au	4.98%	Ambient	**84**
	FTO/m-TiO_2/$CsPbBr_3$/CBP/Au	4.92%	Ambient	**84**
	FTO/m-TiO_2/$CsPbBr_3$/PTAA/Au	5.72%	Ambient	**84**
	FTO/m-TiO_2/$CsPbBr_3$/C	5.0%	Ambient	**86**
	FTO/c-TiO_2/m-TiO_2/$CsPbBr_3$/C	5.38%	Ambient	**87**
	FTO/c-TiO_2/m-TiO_2/$CsPbBr_3$/C	6.7%	Ambient	**88**
	FTO/c-TiO_2/m-TiO_2/GQDs/$CsPbBr_3$/C	9.72%	Ambient	**89**
	FTO/c-TiO_2/m-TiO_2/$Cs_{0.91}Rb_{0.09}PbBr_3$/C	9.86%	Ambient	**90**
	FTO/c-TiO_2/m-TiO_2/CQDs/$CsPbBr_3$/C	7.86%	Ambient	**91**
	FTO/c-TiO_2/m-TiO_2/$CsPbBr_3$/$CuInS_2$–ZnS QDs/C	8.42%	Ambient	**92**
	FTO/c-TiO_2/m-TiO_2/CQDs/$CsPbBr_3$/PQDs/C	7.93%	Ambient	**93**
	FTO/c-TiO_2/m-TiO_2/CQDs/$CsPbBr_3$/RPQDs/C	8.2%	Ambient	**94**
	FTO/c-TiO_2/m-TiO_2/$CsPbBr_3$/$CsSnBr_{3-x}I_x$ QDs/C	9.13%	Ambient	**95**
	FTO/c-TiO_2/m-TiO_2/$CsPbBr_3$–$CsPb_2Br_5$/Spiro-OMeTAD/Ag	8.36%	Ambient	**96**
	FTO/c-TiO_2/m-TiO_2/$CsPb_{0.97}Sm_{0.03}Br_3$/carbon	10.14%	Ambient	**97**
	FTO/TiO_2/$CsPbBr_3$/MoS_2/carbon	6.8%	Ambient	**98**
	FTO/c-TiO_2/m-TiO_2/$CsPbBr_3$/$CsMBr_3$/C	10.6%	Ambient	**99**
	FTO/c-TiO_2/m-TiO_2/$CsPbBr_3$/ZnS:SnS/C	10.26%	Ambient	**100**
	FTO/c-TiO_2/$CsPbBr_3$/$CsPbBr_3$–$CsPb_2Br_5$/$CsPbBr_3$–Cs_4PbBr_6/carbon	10.17%	Ambient	**101**
	FTO/c-TiO_2/m-TiO_2/$CsPbBr_3$/MnS/C	10.45%	Ambient	**102**
	FTO/c-TiO_2/$CsPbBr_3$/Spiro-OMeTAD/Ag	10.91%	Ambient	**103**
$CsPbIBr_2$	FTO/m-TiO_2/$CsPbIBr_2$/Au	4.7%	Glovebox	**104**
	FTO/bl-TiO_2/mp-TiO_2/$CsPbIBr_2$/Spiro-OMeTAD/Au	6.3%	Ambient	**105**
	FTO/NiO_x/$CsPbIBr_2$/MoO_x/Au	5.52%	N_2	**106**
	FTO/c-TiO_2/m-TiO_2/$CsPbIBr_2$/C	8.25%	Ambient	**70**
	FTO/c-TiO_2/m-TiO_2/$CsPb_{0.9}Sn_{0.1}IBr_2$/C	11.33%	Ambient	**70**
	ITO/SnO_2/$CsPbIBr_2$/Spiro-OMeTAD/Ag	9.68%	Ambient	**107**
	FTO/TiO_2/CsBr/$CsPbIBr_2$/C	10.71%	Ambient	**108**
	ITO/SnO_2/C60/$CsPb_{1-x}Sn_xIBr_2$/Spiro-OMeTAD/Au	11.53%	Glovebox	**109**
$CsPbI_2Br$	ITO/SnO_2/$CsPbI_2Br$/PTAA/MoO_3/Al	13.8%	N_2	**110**
	FTO/c-TiO_2/$CsPbI_2Br$/Spiro-OMeTAD/Ag	10.99%	N_2	**111**
	FTO/c-TiO_2/$CsPbI_2Br$/Spiro:Li-TFSi-tBP/Ag	10.3%	N_2	**112**
	FTO/c-TiO_2/m-TiO_2/$CsPb_{0.98}Sr_{0.02}I_2Br$/P3HT/Au	11.3%	N_2	**113**
	FTO/bl-TiO_2/$Cs_{0.925}K_{0.075}PbI_2Br$/Spiro:Li-TFSi-tBP/Au	10.0%	20 °C, RH < 20%	**114**
	ITO/Ca/C_{60}/$CsPbI_2Br$/TAPC/TAPC:MoO_3/Ag	11.8%	Vacuum	**115**
	FTO/TiO_2/$CsPb_{0.98}Mn_{0.02}I_2Br$/$CsPbI_2Br$ QDs/PTAA/Au	13.47%	N_2	**116**
	ITO/SnO_2/ZnO/$CsPbI_2Br$/Spiro-OMeTAD/MoO_3/Ag	14.6%	N_2	**117**
	ITO/c-TiO_2/$CsPbBrI_2$/Spiro-OMeTAD/Ag	10.34%	N_2	**118**
	FTO/TiO_2/$CsPbI_2Br$(3D–2D–0D)/PTAA/Au	12.39%	Ambient	**119**
	FTO/NiO_x/$CsPbI_2Br$/ZnO@C_{60}/Ag	13.3%	Ambient	**120**
	ITO/c-TiO_2/$CsPbI_2Br$/Spiro-OMeTAD/Au	9.08%	N_2	**121**
	ITO/c-TiO_2/$CsPbI_2Br$/P3HT/Au	12.02%	Ambient	**122**
	FTO/TiO_2/$CsPbI_2Br$/$CsPbI_3$ QDs/PTAA/Au	14.45%	Ambient	**123**
	ITO/c-TiO_2/$CsPbI_2Br$/Spiro-OMeTAD/Au	16.07%	Glovebox	**124**
	FTO/c-TiO_2/m-TiO_2/BaI_2:$CsPbI_2Br$/P3HT/Au	14.85%	Ambient	**125**
	FTO/c-TiO_2/$CsPb_{0.9}Zn_{0.1}I_2Br$/Spiro-OMeTAD/Ag	13.6%	N_2	**126**
	ITO/SnO_2/$CsPbI_2Br$/CsBr/Spiro-OMeTAD/Au	16.37%	N_2 glovebox	**127**
$CsPbI_3$	FTO/c-TiO_2/$CsPbI_3$ QDs/Spiro-OMeTAD/MoO_x/Al	10.77%	Dry ambient condition	**128**
	FTO/c-TiO_2/$CsPbI_3$/CuI/Au	13.21%	N_2	**129**
	FTO/c-TiO_2/$CsPbI_3$/P3HT/Au	10.5%	N_2	**130**
	FTO/bl-TiO_2/mp-TiO_2/$CsPbI_3$/P_3HT/MoO_3/Au	4.68%	N_2	**131**
	FTO/c-TiO_2/$CsPbI_3$/0.025$EDAPbI_4$/Spiro-OMeTAD/Ag	11.8%	N_2	**132**
	FTO/TiO_2/α-$CsPbI_3$/Spiro-OMeTAD/Ag	4.13%	Ambient	**133**
	ITO/PTAA/$CsPbI_3$/PCBM/C_{60}/BCP/Al	11.4%	Glovebox	**134**
	FTO/bl-TiO_2/m-TiO_2/$Cs_{0.9}PEA_{0.1}PbI_3$/Spiro-OMeTAD/Au	5.7%	Ambient	**135**
	ITO/SnO_2/quasi-2D $CsPbI_3$/Spiro-OMeTAD/Au	12.4%	Ambient	**111**
	FTO/c-TiO_2/$BA_2CsPb_2I_7$/Spiro-OMeTAD/Au	4.84%	Ambient	**136**
	FTO/c-TiO_2/$CsPbI_3$/Spiro-OMeTAD/Ag	13.5%	Ambient	**137**
	FTO/c-TiO_2/$CsPbI_3$/Spiro-OMeTAD/Au	2.9%	Vacuum	**85**
	FTO/c-TiO_2/m-TiO_2/$CsPbI_3$-PVP/Spiro-OMeTAD/Au	10.74%	Glovebox	**138**
	ITO/SnO_2/$CsPbI_3$/Spiro-OMeTAD/Au	15.7%	Glovebox	**139**
	FTO/c-TiO_2/PTABr-$CsPbI_3$/Spiro-OMeTAD/Ag	17.01%	Glovebox	**140**

Table 1 (*Contd.*)

Formula	Device structures	PCE	Operation conditions	Ref.
	Glass/FTO/c-TiO_2/α-$CsPbI_3$ QDs/Spiro-OMeTAD/Au	11.87%	—	**141**
	Glass/FTO/TiO_2/$CsPbI_3$ QDs/PTAA/MoO_x/Ag	14.10%	N_2 glovebox	**142**
	FTO/c-TiO_2/m-TiO_2/γ-$CsPb_{1-x}Ca_xI_3$/Spiro-OMeTAD/Au	9.20%	—	**143**
	FTO/c-TiO_2/β-$CsPbI_3$/Spiro-OMeTAD/Ag	18.4%	N_2 glovebox	**144**

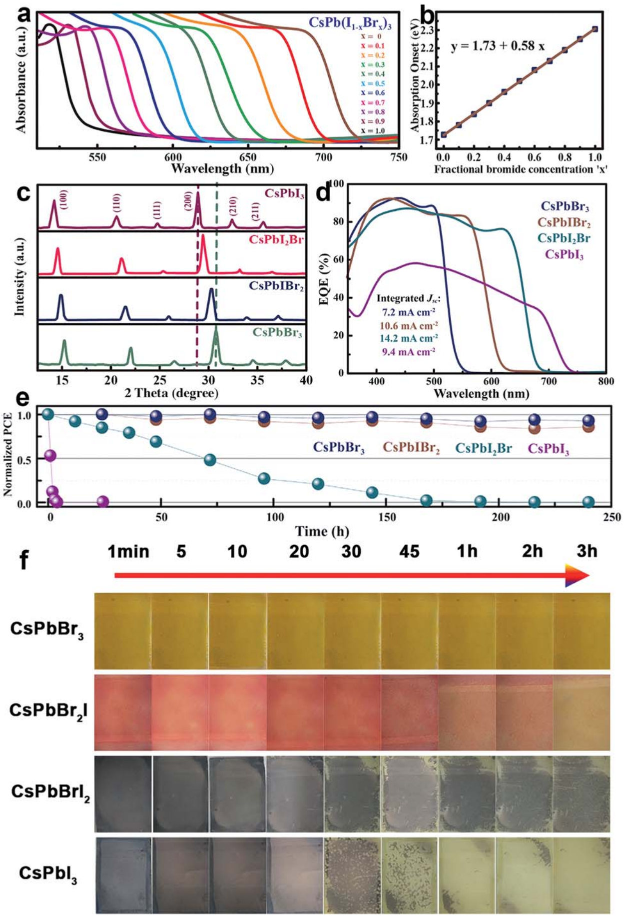

Fig. 4 (a) Absorbance spectra for inorganic $CsPbI_{3-x}Br_x$ perovskite films. (b) Plots of the optical bandgap of $CsPbI_{3-x}Br_x$ as a function of bromide composition. (c) XRD patterns of the $CsPbI_3$, $CsPbI_2Br$, $CsPbIBr_2$, and $CsPbBr_3$ films. (e) The EQE spectra of the corresponding PSC devices.[111] (f) Images of $CsPbI_{3-x}Br_x$ perovskite films in ambient atmosphere (25 °C, 40% RH).

mesoporous device with the architecture of FTO/c-TiO_2/m-TiO_2/$CsPbBr_3$/HTM/Au for the first time, obtaining a PCE of 5.95% with a V_{oc} of 1.28 V, which were comparable to the organic cation MA-containing device.[84] Subsequently, Jin and co-workers fabricated an all-inorganic $CsPbBr_3$ PSC with a similar device structure of FTO/c-TiO_2/m-TiO_2/$CsPbBr_3$/carbon (Fig. 5b and c) in an ambient environment without humidity control, demonstrating excellent moisture- and thermal tolerance even in 95% RH and 100 °C respectively, as shown in Fig. 5d and e.[88] Furthermore, to estimate the application of a $CsPbBr_3$-based device under real operating conditions, the stability was characterized under a temperature cycle between −22 °C and 100 °C without encapsulation (see Fig. 5f), where it demonstrated a superior stable crystal lattice compared to other hybrid species. According to previous reports,[153,154] the dissociation energy of $CsPbBr_3$ into CsBr and $PbBr_2$ is around 0.25 eV, which is much higher than the hybrid $MAPbBr_3$ of 0.19 eV, which is undoubtedly an origination of their excellent stability.

To date, the overall solar-to-electric conversion efficiency of this proof-of-concept photovoltaic is still lower compared to I-containing devices, mainly arising from the substantial defects and broad tail absorption. A key parameter for a high-efficiency $CsPbBr_3$ PSC is a minimal defect state in order to trap photo-induced carriers. Within the $CsPbBr_3$ film, most of the intrinsic defects induce a shallow transition level, while a few defects with high formation energy will lead to deep transition levels, demonstrating that the $CsPbBr_3$ is a defect-tolerance semiconductor and has superior optoelectric properties.[154] The corresponding charge-transition levels induced by

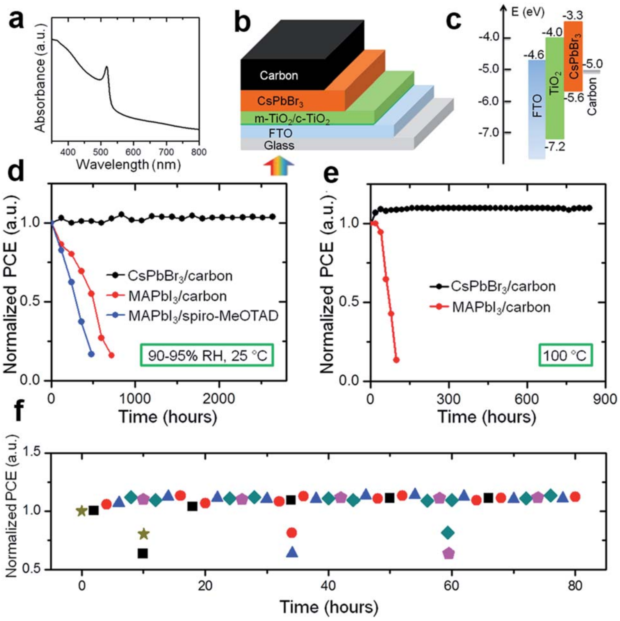

Fig. 5 (a) Absorbance spectra for inorganic $CsPbBr_3$ perovskite films. (b) Schematic structure and (c) energy level diagram of inorganic $CsPbBr_3$ PSCs. The long-term stability of inorganic $CsPbBr_3$ PSCs under: (d) 90–95% RH, 25 °C, (e) 100 °C, and (f) temperature cycles between −22 °C and 100 °C without encapsulation.[88]

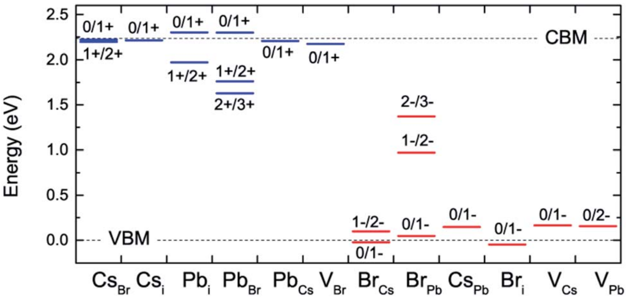

Fig. 6 Defect charge-transition levels from first-principles calculations.[154]

various defects are summarized in Fig. 6 according to theoretical calculations, and only Pb_i, Pb_{Br}, and Br_{Pb} defects produce unwanted deep transition levels (trapping the carrier by way of non-irradiative recombination). Therefore, controlling the growth conditions (under moderate or Br-poor conditions) is crucial to obtain high-quality perovskite films. Aiming to resolve this issue, Tang's group conducted enormous efforts on $CsPbBr_3$-based solar cells, including improving the perovskite film quality, interfacial engineering, and spectral engineering as well as compositional engineering (will be discussed in Sections 4 and 6), boosting the efficiency to 10.6% from an initial 6.7%.[89,92,97,99,100] These works open a new era for developing all-inorganic $CsPbBr_3$ PSCs for cost-effective and stable thin-film photovoltaics. The low cost, simplified device configuration, solution-processable technique, and excellent durability in harsh conditions make all-inorganic $CsPbBr_3$ PSCs promising candidates for large-scale production.

During the study in $CsPbBr_3$ crystals, several all-bromide perovskite derivative phases, such as $PbBr_2$-riched $CsPb_2Br_5$ and CsBr-riched Cs_4PbBr_6, have been discovered in the interior of $CsPbBr_3$ film.[89,155,156] The dimensionality of the Cs–Pb–Br structure can be evolved along with a gradual change of the stoichiometry, from 3D to 0D. Previous reports found that the presence of such a non-perovskite phase can passivate the interfaces and grain boundaries, whereas excess amounts will degrade the overall photovoltaic performance owing to the introduction of defects.[96,157] Recently, Tong *et al.* developed a graded heterojunction device by introducing the perovskite derivative phase into all-inorganic PSCs. Arising from the boosted hole-extraction ability and reduced recombination, a device with the architecture of FTO/c-TiO_2/$CsPbBr_3$/$CsPbBr_3$–$CsPb_2Br_5$/$CsPbBr_3$–Cs_4PbBr_6/carbon achieved an enhanced PCE of up to 10.17%, opening the window for a perovskite derivative phase.[101] Furthermore, by optimizing the crystal growth procedure induced by phase transition, the grain size of $CsPbBr_3$ perovskite films and the surface potential barrier existing between the crystals and grain boundaries have been successfully tuned, leading to a recorded PCE of up to 10.91% for an n–i–p structured PSC.[103] Similarly, binary $CsPbBr_3$–$CsPb_2Br_5$ perovskites-based solar cells also show much higher power output capacity, which is mainly attributed to the decreased intrinsic Br vacancies on $CsPbBr_3$. Actually, the $CsPb_2Br_5$ in $CsPbBr_3$ film cannot be totally eliminated even with careful control of the precursor ratio owing to its transformation from $CsPbBr_3$ to $CsPb_2Br_5$ under elevated temperature.[155] Following this line of thought, precisely tuning the film quality of the perovskite layer is crucial for high-efficiency platforms.

According to the above-mentioned discussion, it can be seen that $CsPbBr_3$ PSCs stand out for their excellent long-term stability, while the great challenge for them is overcoming their relatively lower efficiency in spite of their efficiency being around 11%. How to take the advantage of their stability and improve their efficiency is an urgent need. Integrating this kind of device with wider light absorbance materials, such as Si, PbS, and ZnS:SnS heterojunction, may be a promising path for the further development of $CsPbBr_3$-based PSCs.

3.1.2 $CsPbIBr_2$. Mixed halide $CsPbIBr_2$ perovskites have a narrower bandgap of 2.05 eV, which allows them to be potentially applied in a three-junction tandem cell. Compared to other inorganic perovskites, the research on $CsPbIBr_2$-based devices has stagnated. Ho-Baillie and co-workers pioneered and fabricated an HTM-free planar glass/FTO/c-TiO_2/$CsPbIBr_2$/Au solar cell using a dual source thermal evaporation method, achieving an initial PCE of 4.7% (J_{sc} = 8.7 mA cm^{-2}, V_{oc} = 959 mV, FF = 56%) under reverse scan as well as a PCE of 3.7% (J_{sc} = 8.7 mA cm^{-2}, V_{oc} = 818 mV, FF = 52%) under forward scan for the first time.[104] Subsequently, a spray-assisted solution-processed technology was further employed to fabricate a $CsPbIBr_2$ film, overcoming the solubility problem of Br ions in the precursor.[105] To improve the efficiency of $CsPbIBr_2$ PSCs, researchers began to create new strategies for dense and pinhole-free $CsPbIBr_2$ films with a high crystalline quality.[109,158–160] To date, a champion PCE as high as 11.53% in the field of $CsPbIBr_2$-based PSCs was obtained by partially substituting Pb^{2+} with Sn^{2+} cations, which is similar to the PCE of hybrid perovskite films.[109] The further red-shift and higher absorbance of $CsPb_{0.9}Sn_{0.1}IBr_2$ than both $CsPbBr_3$ and $CsPbIBr_2$ indicated the substitution of I^- and Sn^{2+} ions reduces the bandgap of inorganic perovskites, as shown in Fig. 7.[70] The bandgap of $CsPb_{0.9}Sn_{0.1}IBr_2$ was determined to be 1.79 eV, close to the 1.73 eV for $CsPbI_3$.[128,130,133,161,162] An optimal PSC with a device structure of FTO/c-TiO_2/m-TiO_2/$CsPb_{0.9}Sn_{0.1}IBr_2$/carbon presented more favorable energy band levels, as shown in Fig. 7d, achieving a higher integrated J_{sc} of 10.15 mA cm^{-2}. Through incorporating Sn^{2+} ions into host $CsPbIBr_2$, all the photovoltaic parameters of $CsPb_{0.9}Sn_{0.1}IBr_2$-tailored PSCs including V_{oc}, J_{sc}, and FF displayed significant increases. Intriguingly, the V_{oc} of 1.26 V for the $CsPb_{0.9}Sn_{0.1}IBr_2$-based all-inorganic PSC was higher than the 1.08 V of $CsPbIBr_2$ or 1.25 V of $CsPbBr_3$ devices due to the deep VBM of the $CsPb_{0.9}Sn_{0.1}IBr_2$ (0.13 eV) being closer to the CBM of the electron acceptor. Similarly, Wang *et al.* systematically investigated the morphologies and optoelectronic properties evolution of $CsPb_{1-x}Sn_xIBr_2$ films along with changing the Sn^{2+} dosage from $x = 0$ to $x = 1$, realizing tunable bandgaps from 2.04 eV to 1.64 eV.[109] Finally, a remarkable PCE of 11.53% with a high V_{oc} of 1.21 V was achieved. The advantages of high thermal stability, superb energy band position, and tunable bandgap demonstrated that mixed Pb/Sn- and I/Br-tailored $CsPb_{0.9}Sn_{0.1}IBr_2$ perovskites

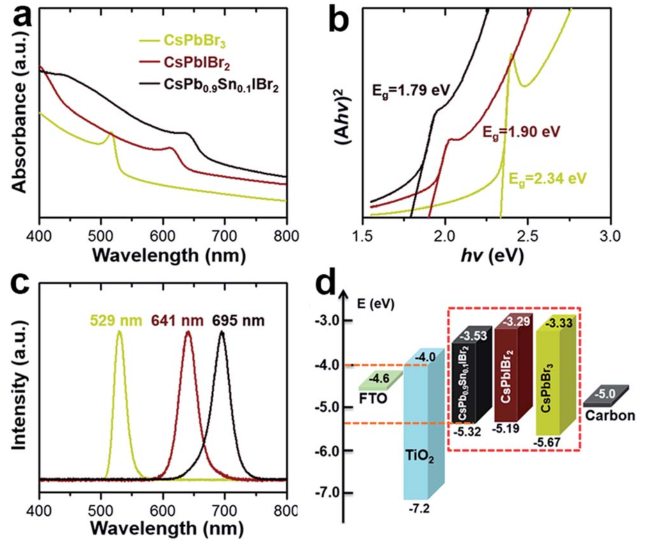

Fig. 7 (a) Absorption spectra and (b) corresponding $(Ahv)^2$ *vs.* energy (hv) curves of perovskite films by partially substituting Pb^{2+} with Sn^{2+}. (c) PL spectra of $CsPbBr_3$, $CsPbIBr_2$, and $CsPb_{0.9}Sn_{0.1}IBr_2$ films. (d) Energy level diagram of the all-inorganic PSCs.[70]

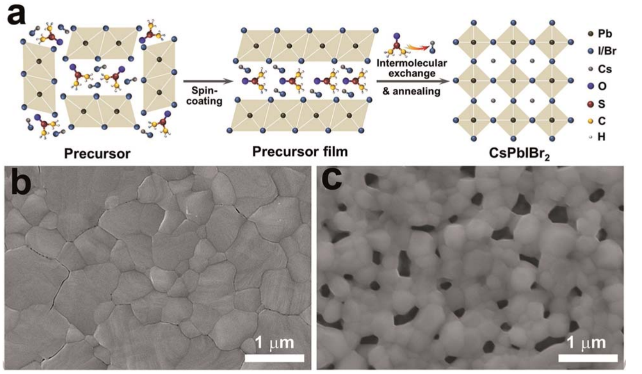

Fig. 8 (a) Schematic of the intermolecular exchange strategy. SEM images of $CsPbIBr_2$ films obtained by: (b) intermolecular exchange and (c) conventional route.[165]

were promising candidates for advanced photovoltaics and optoelectronic applications.

As for photovoltaic cells, the larger energy loss ($E_{loss} = E_g - eV_{oc}$, in which E_g, e, and V_{oc} represent the bandgap, elementary charge, and open-circuit voltage, respectively) in inorganic PSCs is conspicuous compared to hybrid devices, which is mainly attributed to the non-radiative recombination related to the defect states.[122,163] Cheng *et al.* discovered that "iodide-rich" $CsPbI_{(1+x)}Br_{(2-x)}$ phases will be formed at grain boundaries as well as will segregate as clusters inside the $CsPbIBr_2$ film under light and electron beam illumination as ion migration "highways", resulting in an enhanced PCE as well as serious hysteresis and sluggish performance/stability.[164] In particular, the two-step solution-processed film generally involve I-rich species, which can accelerate the phase segregation. To effectively address these issues, an intermolecular exchange route to fabricate the desired $CsPbIBr_2$ film was proposed by Zhu *et al.* involving spin-coating CsI onto the surface of $CsPbIBr_2$ precursor films, as shown in Fig. 8.[165] As a result, the HTM-free, carbon-based $CsPbIBr_2$-based PSC achieved an enhanced efficiency of up to 9.16%, with a stabilized PCE of 8.46%, which was mainly attributed to the optimized crystallinity and reduced defects. Furthermore, they also made great efforts to enhance the performance of this kind of photovoltaic device by optimizing the ETL/perovskite or/and HTL/perovskite interfaces.[108,166,167] For example, upon successfully incorporating CsBr clusters into the $TiO_2/CsPbIBr_2$ heterojunction, a beneficial upper level of the conduction band of TiO_2 from −4.00 to −3.81 eV and the lowering of the work function from 4.11 to 3.86 eV were realized. As a result, the $CsPbIBr_2$ solar cell exhibited a PCE of 10.71% with an efficiency enhancement of 20%, mainly attributed to the optimized band alignment and suppressed charge recombination.[108]

However, the hysteresis in a device still occurs in spite of the greatly reduced defect states by means of doping or tuning crystallization kinetics. To further improve the efficiency of $CsPbIBr_2$ PSCs, significantly reducing the grain boundaries and increasing the grain size are crucial for efficient carrier extraction and transfer, especially for reducing the energy loss (increased V_{oc}).

3.1.3 $CsPbI_2Br$.

To advance the application of inorganic PSCs, developing tandem solar cells is a promising way to increase the efficiency of existing solar cell technologies at a relatively low cost.[168–170] Viable top cell materials for use with a Si bottom cell should have an optical bandgap of ~1.8 eV, which should be resistant to photo-induced phase segregation and stable under 150 °C, a typical curing temperature for ethylene-vinyl acetate (EVA) and many other commercial encapsulants. The bandgap of $CsPbBrI_2$ thin films are reported to be ~1.9 eV (630 nm), while their lattices are significantly more structurally stable in the cubic phase than their fully iodide counterparts, demonstrating their potential application in multi-junction solar cells. Snaith's group systematically compared the absorption and XRD spectra of $CsPbI_2Br$ and $MAPbI_2Br$ films in 2016, as shown in Fig. 9a–d.[161] Obviously, $CsPbI_2Br$ showed both phase and compositional stability when heated at 85 °C in 20–25% RH, while $MAPbI_2Br$ showed compositional instability under the same conditions.

Although $CsPbI_2Br$ was demonstrated as escaping from thermal degradation at high temperatures within the processing and operational window, the light-induced instability is a crucial issue for $CsPbI_2Br$-based photovoltaics. Halide dealloying in $CsPbBrI_2$ perovskite solar cells was clearly proven under solar light irradiation, and this process is reversible.[171] As shown in Fig. 9e, the PL peaks of $CsPb(I_{1-x}Br_x)_3$ presented slight fluctuations under one sunlight persistent irradiation when $x < 0.4$, and adverse fluctuations upon $0.4 < x < 1$, attributed to the formation of iodine-rich and bromine-rich phases, respectively. What the impact of halide dealloying on solar cell performance was first demonstrated by Choi *et al.*, who attempted to increase the efficiency of the corresponding device inspired by "light-induced self-poling" in a $MAPbI_3$-based device.[118] In their

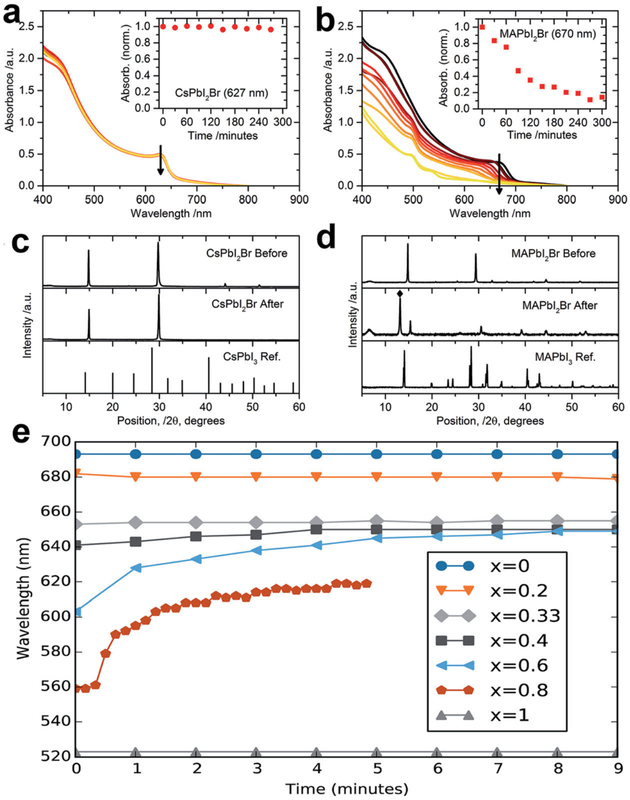

Fig. 9 Absorbance spectra of (a) $CsPbI_2Br$ and (b) $MAPbI_2Br$ films by heating at 85 °C in 20–25% RH for different times. Arrows indicate the direction of increasing heating time. Insets represent absorption intensity over time at the peak of onset (627 and 670 nm; arrow positions in the main plot). XRD profiles before and after 270 min of heating at 85 °C in 20–25% RH for (c) $CsPbI_2Br$ and (d) $MAPbI_2Br$.[161] (e) PL peak position as a function of time for $CsPb(I_{1-x}Br_x)_3$ materials under one sun illumination.[171]

findings, the hole-collection ability could be significantly enhanced owing to the phase segregation and formation of I-rich regions, leading to average and champion device PCEs as high as 9.22 ± 0.64% and 10.34%, respectively.

In fact, the light-induced effects in perovskites, such as phase segregation, ion migration, and defect formation, are responsible for the light degradation of hybrid perovskite solar cells. Following this line of thought, whether the above-mentioned light-induced instability of the all-inorganic $CsPbI_2Br$ film will reduce the device long-term stability is important to consider under solar irradiation. Later, Zhao *et al.* especially studied the light-enhanced ion migration effect in inorganic $CsPbI_2Br$ and hybrid $MAPbI_3$, revealing the light-independent ionic transport mechanism on the stability improvement by inorganic cation substitution in a perovskite-based optoelectronic device.[112] By monitoring the $CsPbI_2Br$ film during the poling process in ambient air at 25 °C, they did not find a dendritic structure in $CsPbI_2Br$ film under illumination (5 and 25 mW cm^{-2}) for 20 s, indicating the $CsPbI_2Br$ perovskite film was much more stable under illumination compared to MA^+-based perovskite film. To better understand the ionic-transport behaviors in inorganic and hybrid perovskites, the energy barrier of ion migration (E_a^{off}) can be derived from eqn (1):[172]

$$\sigma_{\text{ion}}(T)T = ne\mu = \frac{Z_i e^2 N_A C_{v0} D_0}{k_B V_m}\exp\left(\frac{G_v}{5k_B T}\right)\exp\left(\frac{E_a}{k_B T}\right) = \sigma_0\exp\left(\frac{E_a^{\text{off}}}{k_B T}\right) \tag{1}$$

where Z_i is the ionic charge, N_A is Avogadro's constant, C_{v0} is the intrinsic defects concentration, D_0 is the diffusion coefficient, V_m is the molar volume of perovskite, G_v is the vacancy defects formation energy, and K_B is Boltzmann's constant. Gottesman and co-workers demonstrated the light-enhanced ionic migration in $MAPbI_3$ films could be mainly attributed to the weaker binding between MA^+ and inorganic species upon exposure to solar light irradiation.[173] Meanwhile, the activation energy for ion migration of $MAPbI_3$ film could be reduced to 0.07 eV from 0.62 eV when tuning the light intensity from 25 to 0.1 mW cm^{-2}. On the contrary, the activation energy was nearly unchanged around 0.45 eV for $CsPbI_2Br$, an indicator of its excellent stability in spite of the presence of phase segregation. A similar conclusion was also reached for the all-bromine perovskite system.[174]

According to the above-mentioned discussion, the light-induced halide segregation is still unclear regarding whether it is beneficial for improving the PCE of the corresponding devices. The effects of phase segregation enhanced ionic movement and accelerated hole extraction along with increased injection barriers or hysteresis are fuzzy in studies pf all-inorganic perovskites, with no consensus. Therefore, further exploration focusing on this point should be conducted in the future.

As the most popular research topic in inorganic PSCs other than $CsPbI_3$ (thermodynamic instability) and Br-rich $CsPbIBr_2$ or $CsPbBr_3$ (larger optical bandgaps), another crucial issue on the way toward commercialization is the high-temperature annealing process to obtain an ideal black phase, which is undesirable for flexible devices. The phase conversion temperature is highly dependent on the fabrication technology. A recent investigation on the crystal behavior of phase-pure $CsPbI_2Br$ *via* a one-step method indicated that the effective phase conversion can only be realized when the annealing temperature is over 260 °C.[175] Sutton and co-workers demonstrated that a much higher crystallization temperature was required when employing a two-step method to fabricate an all-inorganic perovskite film. Furthermore, gas-vapor assisted technologies elevated the temperature to >300 °C.[161] To significantly reduce the energy-consumption, incorporating I-excess precursors of $HPbI_{3+x}$ (x = 0.1–0.2) to replace PbI_2 and substituting traditional DMF with dimethylsulphoxide (DMSO, a stronger coordination solvent) were tested, resulting in the successful phase conversion even at room temperature.[176] The possible mechanism behind these phenomena is mainly attributed to the formation of an intermediate phase, accelerating the room temperature conversion of the cubic $CsPbI_2Br$, which has also been observed in the $CsPbI_3$ system.[85] Owing to the much higher coordination interaction between DMSO and

PbI_2 than that of DMF, a longer PbI_2 interplanar distance could be formed, which is beneficial for the subsequent intercalation of CsI species. Subsequently, a CsI–Pb[I/Br]$_2$–DMSO intermediate phase was spontaneously formed. Upon the solvent escaping from this intermediate concept, a perovskite phase could be obtained.[177]

The $CsPbI_2Br$ film quality, defect-free crystallinity, and thickness dominate the photovoltaic performance of the corresponding device. To date, by the precise growth controlling and post-treatment of $CsPbI_2Br$ film has demonstrated considerable advantages for efficiency enhancement, yielding an enhanced efficiency of over 16%.[124] Utilizing the post-treatment of evaporating CsBr to passivate the $CsPbI_2Br$/HTL interface and reduce the energy loss, a recorded efficiency of up to 16.37% was obtained.[127] Compared to hybrid perovskites, inorganic $CsPbI_2Br$ with superior long-term stability and a high light absorbance ability shows great potential for application in photovoltaics, especially tandem solar cells, by allowing developing a novel fabrication technology and stabilizing the lattice to facilitate a simple assembly process and eliminating phase segregation.

3.1.4 $CsPbI_3$. When completely removing the Br atom in cesium lead halides, a triiodide $CsPbI_3$ with a bandgap of 1.73 eV was formed, which is much more appropriate as a photovoltaic candidate among all the all-inorganic perovskites. However, in early research, the $CsPbI_3$-based PSCs presented sluggish efficiency because the black cubic perovskite phase is thermodynamically preferred only above 330 °C and converts into a photoinactive orthorhombic δ-phase (yellow phase) at lower temperature.[85,178] The mechanism behind this phenomenon is that the tolerance factor of $CsPbI_3$ was calculated as 0.80 according to the ionic radii of Cs^+, Pb^{2+}, and I^-, which is relatively lower and easier to maintain the 'black' polymorph structure and to easily transfer to its 'yellow' non-perovskite polymorph, which is thermodynamically more stable at ambient temperature. This is the biggest challenge in the pursuit of high-performance platforms. Actually, based on the recent study by Zhao's group, most of the previously reported results on the $CsPbI_3$ phase with a 1.73 eV bandgap correspond to γ-$CsPbI_3$ not to the α-$CsPbI_3$ phase. In 2013, $CsPbI_3$ was experimentally formed by substituting the organic MA^+ cation in $MAPbI_3$ with Cs^+ ion, and this was then used as a light absorber for a solar cell application for the first time.[60] By careful processing control (with the addition of HI into the precursor, which is similar to the above-mentioned conclusion in Section 3.1.3) and the development of a low-temperature phase transition route, Snaith *et al.* stabilized the $CsPbI_3$ halide in its black perovskite phase and finally obtained an efficiency of up to 2.9% for a planar heterojunction architecture.[85] Thereafter, ever-increased strategies have been launched to improve the environmental stability of perovskite-structured $CsPbI_3$, such as controlling the grain size,[128] composition engineering (*e.g.*, PEA^+,[111,135] sulfobetaine zwitterion,[134] PVP,[138] bication 2D-quasi perovskite,[132] and external cations/anions doping[90]) and solvent control.

Grain refinement has been demonstrated to be a promising strategy to stabilize the crystal lattice owing to the higher contribution of surface energy. In 2016, Luther and co-workers synthesized α-$CsPbI_3$ QD films (Fig. 10a and b), which were stable for months in ambient air.[128] When assembling into a photovoltaic device with the architecture of FTO/TiO_2/QDs/Spiro-OMeTAD/MoO_x/Al, a recorded efficiency of 10.77% with an open-circuit voltage of 1.23 V was achieved (Fig. 10c), providing a path to assemble high-performance devices. However, the short-circuit current density and fill factor were limited by charge transportation to a certain extent.[128,152] Therefore, they further developed a novel avenue *via* AX (A = FA^+, MA^+, Cs^+; X = I^-, Br^-) treatment to improve the charge transportation of α-$CsPbI_3$ QD-based perovskite solar cells, leading to a record certified QD solar cell efficiency of 13.43% (Fig. 10d).[179] In detail, the $CsPbI_3$ QD film for this work was deposited by layer-by-layer spin-coating; next, each QD layer was immersed into a saturated lead(II) nitrate [$Pb(NO_3)_2$] solution in methyl acetate (MeOAc) to partially remove the native ligands and to allow for further layers to be deposited without re-dispersing the existing layers; after forming a sufficiently thick $CsPbI_3$ QD film (200–400 nm), the film was immersed into a saturated AX salt solution in ethyl acetate (EtOAc) for around 10 s, as illustrated in Fig. 10e. Recently, an efficient surface passivation method for $CsPbI_3$ perovskite QDs using a variety of inorganic cesium salts has been also reported by Ma *et al.*, as shown in Fig. 10g, with not only filling the vacancy at the $CsPbI_3$ perovskite surface but also improving the electron coupling between QDs. As a result, an impressive efficiency of 14.10% for $CsPbI_3$ QD solar cells was obtained.[142] This method has also been applied to fabricate $CsPbBr_3$ QDs based films, which has been discussed as following. Likewise, Huang and coworkers added sulfobetaine zwitterions into a $CsPbI_3$ precursor solution (Fig. 10f) to impede $CsPbI_3$ crystallization *via* electrostatic interaction with the ions and colloids in the $CsPbI_3$ precursor solution to form small-grained films with an average size of 30 nm, thus resulting in enhanced α-phase stability.[134] As shown in Fig. 10h, during spin-coating of the precursor solution, the process of Cs^+ ions entering the octahedral sites of $[PbI_6]^{4-}$ octahedra to form a $CsPbI_3$ perovskite is quick, leading to larger grains with the orthorhombic phase. Upon introducing sulfobetaine zwitterions into the system, the above process will be suppressed owing to the collapse of the layered structure of the colloids; therefore, leading to a decreased colloid size. Furthermore, the molecules will be expelled to the grain boundaries and will impede the grain growth continuously. Finally, the device could maintain 85% of its initial efficiency after storage in air for over 30 days, demonstrating the great potential to stabilize the crystal by reducing the grain size. However, for all the methods mentioned here, the inferior interfacial charger-transfer behavior is still a major issue to solve to further improve the efficiency of solar cells. Zhang *et al.* employed oleic acid, oleylamine, octanoic acid, and octylamine as capping ligands for synthesizing high-quality $CsPbI_3$ QDs (Fig. 10i).[141] Although an enhanced efficiency from 7.76% to 11.87% was obtained owing to the reduced charge-transfer resistance induced by the shorter ligands, substantial recombination was still present. With the aim to resolve this problem, Liu's group used high-mobility μGR sheets to react with the

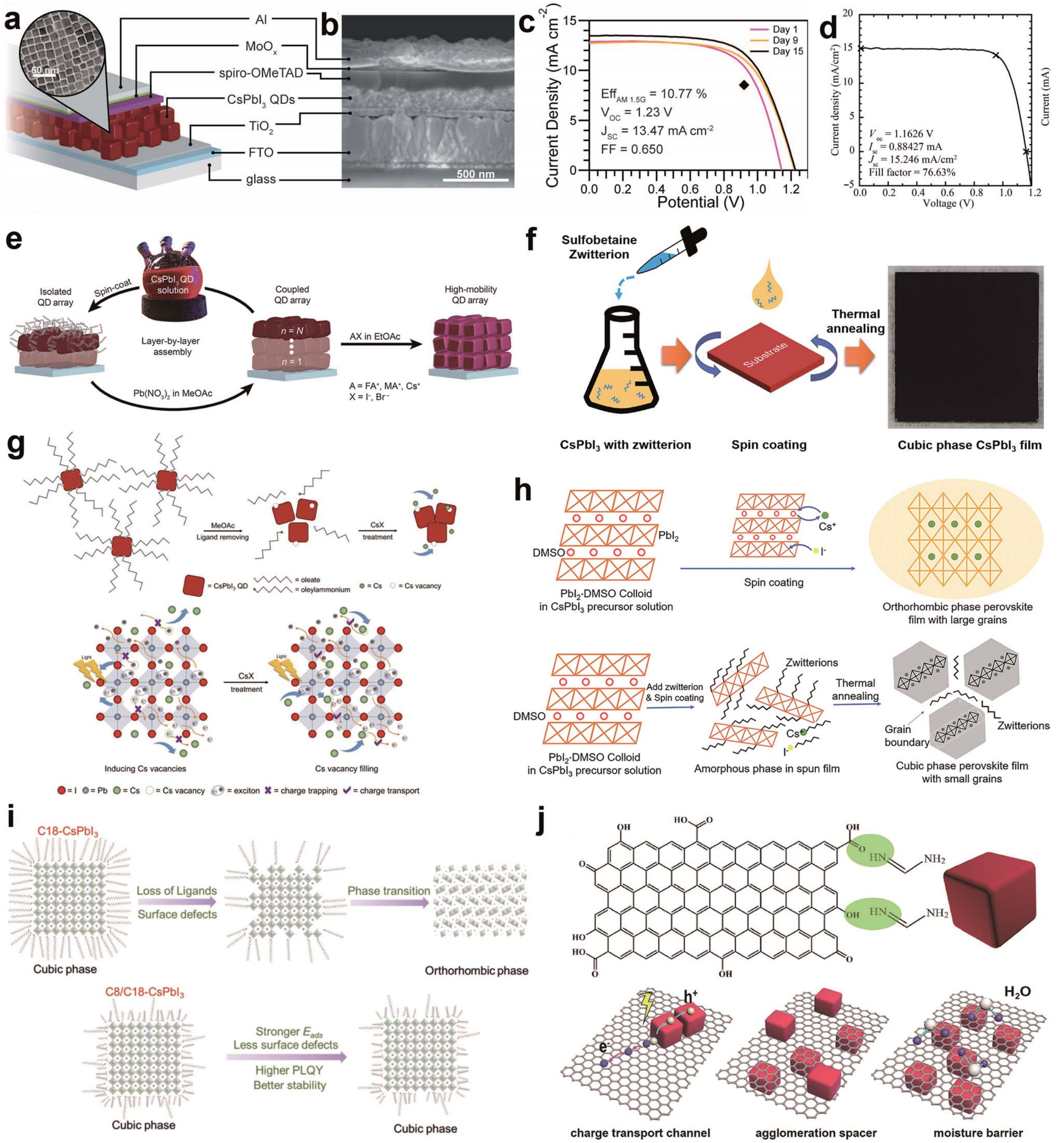

Fig. 10 (a) Schematic and (b) cross-sectional SEM image of a CsPbI$_3$-tailored solar cell.[128] Current density–voltage curves of the corresponding devices with (c) and without (d) surface treatment.[128,179] Schematic of the perovskite film deposition processes of (e) AX salt post-treated QDs[179] and (f) zwitterions-assisted technology.[134] (g) Schematic illustrations of CsPbI$_3$ QD film deposition and CsX post-treatment process.[142] (h) Mechanism of α-phase CsPbI$_3$ stabilization by zwitterions.[134] (i) Schematic of CsPbI$_3$ α-phase stabilization mechanism due to the presence of shorter ligands.[141] (j) Chemical structure of the μGR and CsPbI$_3$ QDs, and their cross-linking mechanism. Schematic illustration of the charge-transport process and stabilization mechanism for the μGR/CsPbI$_3$ film-based PSCs.[180]

CsPbI$_3$ QDs to accelerate charge transfer and extraction, as depicted in Fig. 10j. They proved that intermolecular hydrogen bonds cross-linked two materials together through Fourier transform infrared spectroscopy (FT-IR) determination,[180] inhibiting the self-healing induced accumulation and aggregation of QDs. Therefore, the phase transition induced degradation from the α-phase to the δ-phase was suppressed, which in turn increased the environmental tolerance. Meanwhile, μGR can also protect QDs from being attacked by water molecules due to its hydrophobic group.[181–183] Arising from the stabilized lattice and effective charge-transport dynamics, an enhanced PCE of up to 13.59% has been obtained.

Another strategy to significantly enhance the stability of the $CsPbI_3$ crystal lattice is to increase the moisture resistance and decrease the dimension structure of perovskite materials by introducing a long-chain polymer and large cations. Li and coworkers incorporated polymer polyvinylpyrrolidone (PVP) into the perovskite precursor solution to stabilize inorganic perovskite $CsPbI_3$ with a cubic crystal structure *via* a reproducible solution-chemistry reaction process.[138] Owing to the interaction between the acylamino group in PVP and $CsPbI_3$, as shown in Fig. 11a, the grain boundaries could be effectively passivated, resulting in an enhanced efficiency of 10.74% with excellent thermal and moisture stability. The corresponding conclusions have been also explored in hybrid perovskite devices similar to PEG polymer incorporation. Unlike the organic cation in organic–inorganic hybrid perovskites, the Cs^+ cation in the $CsPbI_3$ crystal lattice is highly stable and therefore a quasi-2D perovskite layer would be formed upon substituting Cs^+ with a large radius cation, such as phenylethylammonium (PEA^+),[135,137] ethylenediamine (EDA^+),[132] triple cation diethylenetriamine ($NH_3^+C_2H_4NH_2^+C_2H_4NH_3^+$),[184] and phenyltrimethylammonium (PTA^+).[140] Especially, Liu and Zhao *et al.* introduced PEA^+ to form a defect-passivating organic cation terminated surface to improve the phase stability and moisture resistance.[137,185] The mechanism is depicted in Fig. 11b and c. Through forming the intermediate hydrogen lead iodide ($HPbI_{3+x}$) before the distorted black phase as an avenue to lower the crystallization temperature and stabilize the lattice according to previous reports, a solar cell efficiency as high as 15.07% and negligible efficiency loss after 300 h light soaking without encapsulation were obtained. Almost simultaneously, Chen's group adopted cesium acetate (CsAc) and hydrogen lead trihalide ($HPbX_3$) as a new precursor pair to form high-quality $CsPbX_3$ films by introducing a trace of PEAI into the new precursor system, which could reduce the dimension of the perovskite and thereby significantly suppress the undesirable phase transition.[111] Strikingly, following a one-step spinning method, they were able to fabricate mirror-like $CsPbI_3$ films with an area as high as 9 × 9 cm^2, providing a possibility for realizing large-area commercialization device fabrication. More recently, Zhao *et al.* mitigated the effects of cracks and pinholes in the perovskite layer by surface treatment with choline iodide (CHI), as shown in Fig. 11d, which increased the charge-carrier lifetime and improved the energy-level alignment between the β-$CsPbI_3$ absorber layer and carrier-selective contacts. As a result, a recorded efficiency reaching 18.4% under 45 ± 5 °C ambient conditions was obtained, demonstrating that the inorganic perovskites are promising as light absorbers.[144]

According to aforementioned discussion, two main avenues to stabilize α-phase $CsPbI_3$ can be concluded: (1) reduce the crystal size, no matter whether 2D or quantum dots; (2) surface-terminated protection, no matter by solvent control or by the introduction of organic groups. Besides, doping smaller ions to substitute the Cs^+ and realizing lattice contraction (which will be discussed in the following part) is also an effective method to stabilize the $CsPbI_3$ phase. All these various strategies to reduce the surface energy to enhance the phase stability and the long-term performance of state-of-the-art devices based on various stabilization strategies are summarized in Table 2.

3.2 Pb-free perovskites

Lead-based inorganic perovskites are the most studied materials in all-inorganic perovskite devices, which have achieved PCEs of over 10% with the highest value of 18.4%. In this review, we mainly focus on depicting the progress of Pb-based inorganic perovskite solar cells. However, with an aim to better understand the development situation of this emerging class of photovoltaics, Pb-free perovskite assembled devices are also discussed in this part.

Actually, the first all-inorganic perovskite solar cell was based on Sn-containing materials by completely substituting Pb^{2+} with Sn^{2+} in 2012, achieving an efficiency of 0.88%.[186] Unfortunately, compared with Pb-based inorganic perovskite, Sn-based inorganic perovskites are more susceptible to moisture-mediated degradation, oxygen-mediated oxidation of Sn^{2+} to Sn^{4+}, and even to beam damage, leading to severe decomposition of the original structure.[187,188] Subsequently, Kumar *et al.* fabricated a common photovoltaic device with the configuration FTO/TiO_2/$CsSnI_3$/HTM/Au, showing an improved PCE up to 2.02% by introducing SnF_2 into the lattice of $CsSnI_3$ to reduce the intrinsic defects, such as Sn-cation vacancies.[189] A corresponding conclusion was also demonstrated in $CsSnBr_3$ PSC.[187] Hodes *et al.* reported that the addition of SnF_2 could slightly raise the work function and E_{VBM} of $CsSnBr_3$ and increase stability against electron beam damage. After carefully controlling the dosage of SnF_2, the PCE could be increased to over 2% from an initial 0.01%. Further, Mai's group introduced SnF_2 and hypophosphorous acid (HPA) additive to improve the phase stability of a Sn-based perovskite during long-term thermal treatment, as shown in Fig. 12a and b.[190] Arising from the inhibition of the formation of Sn^{4+} during the formation process of $CsSnIBr_2$ films, the long-term stability could be significantly enhanced. Finally, PCEs of around 3% were obtained by $CsSnIBr_2$ with the mesoscopic PSC architecture. All the above-mentioned results demonstrate the promising application of Pb-free perovskites as photoactive layers in corresponding devices.

Similar to $CsPbX_3$, as shown in Fig. 12c and d, when increasing the Br doping dosage, the optical bandgap of $CsSnX_3$ increases from 1.27 eV for $CsSnI_3$ to 1.37, 1.65, and 1.75 eV for $CsSnI_2Br$, $CsSnIBr_2$, and $CsSnBr_3$, respectively.[191] Meanwhile, the photovoltaic performances and stability are highly dependent on the composition. An obvious improvement in V_{oc} and decrease in J_{sc} could be detected upon incorporating Br element, as shown in Fig. 12e, which was mainly attributed to the reduced Sn-cation vacancies. By adding SnF_2 to further optimize the film quality, an optimal PCE of 1.76% was obtained for $CsSnI_{2.9}Br_{0.1}$ PSCs. By adding $SnCl_2$ into the $CsSnI_3$ perovskite precursor, Hatton's group formed a low pin-hole

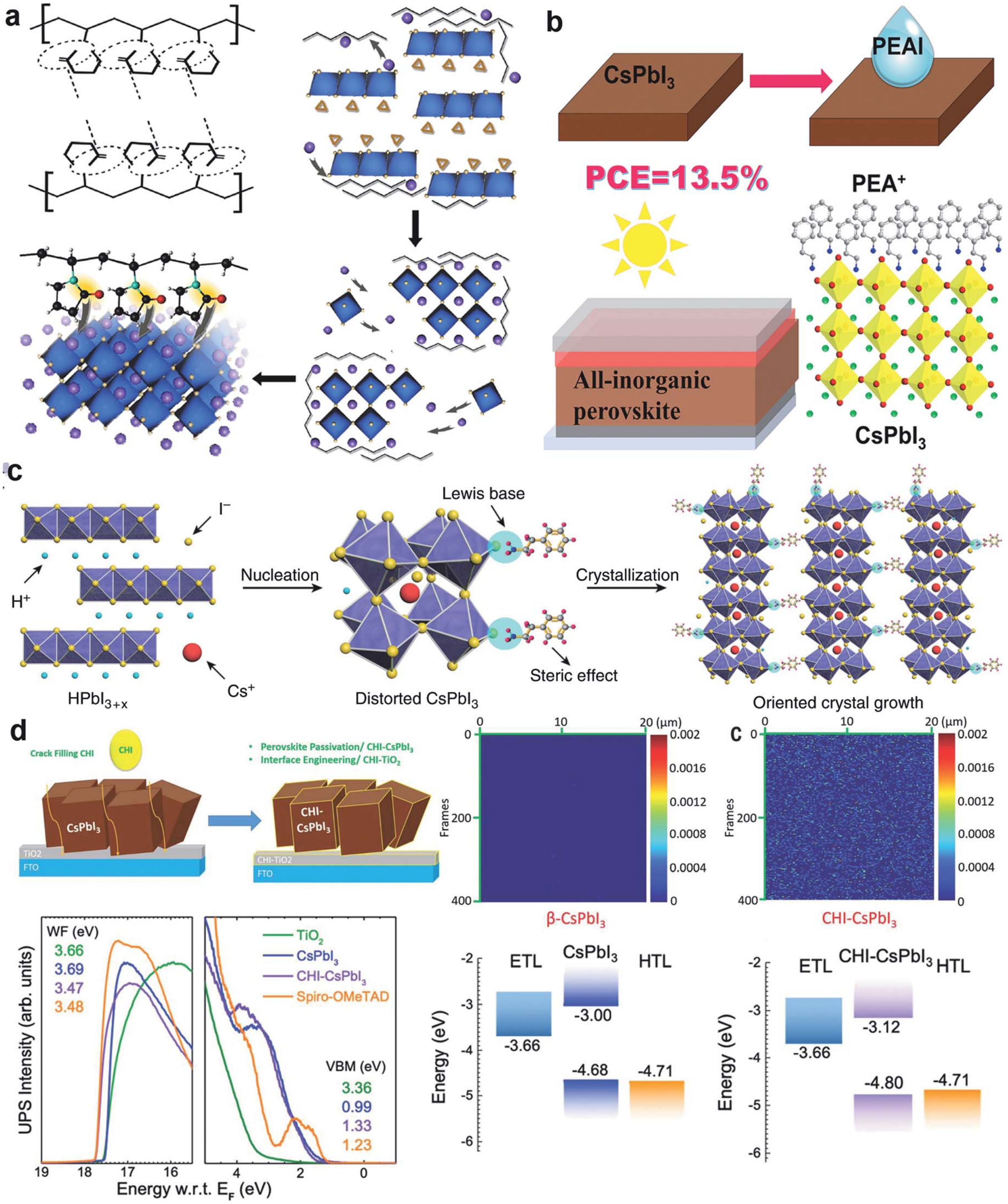

Fig. 11 Mechanism of enhanced phase stability of $CsPbI_3$ films by incorporating: (a) PVP,[138] (b) PEAI,[137] (c) HI/PEAI,[185] and (d) CHI.[144]

density and highly stable $CsSnI_3$ perovskite film, achieving a high PCE of 3.56%.[192]

Apart from the Sn-based Pb-free perovskites, employing Ge element to substitute Pb or forming perovskite derived materials, such as A_2BX_6 (2-1-6), $A_3B_2X_9$ (3-2-9), and $A_2B^{1+}B^{3+}X_6$ (2-1-1-6) are another two strategies to obtain Pb-free perovskites. The typical compounds contain $CsGeCl_3$, $CsGeBr_3$, and $CsGeI_3$, with bandgaps of 3.67, 2.32, and 1.53 eV, respectively.[193] To date, their efficiency as well as stability are still much lower compared to Pb-containing devices, mainly attributed to the easily oxidized behavior of Ge^{2+} to Ge^{4+}. Efficient stabilizing of the lattice of $CsGe(Sn)X_3$ is a great challenge to realize high-performance Pb-free PSC devices. For perovskite-derived materials, including Cs_2SnI_6, $Cs_3Bi_2I_9$, $Cs_3Sb_2I_9$, $Cs_2BiAgCl_6$, $Cs_2BiAgBr_6$, and so on, although theoretical calculations have predicted that those derived perovskites have ideal bandgaps to achieve high solar-to-electric conversion efficiency, the PCEs of photovoltaics assembled based on these materials are generally

Table 2 Phase stability of $CsPbI_3$ modified by various strategies under various conditions

Type	Phase stability	Ref.
$CsPbI_3$ (HI) planar	<1 day	85
$CsPbI_3$ QDs	>60 days (dry)	128
PVP-passivation $CsPbI_3$	>500 h	138
PEA^+	>100 h (dry)	135
PEA^+	>200 h (dry)	137
$CsPbI_3 \cdot 0.025EDAPbI_4$	>35 days (dry)	132
Sulfobetaine zwitterions	>30 days	134
PEA^+	>40 days	111
2D $BA_2CsPb_2I_7$	>30 days	136
SCG-$CsPbI_3$	>500 h	139
μGR/$CsPbI_3$ QDs	>30 days (N_2)	180
CHI/$CsPbI_3$	>500 h (N_2)	144

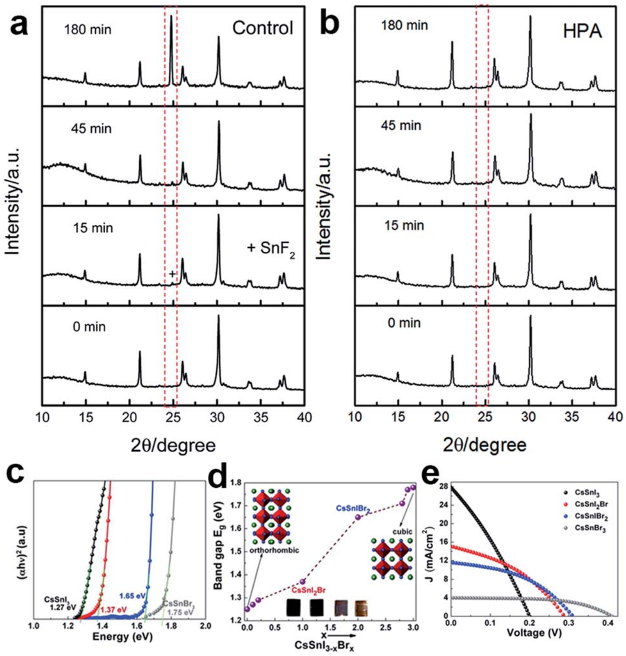

Fig. 12 XRD pattern of SnF_2-doped $CsSnIBr_2$ prepared: (a) without and (b) with HPA. (c) Tauc plots, (d) the bandgap, and (e) J–V curves of $CsSnI_{3-x}Br_x$ and corresponding devices with different x values.[190,191]

around 3%, even after optimizing the element ratio of X site and when improving the film quality.[194,195] All in all, great breakthroughs may be achieved by developing suitable synthetic routes to fabricate these novel materials in the future.

After comparing various inorganic PSCs, it can be seen that the advantages and deficiencies are typically concomitant. Taking $CsPb(I_{1-x}Br_x)_3$ into consideration, generally, when $x < 0.2$, the I-rich phase is preferred insulating the δ phase at room temperature; when $x > 0.4$, the light-induced segregation dominates under irradiation. To date, the best recorded efficiency of inorganic PSC device that has been achieved is 18.4% for $CsPbI_3$ perovskite, and 16.37% for $CsPbI_2Br$ perovskite, and 10.91% for $CsPbBr_3$ perovskite. For Pb-free devices, the photovoltaic performance is still unsatisfactory. Taking all parameters together, $CsPbI_2Br$ films may be regarded as the best choice for inorganic PSCs by balancing the stability and efficiency.

4. Compositional engineering

Although cesium lead halide perovskite is regarded as an alternative light absorber, the nonuniform film coverage, high trap state density, and phase instability still degrade the photovoltaic performances of the corresponding devices fabricated with this material. Doping inorganic perovskites with a smaller ion leads to a reduction of the lattice constants and thus to the contraction of the cubic volume, which has been proved to be an efficient strategy to further enhance the overall photovoltaic performance of inorganic PSCs. Fig. 13 summarizes the radii of ions that have been used in doping engineering and the inner mechanism of A-site and B-site substitutions.

4.1 A-site substitution

A general recognized mechanism involves adjusting the A-site cations to contract the sizes of the octahedral voids, with an aim to obtain an ideal cubic perovskite phase with a Goldschmidt's tolerance factor (τ) of 1, and thus stabilizing the perovskite phase.[114,196] Therefore, the composition of the A-site is crucial for effective PSC devices. Incorporating alkali metal cations has also been systematically studied in hybrid perovskite system, displaying a positive effect on the final photovoltaic performance. Liu's group systematically demonstrated that A-site substitution with alkali metal ions could dramatically improve the perovskite quality by enlarging the grain sizes, reducing the defect state density, passivating the grain boundaries, and increasing the built-in potential (V_{bi}).[196] Various alkali metal ions with smaller ionic radii have been discovered to substitute for Cs^+, as shown in Fig. 13b, with an aim to enhance the photoelectric properties of inorganic perovskite solar cells. The first group to kick off the alkali metal doping way was Park's group in inorganic PSCs by means of incorporating potassium cations (K^+) into the $CsPbI_2Br$ lattice.[114] After optimizing the doping dosage, as shown in Fig. 14a and b, the largest shift of the XRD characteristic peak position to a higher angle was

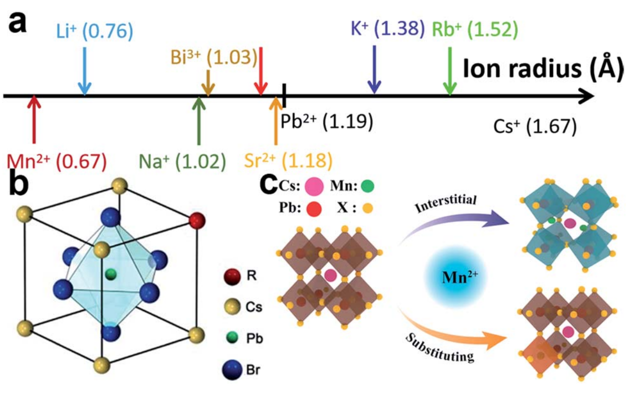

Fig. 13 (a) The ion radii of various metal ions. Illustrated crystal structure for (b) A-site and (c) B-site substitutions.

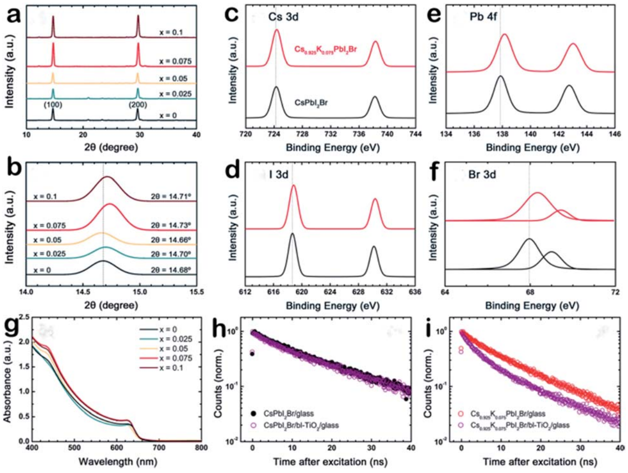

Fig. 14 (a) XRD patterns and (b) Gaussian fitting curves for the (100) peaks of $Cs_{1-x}K_xPbI_2Br$ films (x = 0, 0.025, 0.05, 0.075, 0.1). XPS spectra of $CsPbI_2Br$ (black) and $Cs_{0.925}K_{0.075}PbI_2Br$ (red) for (c) Cs 3d, (d) Pb 4f, (e) I 3d, and (f) Br 3d. (g) Absorbance spectra of $Cs_{1-x}K_xPbI_2Br$ films (x = 0, 0.025, 0.05, 0.075, 0.1). Time-resolved PL decay profiles of (h) $CsPbI_2Br$ and (i) $Cs_{0.925}K_{0.075}PbI_2Br$ films with and without a bl-TiO_2 layer.[114]

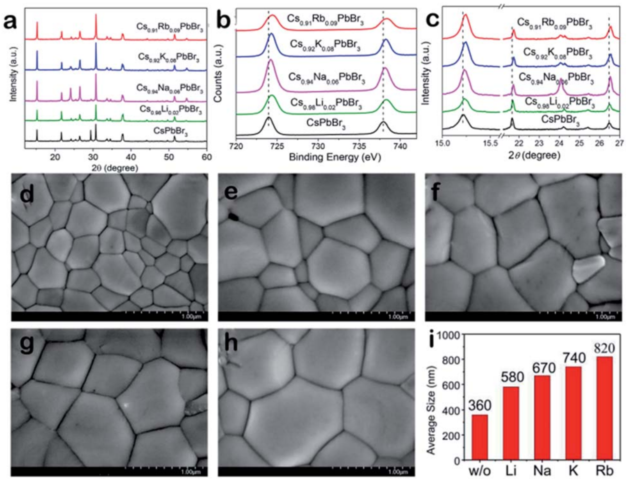

Fig. 15 (a) XRD patterns for $Cs_{1-x}R_xPbBr_3$ films. (b) XPS spectra of Cs 3d for various alkali metal cations-doped perovskite films. (c) Enlarged comparison of the (100), (110) and (111) diffraction peaks. Top-view SEM images of the (d) $CsPbBr_3$, (e) $Cs_{0.98}Li_{0.02}PbBr_3$, (f) $Cs_{0.94}Na_{0.06}PbBr_3$, (g) $Cs_{0.92}K_{0.08}PbBr_3$, and (h) $Cs_{0.91}Rb_{0.09}PbBr_3$ films. (i) Grain statistical distribution of five different films based on the top-view images.[90]

observed upon a closer look for the (100) peak of $Cs_{0.925}K_{0.075}PbI_2Br$, which could be correlated with a significant decrease in the lattice constant from 6.0341 Å to 6.0137 Å, resulting in the contraction of the cubic volume and a significant stabilization of the perovskite phase.[197] Furthermore, the increased XRD peak intensity indicated an increase in the crystallinity, whereby the preferred orientation was arranged. The binding energy for Pb 4f and Br 3d shifted from 137.8 to 138.2 eV and 67.95 to 68.35 eV owing to the changed interaction between the elements (see Fig. 14c–f) after doping with K^+, respectively. Arising from the smaller ion radius of potassium (1.38 Å) than cesium (1.67 Å), the volumetric ratio between PbX_6 octahedra and A-site cations for $Cs_{0.925}K_{0.075}PbI_2Br$ could be well-tuned, leading to an enhancement of the phase stability of perovskites. A significant increase in absorbance intensity and the enhancement of charge extraction could also be viewed from Fig. 14g–i, which were highly dependent on the optimization of the as-prepared perovskite film.

According to the passivation effect of potassium cations, the defect state density could be significantly reduced, such as the halide vacancy in the grain boundaries or in the interior of the perovskite film.[198] The non-radiative losses could be dramatically eliminated owing to the suppressed recombination, thereby enhancing the external photoluminescence quantum yield as well as the corresponding photovoltaic conversion efficiency. Finally, a device with the architecture of FTO/bl-TiO_2/$Cs_{0.925}K_{0.075}PbI_2Br$/Spiro-OMeTAD/Au yielded an enhanced efficiency as high as 10.0%, demonstrating the feasibility to regulate the lattice and defect state density.

More recently, Tang's group comprehensively studied a series of alkali metal ions (Li^+, Na^+, K^+, and Rb^+) with smaller ionic radii as dopants to modulate the film quality of all-inorganic $CsPbBr_3$ perovskite films.[90] As shown in Fig. 15, the characteristic peaks shifted to higher binding energy and the diffraction angle could also be discovered, confirming the contraction in the perovskite cubic volume. By optimizing the doping amount, the grain size could be enlarged to 820 nm from the pristine 360 nm size, as shown in Fig. 15d–i, leading to the reduction of the grain boundaries, which would induce shallow states near the valence band edge and hinder hole diffusion. In this fashion, the recombination in perovskite films could be suppressed.[199] An unprecedented PCE of 9.86% and the long-term stability of the HTL-free $Cs_{0.91}Rb_{0.09}PbBr_3$ solar cell guarantee its further application.

4.2 B-site substitution

Can the partial substitution of Pb^{2+} (B-site) with other metal ions (from an extent of doping to alloying) stabilize the desired phase of $CsPbX_3$ (X = Cl, Br, I) perovskites without changing their optoelectronic properties? Considering the toxicity of Pb^{2+} in typical perovskite crystals, various bivalent nontoxic metal ions (such as Mn^{2+}, Zn^{2+}, Cd^{2+}, Co^{2+}, Sr^{2+}, Sn^{2+}, and alkaline earth metal ions)[70,113,116,126,197,200–202] and multi-valent nontoxic metal (such as Bi^{3+}, In^{3+}, Y^{3+}, Nb^{5+}, and lanthanide rare earth ions)[97,129,203–207] have been introduced into the perovskite lattice to partially substitute Pb^{2+}, realizing the optimization of the finally perovskite films. According to previous reports, the reduction of the bond length between B^{2+} and X^- can significantly enhance the stability of $CsPbX_3$ perovskites as well as the corresponding performance of photovoltaic devices owing to the optimized tolerance factor and enhanced formation energy for α-$CsPbI_3$ at room temperature and for the orthorhombic $CsPbBr_3$, respectively, as shown in Fig. 16a.[208] Zou *et al.* proved that Pb^{2+} substitution with Mn^{2+} could result in lattice contraction and enhance the formation energy by means of

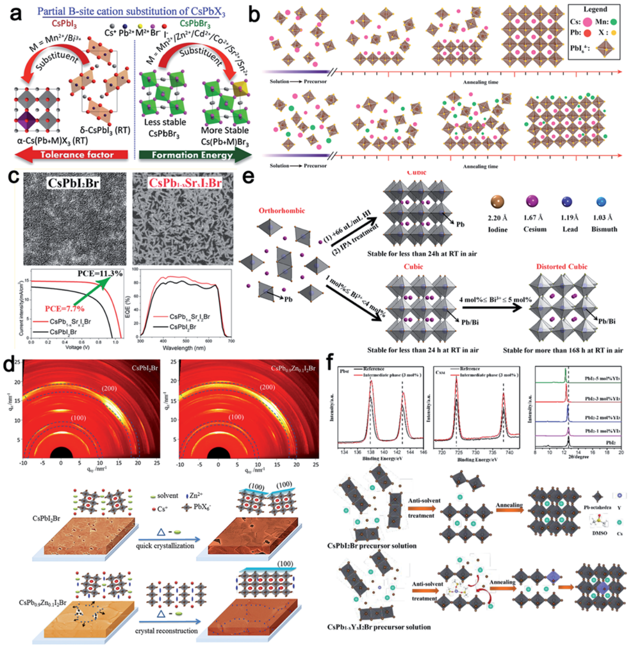

Fig. 16 (a) Schematic representation showing the effect of doping various ions into an inorganic perovskite lattice, such as increasing the tolerance factor and formation energy.[208] The characterization and crystallization processes of: (b) Mn^{2+}-,[116] (c) Sr^{2+}-,[113] (d) Zn^{2+}-,[126] (e) Bi^{3+}-,[129] and (f) Y^{3+} (ref. 207)-doped inorganic perovskite films and corresponding devices.

theoretical calculations, thus fundamentally stabilizing the perovskite lattices.[197] Besides, by inserting Mn^{2+} ions into the interstices of the $CsPbI_2Br$ lattice, the aspect ratio of the $CsPbI_2Br$ crystalline grains could be enhanced as high as 8, as developed by Liu's group (Fig. 16b). Arising from the reduced trap density, when the $MnCl_2$ concentration was increased to 2%, the PCE reached a maximum of 13.47% (as well as a V_{OC} of 1.172 V, a J_{SC} of 14.37 mA cm^{-2}, and an FF of 80.0%).[116] In theory, the valence band maximum is mainly determined by the antibonding hybridization B 6s and X *n*p orbitals with dominant contributions from X *n*p, while the conduction band minimum is mainly determined by the antibonding mixing of B 6p and X *n*p orbitals with the dominant contribution from B 6p.[209] Following this line of thought, B^{2+} doping can tune the band structure of all-inorganic perovskites. Indeed, upon introducing Mn^{2+} into the $CsPbIBr_2$ lattice, the valence band maximum values of perovskite films could be regulated from pristine −5.39 eV to −5.22 eV, reducing the energy barrier for effective photogenerated holes extraction. When assembling into a carbon based device, an enhanced efficiency of up to 7.36% could be achieved, with an increase of 19.9% in PCE compared to a control device.[200]

Partially substituting Pb with Sr has also proved to be an effective strategy to optimize the perovskite film quality. The PCE of $CsPb_{0.98}Sr_{0.02}I_2Br$ solar cells increased from 6.6% (for $CsPbI_2Br$) to 11.3%, with a V_{OC} of 1.07 V, a J_{SC} of 14.9 mA cm^{-2}, an FF of 0.71, and a stabilized efficiency of 10.8%. Sr-doped $CsPbI_2Br$ showed better thermal stability and a large grain size (Fig. 16c).[113] This was the first demonstration of a low-temperature-processed $CsPbI_2Br$ perovskite solar cell that had comparable efficiency to the high-temperature-processed Cs perovskite cells. Meanwhile, Ca^{2+} displayed a similar effect on enlarging the perovskite grain size and reducing the film roughness.[202] According to previous reports, incorporating isovalent small ions to increase the stability and suppress the formation of atomic vacancies has been proved to be an effective strategy in hybrid perovskite systems.[210] Zn^{2+}, which has a stronger interaction to halide ions, can effectively manipulate the crystal growth and enlarge the grain size of $CsPbI_2Br$ with enhanced growth orientation, resulting in reduced grain boundaries and accelerated charge transfer. The mechanism behind this phenomenon is mainly attributed to the controlled nucleation and crystalline growth processes, as shown in Fig. 16d. Arising from the interaction between Zn^{2+} and the adjacent I^- and Br^-, the formed crystals easily coalesce and grow together into bigger domains.[126] Similarly, Tang's group explored the alkaline earth metal ions, such as Mg^{2+}, Ca^{2+}, Sr^{2+}, Ba^{2+}, as dopants to modulate the $CsPbBr_3$ crystal structure, and found they could improve the PCE up to 9.68%.[201] By characterizing the recombination within the device, it was discovered that the defect state density could be significantly reduced, demonstrating that doping B^{2+} ions in $CsBX_3$ film is effective at enhancing the photovoltaic performance of all-inorganic PSCs.

Many works have reported that doping appropriate ions can further stabilize the perovskite lattice owing to the increased formation energy, which will in turn improve the solar-to-electric conversion ability. For example, in order to avoid the undesirable phase degradation from α-$CsPbI_3$ to the non-perovskite yellow phase δ-$CsPbI_3$ at room temperature, Zhang's group incorporated 4 mol% Bi^{3+} ions into a $CsPbI_3$ precursor solution, obtaining a controlled α-$CsPbI_3$ film with the typical cubic structure (*Pm*3*m*).[129] Along with the increase in doping dosage, the grain size was gradually decreased, similar to the Eu^{3+}-doped $CsPbI_2Br$ system,[205] which was beneficial for the enhancement of the long-term stability (Section 3.1.4). After systematically optimizing the doping dosage, a recorded efficiency up to 13.21% with excellent stability was obtained. The mechanism behind this phenomenon was similar to HI addition or IPA treatment. As shown in Fig. 16e, with the increase in the Bi^{3+} component, a small microstrain (distorted cubic structure) will be induced in the crystals owing to the smaller ionic radius, hindering the transition from α-$CsPbI_3$ to δ-$CsPbI_3$. Different from Bi^{3+} ions doping, recently, it was found that yttrium ions (Y^{3+}), as a dopant, could expand the PbI_2 interlayer, allowing DMOS molecules into the PbI_2 planes as a result of the interaction between Y^{3+} and DMSO, which in turn suppressed DMSO evaporation and tuned the film growth process (Fig. 16f).[207] As a result, a much enhanced power conversion efficiency (PCE) of 13.25% could be achieved. Besides the efficiency, the long-term stability of the corresponding device could also be well enhanced owing to the stable crystal lattice. The corresponding stabilities of various ions-doped devices are summarized in Table 3.

For trivalent metal ions as dopants, it should be noted that trivalent metal ions are more difficult to substitute for Pb^{2+}

Table 3 Phase stability of doped perovskites with various metal ions under various conditions

Sample	Phase stability	Condition	Ref.
$CsPb_{0.96}Bi_{0.04}I_3$	>6 days	Ambient	129
$CsPb_{0.98}Sr_{0.02}I_2Br$	>30 days	Encapsulated	113
$CsPb_{0.9}Sn_{0.1}IBr_2$	>100 days	Encapsulated	70
$Cs_{0.925}K_{0.075}PbI_2Br$	>6 days	Ambient	114
$Cs_{0.91}Rb_{0.09}PbBr_3$	>30 days	Ambient	90
$CsPbI_2Br(Mn^{2+})$	>35 days	Ambient	116
$CsPb_{0.97}Sm_{0.03}Br_3$	>60 days	Ambient	97
$CsPb_{0.95}Eu_{0.05}I_2Br$	>300 h	Light	205
$CsPb_{0.9}Zn_{0.1}I_2Br$	>400 h	N_2, 65 °C	126

owing to their unequal electric valence. Therefore, during the formation of the perovskite film, more highly ionic metal cations are believed to be predominantly expelled to the surface and grain boundaries, such as Al^{3+} and lanthanide ions (Ln^{3+}).[97,211] Various Ln^{3+} ions, including La^{3+}, Ce^{3+}, Nd^{3+}, Sm^{3+}, Eu^{3+}, Gd^{3+}, Tb^{3+}, Ho^{3+}, Er^{3+}, Yb^{3+}, and Lu^{3+}, have been successfully incorporated into the $CsPbBr_3$ perovskite lattice to further increase the performance of the corresponding device. By optimizing the doping amount and Ln^{3+} ion species, a device with the architecture of FTO/c-TiO_2/m-TiO_2/$CsPb_{0.97}Sm_{0.03}Br_3$/carbon yielded a champion efficiency as high as 10.14% with a superior open-circuit voltage of 1.594 V, mainly attributed to the enlarged grain size and reduced recombination within solar cells. However, not all Ln^{3+} ions display a positive effect on enhancing the photovoltaic performance. Among them, Lu^{3+}, Gd^{3+}, La^{3+}, Ce^{3+}, Nd^{3+}, or Eu^{3+} have a nearly unchanged effect on device performance, even dragging the PCE down. Therefore, there may be other mechanism behind Ln^{3+} doping of perovskite films owing to their unique multi-energy level construction.

To date, employing compositional engineering to dope an impurity into the all-inorganic perovskite lattice is reported to be an effective strategy to relax the lattice strain and passivate defects. However, no matter whether replacing the A-site or B-site, the doping amount should be carefully controlled. Excessive impurities will destroy the lattice construction of the perovskite, leading to a degradation of the final device performance.

5. Film-making methods

Perovskite film is the heart of an efficient PSC device; therefore, how to make a high-quality perovskite layer with a large grain size and high film coverage is a prerequisite to enhance the PCE output and the stability of inorganic PSCs. Considering the radiative and non-radiative recombination in perovskite films, tremendous studies are emerging concerning perovskite-making pathways. One basic principle is to combine two inorganic components, *i.e.*, PbI_2/$PbBr_2$ and CsI/CsBr, to form $CsPbI_{3-x}Br_x$ perovskite films. In general, the as-developed methods can be divided into three categories according to the film-formation process: one-step, two-step, and multi-step deposition methods. In this section, we discuss the development and advantages of these methods.

5.1 One-step deposition method

Similar to the organic–inorganic hybrid perovskite films, the inorganic $CsPbI_{3-x}Br_x$ perovskite films can also be made by a classical one-step method through directly depositing precursor sources, including *via* the spin-coating technique and physical vapor deposition (co-evaporation) technique.

Among the different film-making techniques, the solution-processable technology represents the mainstream method owing to its low-cost, facile processes, and scalable space in producing high-quality perovskite films and therefore high-performance PSCs. To the best of our knowledge, the one-step solution deposition method was first proposed by Snaith and Grätzel to form a film of an organic–inorganic perovskite.[42,212] Later in 2015, Snaith and co-workers successfully prepared a black phase $CsPbI_3$ film by spin-coating a CsI : PbI_2 solution (1 : 1 in a molar ratio) in *N*,*N*-dimethylformamide (DMF) at a heating temperature of 335 °C, and the as-prepared inorganic $CsPbI_3$ film maintained its stability for a period of a few weeks.[85] However, the heating temperature of 335 °C is relatively high for practical photovoltaic applications. They subsequently proposed an additive method by adding a small amount of hydroiodic acid (HI) to the precursor solution to enhance the solubility of perovskite precursors, allowing for the growth of pinhole-free perovskite layers at only 100 °C for 10 min. However, its ambient instability still remained, limiting the fabrication and application of $CsPbI_3$ in an air atmosphere. Aiming to resolve the issue of stabilizing black perovskite $CsPbI_3$, Lu *et al.* modified the one-step spin-coating method by adding a subsequent solvent engineering process with isopropanol (IPA) treatment, achieving a novel low-temperature phase-transition route from a new intermediate Cs_4PbI_6 to stable α-$CsPbI_3$ for the first time in an air atmosphere.[133] So far, this one-step spin-coating technique has been considered universally applicable to fabricate uniform thin films of Cs-based perovskites with a high iodide content, such as $CsPbI_3$ and $CsPbI_2Br$.[111] Later, Mai *et al.* modified the one-step spin-coating method by adding a gradient thermal treatment process: first, the spin-coated film was placed on a hotplate at 30 °C to form the stable transition film; second, the temperature was increased to 160 °C for 20 min to remove the surplus solvent and to improve the crystallization quality, as shown in Fig. 17a and b. Though the PCE was inferior than that of other inorganic PSCs, it indeed demonstrated that a post-annealing procedure was essential to reduce the Schottky barrier and interface defect state.[106] Subsequently, they used the same film-making method to fabricate all-inorganic $CsPbI_2Br$ PSCs with an inverted FTO/NiO_x/$CsPbI_2Br$/ZnO@C_{60}/Ag structure by introducing ZnO@C_{60} bilayer electron transfer layer, achieving a PCE of over 13.3% and a remarkably stabilized power output of 12% within 1000 s. Importantly, the device free of encapsulation exhibited long-term thermal stability, with only 20% of the PCE quenched after being heated at 85 °C for 360 h.[120]

During the growth of perovskite films, two processes determine the film quality: the first nucleation step and the crystal growth step, which are highly dependent on the solubility of the perovskite precursor and the solvent evaporation rate,

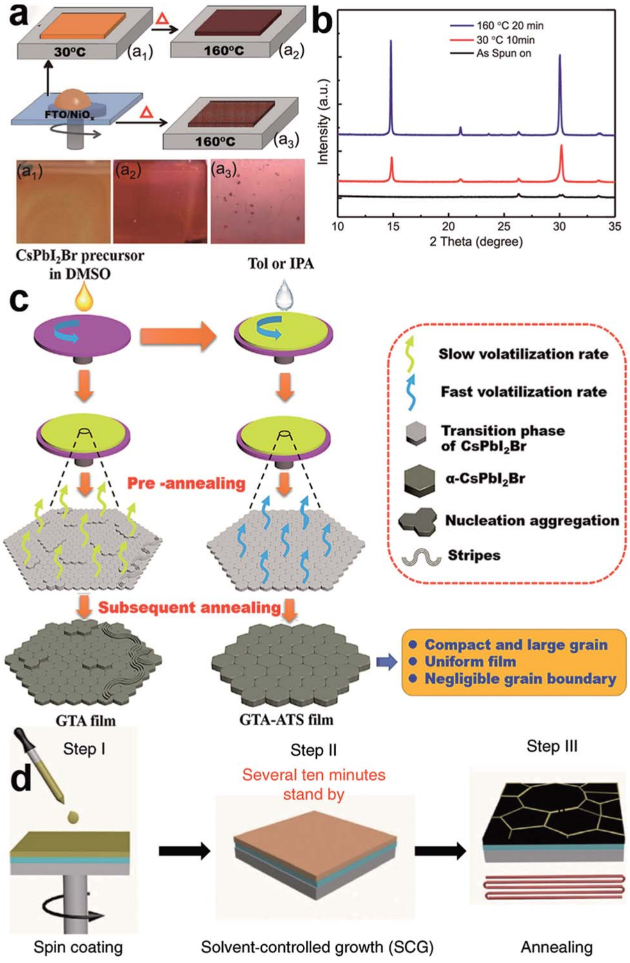

Fig. 17 (a) Schematic view of the gradient thermal treatment process, and (b) XRD spectra of as-prepared perovskite films fabricated with different methods. (c) Illustration of the gradient thermal annealing processes with anti-solvent treatment by Tol and IPA. (d) Schematic of SCG technology.[106,124,139]

respectively. Following this line of thought, the precursor solution temperature is another crucial parameter for suppressing the formation of too many nuclei and for increasing the crystallization rate. Liu's group systematically studied the relationship between crystallization and the fabrication temperature, and found that a precursor solution temperature fixed at 100 °C could dramatically enlarge the grain size of a $CsPbI_2Br$ film.[213] When assembling into a planar architecture device, a maximum PCE of up to 14.81% was achieved, demonstrating the importance of temperature in one-step spin-coating technology.

According to the above-mentioned discussion, precise control of the crystal growth plays a crucial role in obtaining high-quality perovskite films. Therefore, gradient thermal annealing (GTA) was further developed by Chen *et al.*, in which the phase conversion was conducted under 50 °C for 1 min, 100 °C for 1 min, and then 160 °C for 10 min, as shown in Fig. 17c.[124] When further processing the film with anti-solvent (ATS) treatment, such as toluene (Tol) and isopropanol (IPA), a high-quality $CsPbI_2Br$ film with increased average grain sizes and reduced defect density could be obtained, which was mainly attributed to the rapid extraction of the residual solvent by isopropanol. Finally, a record efficiency of up to 16.07% was achieved. Strikingly, You's group further improved the one-step spin-coating method with an intermediate solvent-controlled growth, called SCG, to obtain $CsPbI_3$-perovskite films free of pinholes and a crystal size above 5 μm.[139] SCG, in detail, refers to the process whereby the precursor films were stored in a nitrogen glove box for several tens of minutes before annealing on a hotplate (Fig. 17d). This stagnation allowed the residual DMSO to improve the film quality by enhancing the mass transport and diffusion, achieving the champion PCE (15.7%) of $CsPbI_3$ perovskite solar cells; further, there was no change in the XRD patterns or absorption spectra after 7 days of storage.

In summary, there are dozens of reports about depositing high-quality perovskite films with a large grain size by a one-step method. The growth of perovskite film follows the “Volmer–Weber” growth mode, accompanied with a classic “heterogeneous” nucleation process and grain growth theory. In detail, the number of grains per unit area (Z) is determined by the nucleation formation rate (ν_n) and the crystal growth rate (ν_c), following the formula: $Z \propto (\nu_n/\nu_c)$, where Z is inversely proportional to the grain size. Therefore, retarding the nucleation process and accelerating the grain growth process are two strategies to increase the film quality. To date, the one-step method has been applicable to most cesium perovskites, such as $CsPbI_3$, $CsPbI_2Br$, and even $CsPbIBr_2$, but not for $CsPbBr_3$, owing to its inferior solubility.

Although the solution-processable method provides great advantages to establish an ideal perovskite film, the environmental conditions during perovskite film formation, such as temperature, precursor solubility, atmosphere, annealing time, and so on, lead to an inferior repeatability. In order to overcome these issues, the physical co-evaporation technique was further attempted to obtain an inorganic perovskite light-harvesting layer by Ho-Baillie *et al.*[104] As is well known, a dual source thermal evaporation technique was first employed in a hybrid perovskite system.[214] In detail, an equal molar of CsX and PbX_2 were simultaneously evaporated onto an FTO glass substrate supported electrode, leading to the successful crystallization of a $CsPbX_3$ perovskite film. This physical process did not involve any solvents, therefore, there was no solvent residue left in the film and so this technology is applicable to deposit insoluble materials. Troshin and co-workers prepared $CsPbI_3$ films by thermally co-evaporating CsI and PbI_2 precursors under a vacuum environment for planar heterojunction inorganic PSCs (Fig. 18a).[130] Different from spin-coated films, the low-temperature brown perovskite phase of $CsPbI_3$ is a particular feature for vacuum thermal co-evaporation processes, as it is unstable and undergoes an irreversible transformation to a yellow phase under heating at temperatures above 60 °C. On the contrary, when heated up to 320 °C, the yellow phase undergoes a phase transition back to the black phase, which is depicted in Fig. 18b. Film annealing at 320 °C offers the best optimal light absorbance, which is consistent with the phase

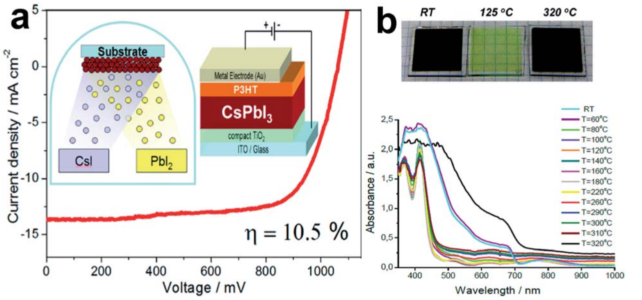

Fig. 18 (a) Illustration of the dual-source co-evaporation technique. (b) Optical images and absorbance spectra of $CsPbI_3$ films under various temperatures, and colorimetric observation of the color change from brown to yellow and then to black phase at higher temperatures.[130]

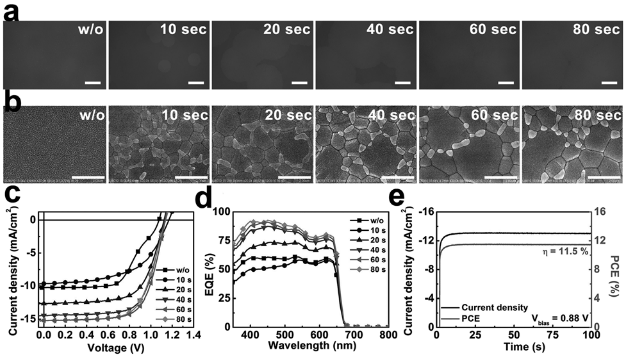

Fig. 19 Top-view scanning electron microscopy images of $CsPbI_2Br$ films annealed at different times at 260 °C. Scale bar: (a) 100 μm and (b) 2 μm. (c) Corresponding *J*–*V* curves and (d) EQE spectra measured under one sun AM 1.5G illumination. (e) Photocurrent density and PCE as a function of time of the champion $CsPbI_2Br$ solar cell under the bias of 0.88 V.[115]

transition temperature from the orthorhombic yellow phase to the cubic black phase. After annealing, the film quality can be significantly optimized, with an increased grain size up to 1–3 μm. In this fashion, it is obvious that the annealing temperature is still necessary for fabricating a high-quality perovskite film. The perovskite films prepared by the co-evaporation method present few impurity defects and a dense and uniform surface. However, this method requires a high vacuum and high-strength equipment as well as large energy consumption.

Vacuum co-deposition is the third technique to make inorganic perovskite films; for example, Lin *et al.* prepared $CsPbI_3$ and $CsPbI_2Br$ films with the aid of the physical vapor behavior of sublimed cesium-based perovskite precursors.[115] Since the smooth CsI surface dramatically changes to a rough and diffusive appearance when exposed to air, a vacuum chamber with observation and measurement windows is utilized to avoid air exposure during the formation of the perovskite phase. Through tuning the annealing time, the best $CsPbI_2Br$ solar cell showed a promising PCE of 11.8%, with a V_{oc} of 1.13 V, J_{sc} of 15.2 mA cm^{-2}, and FF of 0.68. This method has advantages of a precise deposition rate and accurate molar ratio of precursor materials, as shown in Fig. 19, which are critical for device performance, leading to small hysteresis and superior stability.

Meanwhile, taking the different solubilities of components into consideration, especially for double perovskites with a complex composition, vapor-deposited technology shows great potential for high-quality perovskite films as well as for fabricating lead-free semiconductors. Liu's group successfully developed a sequential-vapor-deposition method to fabricate an all-inorganic double perovskite $Cs_2AgBiBr_6$ film, and a maximum PCE of 1.37% was achieved.[215] Compared to solution-processable methods, physical-vapor-deposition demonstrates universal applications in photovoltaic areas.

5.2 Two-step deposition method

In general, the development of inorganic perovskite films follows the same steps as organic–inorganic hybrid perovskites, in which a two-step spin-coating technique has been widely employed for fabricating a high-quality perovskite layer. To date, the two-step or multi-step deposition method (will be discussed in the following part) has been mainly employed to fabricate Br-rich all-inorganic perovskites owing to the solubility limitations of Br^- ions in conventional solvent, which leads to perovskite films with B-rich compositions being difficult to be obtained. Hodes *et al.* proposed that the two-step spin-coating technique can be used to form cesium lead halide perovskites.[84] In detail, the first step is to spin-coat lead bromide solution in DMF onto a mesoporous TiO_2 scaffold and to then dry at 70 °C. Subsequently, these lead bromide films are dipped in a heated solution of the cesium halide salt(s) in methanol for 10 min, thereby realizing the successful perovskite formation. Meanwhile, Jin's group also employed this method to assemble a carbon-based device with the architecture of FTO/c-TiO_2/m-TiO_2/$CsPbBr_3$/carbon, obtaining an efficiency of 6.7% together with excellent long-term stability.[88] However, the uncontrollable dipping process drags down the reproducibility and high-quality film formation. To address these issues, Chen *et al.* systematically explored the relationship between the $CsPbBr_3$ film quality and dipping time as well as the reaction temperature, demonstrating tat the morphology and composition was highly dependent on the two parameters. Finally, the PCE could be increased to 3.9% from the pristine 1.3% after optimizing the reaction time and temperature.[86] In fact, the phase of the perovskite film obtained by this method is complicated. Therefore, Yu and coworkers modified this two-step method by introducing a face-down dipping process to restrict the decomposition of the unwanted precursor films in solution and to fabricate high-quality $CsPbBr_3$ perovskite films with an average grain size of 860 nm.[216] Fig. 20 illustrates the differences in depositing perovskite films, and therefore inorganic perovskite film structures, between the face-up dipping and face-down dipping process.

Most reported $CsPbBr_3$ films are prepared by a solution process; however, the rapid liquid-phase reaction is hard to control, resulting in an inferior perovskite film with enormous pores and notorious efficiency. Therefore, employing an intermediate phase to modulate the final perovskite quality is an

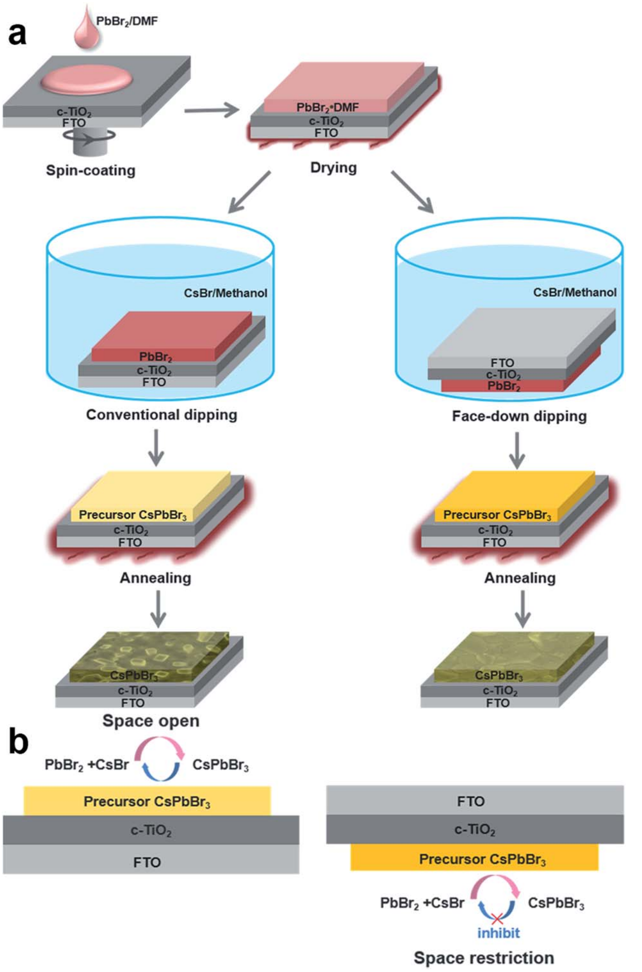

Fig. 20 (a) Fabrication processes for $CsPbBr_3$ films by a dipping process and face-down dipping methods. (b) Mechanisms of the dipping reaction by a face-up dipping and face-down dipping process.[216]

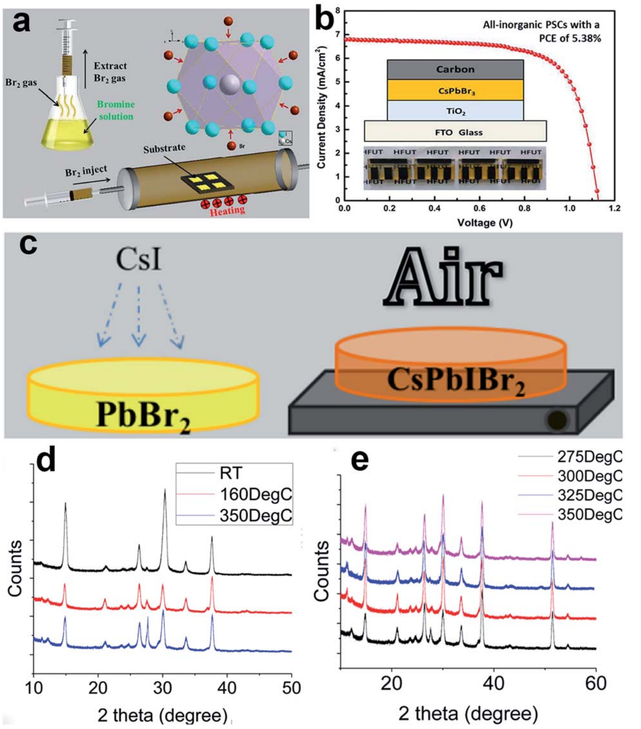

Fig. 21 (a) Extraction of Br_2 vapor from a bottle of bromine solution; Br_2-vapor-assisted CVD process and reaction process; (b) solar cell architecture and J–V curve obtained in a reverse scan.[87] (c) Illustration of the spray-assisted deposition of $CsPbIBr_2$ perovskite film and (d)–(e) XRD spectra of $CsPbIBr_2$ perovskite films prepared under different conditions.[105]

effective strategy. Inspired by the rapid reaction between $MAPbI_3$ and gaseous Br_2 and HBr,[146] Sun *et al.* fabricated a $CsPbBr_3$ perovskite film with a Br_2-vapor-assisted CVD method, as shown in Fig. 21a, in which fast anion exchange from $CsPbI_3$ to $CsPbBr_3$ could be realized owing to the effective incorporation of Br^- into $CsPbI_3$ inorganic perovskites in a few of seconds.[87] First, the $CsPbI_3$ precursors were spin-coated onto the FTO/c-TiO_2/m-TiO_2 substrates, and then transferred into a quartz tube furnace. After pumping the quartz tube for 5 min, the $CsPbI_3$ precursors were heated to 150 °C and then Br_2 vapor was injected into the hot quartz tube for reaction. Finally, the perovskite films were taken out and rinsed with isopropanol, and annealed in ambient air to obtain a bright yellow $CsPbBr_3$ layer. Finally, a relatively high PCE of up to 5.38% (Fig. 21b) was achieved based on this $CsPbBr_3$ all-inorganic perovskite solar cell with carbon as the back electrode. The perovskite layer made by the vapor-assisted method always features high coverage, a smooth surface, and tiny grain size, thus reducing the surface recombination rate during carrier transportation and thereby achieving a high V_{oc} output. Moreover, the vapor-assisted technique does not need special requirements, it is economical and environmental compared to the co-evaporation or solution-processable spin-coating methods.

Perovskite-structured quantum dots (QDs) have also been applied to assemble perovskite films for photovoltaic applications, and are beneficial for eliminating the inconclusive self-assembly crystallization processes as determined by different factors including the precursor ratio, solvent, processing additives, substrate roughness and surface energy, atmospheric/environmental conditions, annealing temperature, and treatment time. To the best of our knowledge, $CsPbI_3$ QDs have recently been utilized to stabilize the crystal phase for the first time, which was discussed in Section 3.1.4.[128] By spin-coating QDs onto the surface of TiO_2 film, a high V_{oc} of 1.23 V and efficiency of 10.77% were obtained, demonstrating the great potential for enhancing the overall photovoltaic performance of all-inorganic PSCs. Subsequently, a $CsPbBr_3$ QDs "ink" was developed to fabricate fully air-processed and stable solar cells, exhibiting an efficiency over 5% with high V_{oc} values.[157,217,218] This strategy may provide a new path to resolve the dissolution issue of the $CsPbBr_3$ precursor.

The uniform deposition and reliable anchoring of perovskite precursors in larger sizes often requires specific conditions, but spray-assisted deposition is regarded as a straightforward, fast, and cost-effective way to pattern substrates on a large scale. Ho-Baillie *et al.* demonstrated the feasibility of spray-assisted deposition to overcome the poor solubility of the bromide ion in one-step and two-step solution methods.[105] In this method, CsI was sprayed onto a spin-coated $PbBr_2$ layer under ambient conditions (see Fig. 21c). The substrate temperature during the spraying of CsI and the annealing temperature were found to be the most crucial parameters for the quality of the perovskite film. As depicted in Fig. 21d, the main peaks at 14.82°, 21.05°, and 29.94° corresponding to the (100), (110), and (220) planes of the $CsPbIBr_2$ perovskite orthorhombic phase could be clearly detected. With a much higher substrate temperature, the segregation of CsI (27.5°) became prominent. Fig. 21e demonstrates the crystallization of $CsPbIBr_2$ perovskite after annealing at 275 °C, 300 °C, 325 °C, or 350 °C for 10 min in atmospheric conditions, suggesting that a good annealing temperature range is from 275 °C to 350 °C. Using the optimized spray-assisted method, the best-performing inorganic FTO/bl-TiO_2/mp-TiO_2/$CsPbIBr_2$/Spiro-OMeTAD/Au PSC achieved a stabilized PCE of 6.3% with negligible hysteresis.

5.3 Multi-step deposition method

To date, the multi-step technology is generally employed to fabricate all-brominated $CsPbBr_3$ perovskite films. During the fabrication process of $CsPbBr_3$ perovskite films, $CsPb_2Br_5$ or Cs_4PbBr_6 will be formed when employing the traditional two-step solution-processed film-making technique. To effectively resolve this issue, a novel multi-step method to form a high-purity cesium lead bromide film with vertical and monolayer-aligned largest grains were proposed by Tang's group, leading to maximizing the charge transportation kinetics and therefore an increased PCE from 6.7% to 9.72% after incorporating GQDs.[89]

A schematic diagram of multi-step deposition technology is shown in Fig. 22a–d, involving a single $PbBr_2$ layer and the multi-step spin-coating of a CsBr layer. By tuning the number of deposition cycles with the CsBr solution, the components, crystal structure, and morphological alignment of the as-prepared perovskite films could be well controlled. From the SEM images, it could be seen that the film coverage and grain size were insufficient when the deposition number was low. Along with increasing the deposition number, an ideal perovskite film could be obtained when the deposition number was controlled at 4 times. The mechanism behind this phenomenon can be explained by the gradual phase conversion and crystal growth processes. Through characterizing the phases of as-prepared perovskite films with various deposition numbers of CsBr solution, the crystalline phase conversion during the multi-step process can be summarized into three reactions as follows:

$$2PbBr_2 + CsBr \rightarrow CsPb_2Br_5\ (n \leq 3) \tag{1}$$

$$CsPb_2Br_5 + CsBr \rightarrow 2CsPbBr_3\ (n = 4) \tag{2}$$

$$CsPbBr_3 + 3CsBr \rightarrow Cs_4PbBr_6\ (n \geq 5) \tag{3}$$

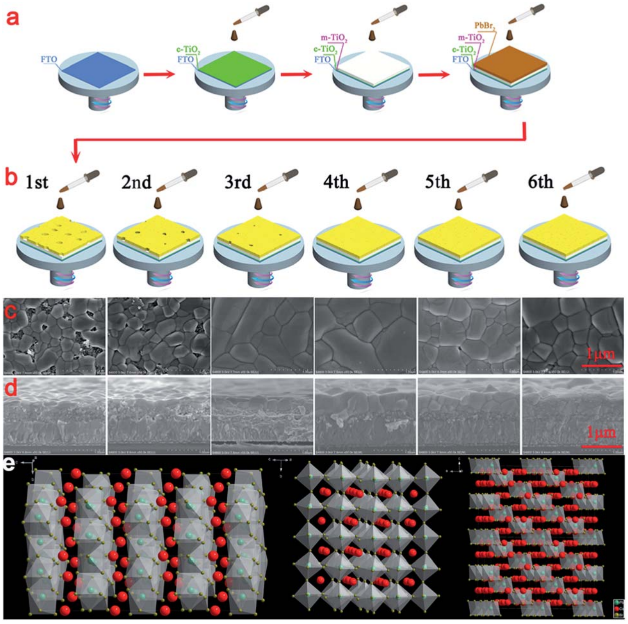

Fig. 22 (a) The steps of depositing c-TiO_2, m-TiO_2, and $PbBr_2$. (b) Multi-step solution-processed deposition of CsBr. (c) Top-view and (d) cross-sectional SEM images of the all-inorganic lead halide film. (e) Crystal structure of the cesium lead bromide halide.[89]

In this fashion, fewer CsBr coating cycles generally lead to the formation of a $PbBr_2$-rich $CsPb_2Br_5$-dominant film, while a higher number of CsBr coating cycles will accelerate the reaction of the $CsPbBr_3$ phase with CsBr to form a CsBr-rich Cs_4PbBr_6-dominant film. Therefore, by a precise control of the amount of CsBr, a high-purity inorganic perovskite film with a minimized mixed phase can be obtained. The thin film with vertical and monolayer-aligned grains has a lower density of defect states and fewer grain boundaries, and therefore the absorption layer is expected to further improve the device performance upon assembly into a photovoltaic device.

Similarly, spray-coating technology has been widely used in industrial processes due to its advantages in scaling up for large area cella.[219,220] Inspired by the above-mentioned conclusion, a multi-step spraying method was further developed to fabricate large-area solar cell devices by Tang's group.[98] Their studies revealed an identical phase conversion from $PbBr_2$-rich $CsPb_2Br_5$ to perovskite-structured $CsPbBr_3$ and further to CsBr-rich Cs_4PbBr_6 by spraying CsBr multilayers sequentially, which was in accordance with a previous report.[89] Following the above-mentioned discussion, an evaporation-assisted solution method was further developed, as shown in Fig. 23a. Based on their conclusion, the corresponding phase conversion from $CsPb_2Br_5$ to $CsPbBr_3$ and then to Cs_4PbBr_6 was also confirmed. By optimizing the CsBr deposition time and accelerating the charge transfer, a high efficiency of up to 10.45% was obtained.[102] Obtaining a high-purity $CsPbBr_3$ film provides a new avenue for making high-performance inorganic PSCs by multi-step spray-assisted method besides the commonly used one-step and two-step techniques, which require a high-temperature annealing process.

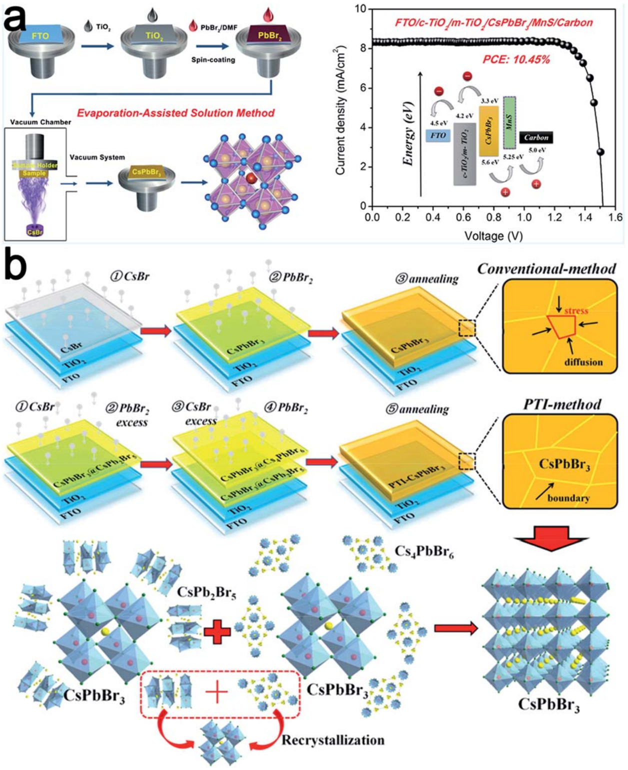

Fig. 23 Illustration on evaporation-assisted deposition and phase transition induced methods of $CsPbBr_3$ perovskite film.[102,103]

To further improve the efficiency of inorganic PSCs, many modifications have been developed recently. Liu *et al.* developed a facile and modified multistep spin-coating strategy, wherein the $PbBr_2$ film was first immersed into CsBr solution (two-step deposition method), with a subsequent spin-coating of a multi-layer of CsBr to realize a highly crystalline $CsPbBr_3$ film. Upon interfacial modification, a remarkable efficiency as high as 8.79% was obtained.[221] Meanwhile, Tong *et al.* constructed a gradient bandgap architecture of $CsPbBr_3$/$CsPbBr_3$–$CsPb_2Br_5$/$CsPbBr_3$–Cs_4PbBr_6 *via* thermal evaporation and spin-coating technology, achieving an enhanced efficiency of up to 10.17%.[101] Furthermore, they developed a strategy to fabricate high-efficiency $CsPbBr_3$-based PSCs by forming perovskite derivative phases ($CsPb_2Br_5$ and Cs_4PbBr_6) *via* a vapor growth method. During the post-annealing process, the derivative phases as nucleation sites are transformed to the pure $CsPbBr_3$ phase accompanied by crystal rearrangement and a retardation in the rapid recrystallization of perovskite grains. As shown in Fig. 23b, the phase transition-induced (PTI) method is beneficial for eliminating the internal stress and for lowering the surface potential barrier. Owing to the improved film quality, a PCE of 10.91% was achieved for n–i–p structured PSCs with silver electrodes, and a PCE of 9.86% for hole-transport-layer-free devices with carbon electrodes.[103] To date, it is obvious that a key advantage of halide perovskites among the various different high-performance semiconductors is their processability. As discussed in this section, a wide variety of strategies can be employed to fabricate all-inorganic perovskite films, providing more options on the path of commercialization.

6. Interfacial engineering

6.1 Theoretical analysis (the detailed balance model)

The detailed balance model is an indispensable tool for predicting the efficiency limit of solar cells.[222,223] The model only considers the detailed balance between absorbed photons and emitted photons. The current density of a solar cell is calculated as the difference between the photons radiating and the photons absorbed by the cell:

$$J = J_e(V) - J_{ph} \tag{2}$$

where V is the applied voltage, J_e represents the radiative recombination current, and J_{ph} is the photogenerated current due to the absorption of incident light in inorganic perovskite materials, *i.e.*,

$$J_{ph} = q\int_0^{\infty} a(\lambda, L)\frac{\Gamma(\lambda)\lambda}{hc_0}d\lambda \tag{3}$$

where c_0 is the speed of light in air, Γ is the global AM 1.5G spectrum of the Sun, λ is the wavelength, and q is the elementary charge, and $a(\lambda,L)$ is the absorptivity of the inorganic perovskite solar cell with an active perovskite layer thickness of L.

The absorptivity a is the ratio of power absorbed by the active layer over the power of incident sunlight, which depends on the thickness of the perovskite layer L, the refractive indices of the materials adopted, and the light-trapping structures. For solar cells having a planar front surface with a perfectly reflecting mirror on the rear, we have:

$$a(\lambda,L) = 1 - \exp[-2\alpha(\lambda)L] \tag{4}$$

Here, we ignore the reflection from the front surface, and α is the absorption coefficient of the active material. For solar cells having a randomly textured front surface with a perfectly reflecting mirror on the rear, the absorptivity can be written as:[224,225]

$$a(\lambda, L, \theta_m) = \frac{\alpha(\lambda)}{\alpha(\lambda) + \dfrac{\sin^2\theta_m(\lambda)}{4(n_r(\lambda))^2L}} \tag{5}$$

where n_r is the real part of complex refractive index of the active material, and θ_m is the maximum angle of emission (with respect to the normal of the front surface), *i.e.*, light escapes out of the solar cell within a cone with a solid angle of θ_m. For complex nanostructures, the absorptivity can be obtained by numerically solving Maxwell's equations. For the limiting efficiency (Shockley–Queisser limit) case,

$$a(\lambda) = \begin{cases} 1, \lambda \le \lambda_g \\ 0, \lambda > \lambda_g \end{cases} \tag{6}$$

where λ_g is the bandgap wavelength of the inorganic perovskite material. An ideal cell will absorb all the photons with energy above the bandgap energy.

According to the detailed balance theory and Boltzmann statistics, the radiative recombination current J_e can be expressed as:

$$J_e = J_{0e}\left[\exp\left(\frac{qV}{k_BT}\right) - 1\right] \tag{7}$$

where J_{0e} is the radiative saturation current, which is the minimum of the (reverse) saturation current. J_{0e} can be calculated by the blackbody radiation law:

$$\begin{aligned} J_{0e} &= q\int_0^{\infty} a(\lambda, L)\frac{\Gamma_0(\lambda, T)\lambda}{hc_0}\mathrm{d}\lambda \\ \Gamma_0(\lambda, T) &= \int_0^{2\pi}\mathrm{d}\varphi\int_0^{\theta_m(\lambda)} S(\lambda, T)\cos(\theta)\sin(\theta)\mathrm{d}\theta \\ &= \pi\sin^2\theta_m(\lambda)S(\lambda, T)\quad S(\lambda, T) = \frac{2hc_0^2}{\lambda^5}\frac{1}{\exp\left(\frac{hc_0}{\lambda k_BT}\right) - 1} \end{aligned} \tag{8}$$

where $\Gamma_0(\lambda,T)$ is the blackbody emission spectrum of the solar cell operated at the temperate T, and $S(\lambda,T)$ is the corresponding thermal radiance of the cell.

For a solar cell system, the dominated thermodynamic loss is caused by the non-radiative recombination, including the Shockley–Read–Hall (SRH) recombination (monomolecular recombination) and Auger recombination. The defects, impurities or deep-level traps at the bulk and interface will induce the SRH recombination, while the high carrier density by injection or generation will induce the Auger recombination, which always occurs in heavily doped inorganic semiconductors. Consequently, to describe the electrical response of a practical inorganic perovskite solar cell, the non-radiative recombination current should be introduced. Thus, eqn (2) should be modified as:

$$\begin{aligned} &J = J_{n,srh}(V) + J_{n,aug}(V) + J_e(V) - J_{ph} \\ &J_{n,srh}(V) = J_{0n,srh}\left(\exp\left(\frac{qV}{2k_BT}\right) - 1\right),\quad J_{0n,srh} = qC_{srh}Ln_i \\ &J_{n,aug}(V) = J_{0n,aug}\left(\exp\left(\frac{3qV}{2k_BT}\right) - 1\right),\quad J_{0n,aug} = qC_{aug}Ln_i^3 \end{aligned} \tag{9}$$

where $J_{n,srh}$ and $J_{n,aug}$ are the non-radiative recombination currents for the SRH and Auger recombination, respectively, C_{srh} and C_{aug} are the SRH and Auger recombination rates, respectively, and $J_{0n,srh}$ and $J_{0n,aug}$ are the non-radiative saturation currents for the SRH and Auger recombination, respectively.

One may approximate eqn (9) as a more compact form given by:

$$\begin{aligned} &J \approx J(V) - J_{ph} \\ &J(V) = J_0\left(\exp\left(\frac{qV}{mk_BT}\right) - 1\right) \end{aligned} \tag{10}$$

where J is the total recombination current including the radiative and nonradiative ones and m is the ideality factor, and J_0 is the dark current or saturation current, which should be the superposition of the radiative saturation current J_{0e} and the non-radiative saturation currents $J_{0n,srh}$ and $J_{0n,aug}$. From eqn (10), we can obtain the expression of V_{oc} for the inorganic perovskite solar cells:

$$V_{oc} = m\frac{k_BT}{q}\log\left(\frac{J_{ph}}{J_0}\right) \tag{11}$$

Thus, we can extract the ideality factor m to understand the recombination mechanism of the inorganic perovskite solar cells by investigating the light-intensity-dependent V_{oc} curve. Fig. 24 shows the V_{oc}–log(J_{ph}) curve for a $CsPbBr_3$ system, and m is approximate to 2. Therefore, the dominant recombination in inorganic PSCs is the SRH recombination.

Also, we can split the saturation current into radiative and non-radiative ones, *i.e.*,

$$\begin{aligned} &J_0 = J_{0e} + J_{0n,srh} + J_{0n,aug} = J_{0e} + J_{0n} = J_{0e}/\eta_{ELQE} \\ &\eta_{ELQE} = \frac{J_{0e}}{J_{0e} + J_{0n}} \end{aligned} \tag{12}$$

where η_{ELQE} is the external luminescence quantum efficiency (ELQE).[226] The ELQE is the number of photons emitted into free space over the number of electron–hole pairs generated by light absorption, which is a figure of merit for the photon recycling of inorganic perovskite solar cells.[227] Finally, we consider two circuit quantities involving the series resistance R_s, describing the ohmic loss from the interfaces and electrodes, and the shunt resistance R_{sh}, describing the shunt current resulting from the voids and defects. The two circuit parameters are essential to the fill factor of the inorganic perovskite solar cells. Incorporating the series and shunt resistances into the detailed balance model, the modified model can be written as:[228]

$$\begin{aligned} J = \frac{V - JR_s}{R_{sh}} &+ J_{n,srh}(V - JR_s) + J_{n,aug}(V - JR_s) \\ &+ J_e(V - JR_s) - J_{ph} \end{aligned} \tag{13}$$

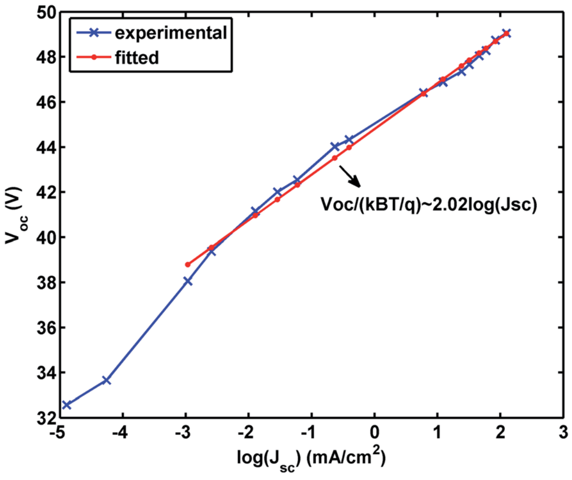

Fig. 24 The V_{oc}–log(J_{ph}) curve for an all-inorganic $CsPbBr_3$ PSC.

here, eqn (13) is the modified detailed balance model to capture the current density–voltage characteristics of the inorganic perovskite solar cells.

From the detailed balance theory and eqn (2), it is easy to predict the limiting efficiency of inorganic PSCs. Table 4 lists the calculated results for the commonly-used inorganic perovskite materials, with organic–inorganic halide perovskite materials also presented as references. Regarding the worst $CsSnBr_3$ and $CsSnI_3$ systems, they show giant J_{sc} losses and V_{oc} losses due to their low internal quantum efficiency and non-radiative recombination, respectively.[187,192,229] The most promising system is $CsPbI_2Br$, which shows the lowest PCE loss (40.6%) in all the inorganic perovskite systems. Therefore, accelerating the charge extraction at the interface is crucial for high-performance all-inorganic perovskite solar cells.

6.2 Interfacial modification

Inorganic perovskites have advantages in terms of their ambient phase stability compared to organic–inorganic perovskites; however, the serious energy barrier at the interface between the perovskite and HTL and/or ETL limits the charge extraction and therefore drags down the device performance. Thus, interfacial engineering is a prerequisite to eliminate interfacial structural and electronic mismatches, lowing the charge transfer barrier for maximized charge transfer dynamics, including ETL/perovskite and HTL/perovskite interfaces.

In a typical perovskite solar cell, free electrons (photogenerated electrons) are usually injected into the TiO_2 layer and then in to the external circuit under an electric field. Although the transfer rate can be up to 10^9 s^{-1}, substantial charge is still lost when crossing the interface owing to the presence of the energy barrier as well as defects.[230] To better address this issue, enormous efforts have been conducted to boost the charge extraction. Highly conductive materials with a matchable energy structure to the ETL and perovskite (such as graphene QDs, carbon QDs, or C_{60}) have been incorporated in an attempt to accelerate charge transfer.[89,93,120] Upon introducing graphene QDs into the TiO_2/$CsPbBr_3$ interface, the charge-extraction time could be shortened from 116.2 ns to 99.3 ns.[89] Furthermore, by combining the C_{60} with ZnO to form a ZnO@C_{60} bilayer as an electron-transporting layer, the recombination reaction could be suppressed, owing to the higher driving force of 0.34 eV for C60 than 0.04 eV for ZnO layer, as shown in Fig. 25a and b. Consequently, the all-inorganic $CsPbI_2Br$ perovskite solar cell yielded a PCE as high as 13.3% with excellent long-term stability.[120] Besides, TiO_2/SnO_2 and SnO_2/ZnO

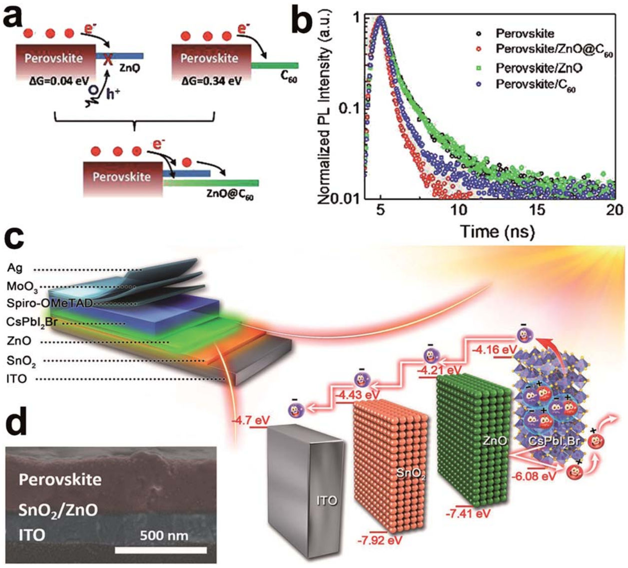

Fig. 25 (a) Charge-transfer mechanism and time-resolved PL decay spectra of Zn@C60/perovskite film.[120] (c) Device architecture of the all-inorganic $CsPbI_2Br$ PVSC and the corresponding energy diagrams. (d) Cross-section SEM image of a $CsPbI_2Br$ perovskite film on SnO_2/ZnO.[117]

Table 4 Efficiency limit of inorganic perovskite solar cells. The losses of the device characteristics (J_{sc}, V_{oc}, FF, and PCE) compared to their Shockley–Queisser limiting values are also listed

Formula	J_{sc} (mA cm^{-2})	V_{oc} (V)	PCE (%)	FF	Bandgap (eV)	Ref.
$CsPbBr_3$	8.12	1.458	9.72%	0.82	2.3	89
Limit	8.99	1.98	16.54%	0.93	2.3	
Loss	9.6%	26.3%	41.2%	11.8%	—	
$CsPb_{0.9}Sn_{0.1}IBr_2$	14.3	1.26	11.33%	0.63	1.79	70
Limit	19.89	1.50	27.33%	0.92	1.79	
Loss	28.1%	16%	58.5%	31.5%	—	
$CsPbI_2Br$	15.0	1.23	14.6%	0.79	1.82	117
Limit	16.45	1.62	24.57%	0.92	1.82	
Loss	8.8%	24.1%	40.6%	22.8%	—	
$CsPbI_3$	~18	~1.08	15.7%	0.81	1.73	139
Limit	21.66	1.45	28.55%	0.91	1.73	
Loss	16.9%	37.2%	45.0%	10.9%	—	
$CsSnBr_3$	9.1	0.42	2.17%	0.57	1.75	187
Limit	21.06	1.46	28.15%	0.92	1.75	
Loss	56.8%	71.2%	92.3%	38.0%	—	
$CsSnI_3$	~9.08	~0.4	3.56%	0.62	1.3	192
Limit	35.81	1.04	33.13%	0.89	1.3	
Loss	71.5%	50%	89.2%	30.3%	—	

bilayered electron-transporting layers have also been developed to provide a buffer area for charge transfer.[117,221] As shown in Fig. 25c and d, ZnO displayed a desirable cascade energy level alignment between the perovskite and SnO_2 ETL, resulting in suppressed interfacial non-radiative recombination and a high PCE of 14.6%. In this work, the effects induced by the different interfacial ETLs were determined by steady-state photoluminescence (PL) measurements and time-resolved PL decay, demonstrating the beneficial effect on modulating the electron-extraction processes.

Another strategy to realize the rapid transfer of electrons to the ETL layer and to reduce recombination is to tune the electronic state or to increase the conduction band minimum (CBM) of the window layer. A simple interfacial engineering process by passivating SnO_2 with $SnCl_2$ could significantly reduce the energy loss for a high V_{oc} device, which may be associated with the interaction between Cl^- and SnO_2 according to previous reports in hybrid perovskite solar cells.[231,232] It should be noted the interfacial engineering is universal in all types of photovoltaics. Therefore, enormous works have employed this strategy in organic–inorganic perovskite solar cells, such as with lead-doped mesoporous TiO_2 and nanofibers,[233] Sb_2S_3,[234] MgO,[235] or Y_2O_3 (ref. 236) as interfacial modification materials, to increase the performance of all-inorganic perovskite solar cells.

The large interfacial energy differences at perovskite/HTL interfaces is another reason to depress the charge-extraction kinetics. One promising solution to this impasse is to narrow the energy differences by tuning the energy band edge of cell layers or by setting intermediate energy levels at interfaces. Quantum dots (QDs) with tunable bandgaps, high absorption coefficients, and small size have attracted great interest as interfacial modifiers in PSCs to increase electron–hole separation.[237] Aiming to realize the successful fabrication of this physical-of-proof concept graded bandgap construction, perovskite films and QDs films should be exhibited using orthogonal solvents, allowing the subsequent coating of upper multilayers. Especially for perovskite QDs, upon perovskite QDs covered onto the surface of perovskite active layer, anion exchange is inevitable at the interface, resulting in a component-graded heterojunction, as shown in Fig. 26. Liu's group integrated bulk-nanosheet-quantum dots to optimize the energy alignment between $CsPbBrI_2$ and the hole-transport layers, achieving a PCE of 12.39%. This was the first designation of a 3D–2D–0D multiple graded interface based on $CsPbBrI_2$ material *via* a solution process.[119] Later on, optical and energy-band manipulation were further employed to enhance the $CsPbI_2Br$ device performance. A stable and high-mobility $CsPbI_3$ QDs film was obtained through Mn^{2+} substitution, SCN capping, and $[(NH_2)_2CH]^+$ treatment, achieving a PCE of 10.97% based on this $CsPbI_3$ QDs film. Subsequently, a halide-ion-profiled heterojunction was designed at the $CsPbBrI_2/CsPbI_3$ QD interface to improve the carrier collection. Arising from the extended light absorbance range and minimal charge recombination loss, as a result, the device achieved a PCE of 14.45%.[123]

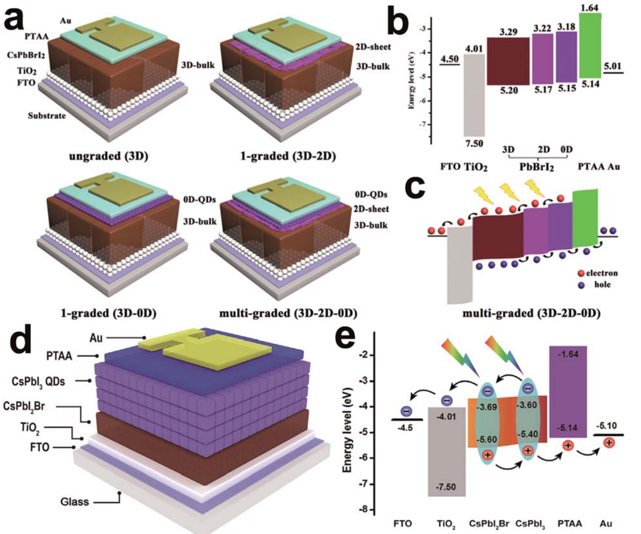

Fig. 26 (a) Schematic structures of inorganic PSC devices without and with a graded interface. (b) Energy-level diagram of multi-graded $CsPbBrI_2$ PSCs. (c) Schematic of the carrier-transport mechanism in multi-graded $CsPbBrI_2$ PSCs. (d) Schematic structure and (e) energy-level diagram of the charge-collection process of photogenerated charge carriers.[119,123]

For $CsPbBr_3$ perovskite solar cells, the hole-extraction barrier is a more serious issue due to their larger bandgap, which achieves a barrier value of 0.6 eV in carbon-electrode-based devices. Therefore, modulating the interfaces of $CsPbBr_3$/carbon provides huge room for efficiency improvement. Tang *et al.* synthesized a series of p-type and bandgap-tunable QDs, such as $CuInS_2/ZnS$,[92] CdZnSe@ZnSe,[238] $CsSnBr_{3-x}I_x$ (ref. 95) and red phosphorus QDs,[93,94] to bridge the large gap at the perovskite/carbon interface, setting an intermediate energy level between the perovskite and back electrode for the sake of hole transportation from the perovskite, as shown in Fig. 27. By optimizing the species and energy levels of QDs, the efficiency of all-inorganic $CsPbBr_3$ perovskite solar cells could be

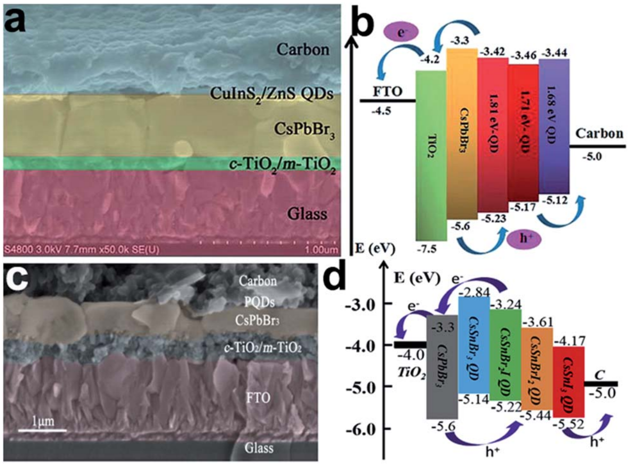

Fig. 27 Cross-sectional SEM images (a, c) and energy diagrams (b, d) of a typical inorganic PSC device with an architecture of glass/c-TiO_2/m-TiO_2/$CsPbBr_3$/carbon by modifying the perovskite/carbon interface with $CuInS_2/ZnS$ and $CsSnX_3$ QDs.[92,95]

enhanced to around 10%, which is much higher than that of the control device. Recently, organic materials, including P3HT,[239] P3HT/zinc phthalocyanine composition,[240] polythiophene, polypyrrole, and polyaniline, as well as organic small molecule BT-BTH[241] were also employed to modify the $CsPbBr_3$/carbon interface to enhance the overall performance of corresponding devices, demonstrating the importance of reducing the energy loss and recombination by interfacial engineering.

Lowering the work function (WF) of a carbon electrode is another path to accelerate charge transfer. Tang's group developed a novel method to tune the WF of a carbon electrode by doping alloyed PtNi nanowires to accelerate hole extraction from $CsPbBr_3$ halides (Fig. 28).[91] The WFs of metallic Pt and Ni are −5.65 eV and −4.6 eV, respectively. After alloying, PtNi nanowires with a WF of −5.5 eV could be obtained. Upon combination with carbon paste, the WF of carbon/PtNi composition electrode could be well-tuned ranging from −5.1 to −5.5 eV through controlling the PtNi dosage (1–7 wt%). The preliminary results demonstrate a maximized PCE of 7.17% (J_{sc} = 6.54 mA cm^{-2}, V_{oc} = 1.431 V, FF = 76.6%) at 3 wt% PtNi nanowires. Although the WF of −5.5 eV was more matchable at 7 wt% PtNi to −5.6 eV (the VB value of $CsPbBr_3$ film), the poor adhesion of carbon/PtNi to the perovskite layer caused serious charge transfer resistance. This research indicated that the matching WF and good adhesion of the carbon back electrode is beneficial to hole extraction and electron–hole separation. Meanwhile, carbon nanotubes were also introduced to adjust the WF of the carbon electrode, whereby the performance of solar cells could also be improved.[242]

As discussed above, inserting an intermediate energy level and lowering the WF of the charge-contact layer are effective ways to improve charge separation and extraction. Aiming to further improve the efficiency, a dual interfacial design for efficient $CsPbI_2Br$ perovskite solar was developed by applying an amino-functionalized polymer (PN4N) as a cathode interlayer and a dopant-free hole-transporting polymer poly[5,5′-bis(2-butyloctyl)-(2,2′-bithiophene)-4,4′-dicarboxylate-*alt*-5,5′-2,2′-bithiophene] (PDCBT) as the anode interlayer.[243] Apart from providing a better energy-level matching, both theoretical and experimental results revealed that the organic materials could couple with perovskite crystals, passivating the surface-region defects and suppressing the photo-induced halide segregation of $CsPbI_2Br$ films. With these positive effects, the optimal device achieved an enhanced efficiency of up to 16.2%, mainly attributed to the reduced trap-assisted nonirradiative recombination and increased charge-extraction ability.

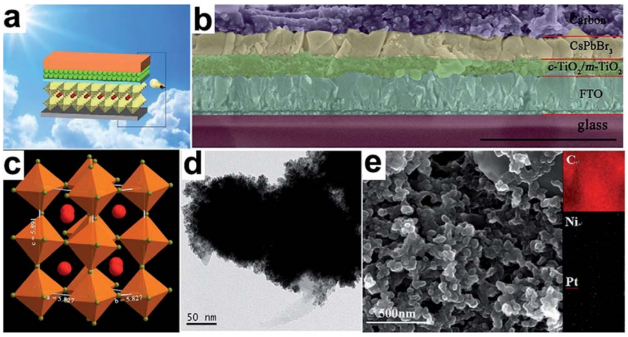

Fig. 28 (a) Schematic illustration and (b) cross-sectional SEM image of the carbon-based inorganic PSC configuration. (c) Crystal structure of perovskite-structured $CsPbBr_3$ halide. (d) TEM image of PtNi NWs. (e) Top-view SEM image of 3 wt% alloy-controlled carbon back-electrode and mapping images of C, Pt, and Ni elements.[91]

Considering "devices are interfaces," fully understanding the interfacial atomic and electronic structures is essential for interface design. After introducing functional materials, the lattice stability and charge transfer are two crucial parameters to evaluate the feasibility of interfacial engineering. Overall, new interface modifiers and heterojunction device designs still need to be developed in the future.

7. Challenges and outlook

The birth of PSCs in 2009 undoubtedly heralded a new frontier for the third-generation photovoltaics. PSCs have experienced a great change from liquid to solid junctions and from spatial three-dimensional to planar two-dimensional structures, and the maximized PCE has increased from an initial 3.8% to now 25.2% within these past ten years. As a promising candidate, inorganic PSCs, due to their much more stable phase, have inevitably attracted more and more attention on the basis of the existing technology. However, several challenges still need to be resolved, such as reducing the costs, improving the efficiency and stability, to push their industrialization. Here, some brief aspects are enumerated in the following:

(1) Research on a deep insight into the photophysics mechanism:

At present, although much research is focused on improving the film synthesis methods or material properties, the physical mechanism of inorganic perovskite solar cells is still lacking. A deeper understanding and in-depth study on the mechanism of interfacial charge recombination and regarding the stability of materials would be useful for finding new structures and for further improving the perovskite solar cell performance.

(2) Broadening the absorption spectrum:

Commercial Si solar cells can absorb light from 300 nm to 1200 nm. However, the inorganic $CsPbI_3$ perovskite film can only absorb light to nearly 700 nm, not to mention the maximized 540 nm for $CsPbBr_3$ perovskite; such a narrow light response causes serious solar energy loss. Therefore, how to broaden the light absorption of inorganic PSCs is an inevitable course to achieve champion PCE outputs. Compared to hybrid perovskites, the inorganic perovskite is a promising material for tandem solar cells owing to their relatively larger bandgap. Therefore, developing tandem solar cells with inorganic PSCs and Si or CIGS solar cells may be a focus in the future.

(3) Enhanced stability:

Inorganic $CsPbBr_3$ perovskite is regarded as having high stability under UV light, water, and/or heat attacks; however, other I-containing inorganic PSCs still suffer from light- and steam-induced phase degradation, even with encapsulation technology. So, manufacturing a long-time working PSC device with a high PCE is still an urgent issue to be implemented.

Doping $CsPbX_3$ with smaller radius ions has recently been highlighted as a promising way to achieve phase stability and reduce the trap density of the perovskite layer. Other strategies, such as solvent controlled film growth, alloying a 2D perovskite component into host perovskite, polymer-induced surface passivation, and interfacial engineering, all pave the way to stabilize $CsPbI_3$.

(4) Environmentally friendly issues:

Lead is a widely-used heavy metal element but is extremely harmful to the human body, especially to children. A lead amount more than 10 μg dl^{-1} in blood can cause irreversible damage to the mental development of children, so avoiding the usage of lead in perovskite solar cells is a significant work. However, to date, highly efficient perovskite solar cells are all based on toxic metal Pb, or on the partial substitution of Pb with other elements. In this regard, developing lead-free perovskite light-absorbing layers is an important direction in the future. Although some researchers have made great efforts with lead-free perovskite solar cells, their photoelectric conversion efficiency is still low compared to Pb-based devices. Thus, further in-depth systematic research on materials and structures and the preparation methods of new lead-free perovskite solar cells is essential.

(5) Research on large-area devices:

Scale-up and large-area processing technology has become a tricky problem that must be resolved before commercialization. Although some researchers have focused on large-area devices, their film uniformity is still poor as is their efficiency. So how to get high-efficiency large-area devices is still a great challenge. Tremendous progress has already been made in enhancing the performance of small-area cells (typically ≤ 0.1 cm^2). However, many of the film-making techniques (such as spin-coating and drop-casting) used in the laboratory do not suit large-scale production. Spin-coating is currently the most common film-making strategy for inorganic perovskite layers but not for large-area processing (≥ 1 cm^2). Besides, much material may be wasted during the process. Spraying and printing methods seem to be promising methods for scale-up. However, clearly, scaling up the size of perovskite solar cells without significant efficiency loss is a remaining challenge to be resolved.

(6) Flexible perovskite solar cells:

With an aim to achieve the building of integrated photovoltaics, there have been many reports on organic–inorganic flexible perovskite solar cells. However, insufficient studies on all-inorganic perovskite solar cells have been undertaken. Recently, Liu's group improved the quality of the perovskite absorber layer by adding dimethyl sulfide, enhancing the efficiency of the flexible perovskite solar cell.[244] Zhao's group demonstrated a facile method to fabricate a high-performance all-inorganic $CsPbI_2Br$ perovskite solar cell through a one-step method under 100–130 °C low-temperature annealing process, which was beneficial for assembly on flexible substrate.[176] Therefore, more research should be done to promote the development of flexible inorganic perovskite solar cells.

8. Conclusions

The tremendous progress made in the development of inorganic perovskite solar cells convinces that inorganic perovskites is a promising alternative to organic–inorganic perovskites, due to their low-cost facile fabrication process and long-time stability. This review systematically summarizes the developments of inorganic halide perovskite solar cells in respect of compositional engineering, film-making methods, and interfacial engineering methods. It also covered predicting their limited efficiency using the modified detailed balance model and discussed the recombination mechanism. Finally, by identifying new challenges, several outlooks are provided for further research and potential development in this area.

Conflicts of interest

There are no conflicts to declare.

Acknowledgements

This work was supported by the National Natural Science Foundation of China (61774139, 21503202, 61604143), the Fundamental Research Funds for the Central Universities (11618409, 21619311), and China Postdoctoral Science Foundation (55350315).

Notes and references

1 D. M. Chapin, C. S. Fuller and G. L. Pearson, *J. Appl. Phys.*, 1954, **25**, 676–677.

2 N. M. Haegel, R. Margolis, T. Buonassisi, D. Feldman, A. Froitzheim, R. Garabedian, M. Green, S. Glunz, H.-M. Henning, B. Holder, I. Kaizuka, B. Kroposki, K. Matsubara, S. Niki, K. Sakurai, R. A. Schindler, W. Tumas, E. R. Weber, G. Wilson, M. Woodhouse and S. Kurtz, *Science*, 2017, **356**, 141–143.

3 Y. Ren, D. Sun, Y. Cao, H. N. Tsao, Y. Yuan, S. M. Zakeeruddin, P. Wang and M. Grätzel, *J. Am. Chem. Soc.*, 2018, **140**, 2405–2408.

4 N. Zhou, K. Prabakaran, B. Lee, S. H. Chang, B. Harutyunyan, P. Guo, M. R. Butler, A. Timalsina, M. J. Bedzyk, M. A. Ratner, S. Vegiraju, S. Yau, C.-G. Wu, R. P. H. Chang, A. Facchetti, M.-C. Chen and T. J. Marks, *J. Am. Chem. Soc.*, 2015, **137**, 4414–4423.

5 M. K. Brennaman, R. J. Dillon, L. Alibabaei, M. K. Gish, C. J. Dares, D. L. Ashford, R. L. House, G. J. Meyer, J. M. Papanikolas and T. J. Meyer, *J. Am. Chem. Soc.*, 2016, **138**, 13085–13102.

6 Y. Saygili, M. Söderberg, N. Pellet, F. Cao, Y. Cao, A. B. Muñoz-García, S. M. Zakeeruddin, N. Vlachopoulos, M. Pavone, G. Boschloo, L. Kavan, J. Moser, M. Grätzel, A. Hagfeldt and M. Freitag, *J. Am. Chem. Soc.*, 2016, **138**, 15087–15096.

7 A. Kunzmann, S. Valero, Á. E. Sepúlveda, M. Rico-Santacruz, E. L. Jesús, R. Berenguer, J. García-Martínez, D. M. Guldi,

E. Serrano and R. D. Costa, *Adv. Energy Mater.*, 2018, **12**, 1702583.

8 Z. Zhao, C. Lin, J. Tang and Z. Xia, *Nano Energy*, 2018, **49**, 193–199.

9 T. J. Barr and G. J. Meyer, *ACS Energy Lett.*, 2017, **2**, 2335–2340.

10 L. Song, W. Wang, S. Pröller, D. M. González, J. Schlipf, C. J. Schaffer, K. Peters, E. M. Herzig, S. Bernstorff, T. Bein, D. Fattakhova-Rohlfing and P. Müller-Buschbaum, *ACS Energy Lett.*, 2017, **2**, 991–997.

11 P. Maisch, K. C. Tam, P. Schilinsky, H. Egelhaaf and C. J. Brabec, *Sol. RRL*, 2018, **2**, 1800005.

12 B. Yang, M. A. Kolaczkowski, M. A. Brady, J. K. Keum, J. F. Browning, T. L. Chen and Y. Liu, *Sol. RRL*, 2018, **2**, 1700208.

13 Y. L. Lin, M. A. Fusella and B. P. Rand, *Adv. Energy Mater.*, 2018, **8**, 1702816.

14 C. Xie, A. Classen, A. Späth, X. Tang, J. Min, M. Meyer, C. Zhang, N. Li, A. Osvet, R. H. Fink and C. J. Brabec, *Adv. Energy Mater.*, 2018, **8**, 1702857.

15 I. Ramirez, M. Causa, Y. Zhong, N. Banerji and M. Riede, *Adv. Energy Mater.*, 2018, **8**, 1703551.

16 G. O. N. Ndjawa, K. R. Graham, S. Mollinger, D. M. Wu, D. Hanifi, R. Prasanna, B. D. Rose, S. Dey, L. Yu, J. Brédas, M. D. McGehee, A. Salleo and A. Amassian, *Adv. Energy Mater.*, 2017, **7**, 1601995.

17 N. Li, I. McCulloch and C. J. Brabec, *Energy Environ. Sci.*, 2018, **11**, 1355–1361.

18 S. Chang, P. Cheng, G. Li and Y. Yang, *Joule*, 2018, **2**, 1–16.

19 H. B. Naveed and W. Ma, *Joule*, 2018, **2**, 621–641.

20 S. M. Menke, N. A. Ran, G. C. Bazan and R. H. Friend, *Joule*, 2016, **2**, 25–35.

21 L. E. Garner, A. Bera, B. W. Larson, D. P. Ostrowski, A. J. Pal and W. A. Braunecker, *ACS Energy Lett.*, 2017, **2**, 1556–1563.

22 V. V. Duzhko, B. Dunham, S. J. Rosa, M. D. Cole, A. Paul, Z. A. Page, C. Dimitrakopoulos and T. Emrick, *ACS Energy Lett.*, 2017, **2**, 957–963.

23 J. Jean, T. S. Mahony, D. Bozyigit, M. Sponseller, J. Holovský, M. G. Bawendi and V. Bulović, *ACS Energy Lett.*, 2017, **2**, 2616–2624.

24 L. Tan, P. Li, B. Sun, M. Chaker and D. Ma, *ACS Energy Lett.*, 2017, **2**, 1573–1585.

25 S. Pradhan, A. Stavrinadis, S. Gupta, S. Christodoulou and G. Konstantatos, *ACS Energy Lett.*, 2017, **2**, 1444–1449.

26 F. Wang, H. Wang, X. Liu, D. Wu, K. Jiang, Q. Li and D. Xu, *Adv. Energy Mater.*, 2018, **8**, 1800136.

27 S. Chen, Y. Wang, Q. Liu, G. Shi, Z. Liu, K. Lu, L. Han, X. Ling, H. Zhang, S. Cheng and W. Ma, *Adv. Energy Mater.*, 2017, **8**, 1701194.

28 S. Baek, S. Lee, J. H. Song, C. Kim, Y. Ha, H. Shin, H. Kim, S. Jeong and J. Lee, *Energy Environ. Sci.*, 2018, **11**, 2078–2084.

29 Y. Wang, Q. Zhang, F. Huang, Z. Li, Y. Zheng, X. Tao and G. Cao, *Nano Energy*, 2018, **44**, 135–143.

30 J. M. Kim, S. Kim, D. H. Shin, S. W. Seo, H. S. Lee, J. H. Kim, C. W. Jang, S. S. Kang, S. Choi, G. Y. Kwak, K. J. Kim, H. Lee and H. Lee, *Nano Energy*, 2018, **43**, 124–129.

31 J.-H. Im, C.-R. Lee, J.-W. Lee, S.-W. Park and N.-G. Park, *Nanoscale*, 2011, **3**, 4088–4093.

32 W. Zhang, G. E. Eperon and H. J. Snaith, *Nat. Energy*, 2016, **1**, 16048.

33 M. A. Green and A. Ho-Baillie, *ACS Energy Lett.*, 2017, **2**, 822–830.

34 N. J. Jeon, H. Na, E. H. Jung, T.-Y. Yang, Y. G. Lee, G. Kim, H.-W. Shin, S. I. Seok, J. Lee and J. Seo, *Nat. Energy*, 2018, **3**, 682–689.

35 R. Mastria, S. Colella, A. Qualtieri, A. Listorti, G. Giglia and A. Rizzo, *Nanoscale*, 2017, **9**, 3889–3897.

36 A. Ummadisingu, L. Steier, J. Y. Seo, T. Matsui, A. Abate, W. Tress and M. Grätzel, *Nature*, 2017, **545**, 208–212.

37 N. Ahn, D.-Y. Son, I.-H. Jang, S. M. Kang, M. Choi and N.-G. Park, *J. Am. Chem. Soc.*, 2015, **137**, 8696–8699.

38 A. Kojima, K. Teshima, Y. Shirai and T. Miyasaka, *J. Am. Chem. Soc.*, 2009, **131**, 6050–6051.

39 W. S. Yang, B. W. Park, E. H. Jung, N. J. Jeon, Y. C. Kim, D. U. Lee, S. S. Shin, J. Seo, E. K. Kim, J. H. Noh and S. I. Seok, *Science*, 2017, **356**, 1376–1379.

40 E. H. Jung, N. J. Jeon, E. Y. Park, C. S. Moon, T. J. Shin, T.-Y. Yang, J. H. Noh and J. Seo, *Nature*, 2019, **567**, 511–515.

41 Q. Jiang, Y. Zhao, X. Zhang, X. Yang, Y. Chen, Z. Chu, Q. Ye, X. Li, Z. Yin and J. You, *Nat. Photonics*, 2019, **13**, 460–466.

42 M. Kim, G.-H. Kim, T. K. Lee, I. W. Choi, H. W. Choi, Y. Jo, Y. J. Yoon, J. W. Kim, J. Lee, D. Huh, H. Lee, S. K. Kwak, J. Y. Kim and D. S. Kim, *Joule*, 2019, DOI: 10.1016/j.joule.2019.06.014.

43 J. Burschka, N. Pellet, S. J. Moon, R. Humphry-Baker, P. Gao, M. K. Nazeeruddin and M. Gratzel, *Nature*, 2013, **499**, 316–319.

44 H. Zhou, Q. Chen, G. Li, S. Luo, T.-b. Song, H.-S. Duan, Z. Hong, J. You and Y. Yang, *Science*, 2014, **345**, 542–546.

45 N. J. Jeon, J. H. Noh, W. S. Yang, Y. C. Kim, S. Ryu, J. Seo and S. I. Seok, *Nature*, 2015, **517**, 476–480.

46 W. S. Yang, J. H. Noh, N. J. Jeon, Y. C. Kim, S. Ryu, J. Seo and S. I. Seok, *Science*, 2015, **348**, 1234–1237.

47 https://www.nrel.gov/pv/assets/pdfs/best-research-cell-efficiencies.20190802.pdf.

48 B. Cai, Y. Xing, Z. Yang, W.-H. Zhang and J. Qiu, *Energy Environ. Sci.*, 2013, **6**, 1480–1485.

49 S. Pang, H. Hu, J. Zhang, S. Lv, Y. Yu, F. Wei, T. Qin, H. Xu, Z. Liu and G. Cui, *Chem. Mater.*, 2014, **26**, 1485–1491.

50 J. Tong, Z. Song, D. H. Kim, X. Chen, C. Chen, A. F. Palmstrom, P. F. Ndione, M. O. Reese, S. P. Dunfield, O. G. Reid, J. Liu, F. Zhang, S. P. Harvey, Z. Li, S. T. Christensen, G. Teeter, D. Zhao, M. M. Al-Jassim, M. F. A. M. van Hest, M. C. Beard, S. E. Shaheen, J. J. Berry, Y. Yan and K. Zhu, *Science*, 2019, **364**, 475–479.

51 A. A. Zhumekenov, M. I. Saidaminov, M. A. Haque, E. Alarousu, S. P. Sarmah, B. Murali, I. Dursun, X.-H. Miao, A. L. Abdelhady, T. Wu, O. F. Mohammed and O. M. Bakr, *ACS Energy Lett.*, 2016, **1**, 32–37.

52 Z. Wang, Z. Shi, T. Li, Y. Chen and W. Huang, *Angew. Chem., Int. Ed.*, 2017, **56**, 1190–1212.

53 Q. A. Akkerman, G. Rainò, M. V. Kovalenko and L. Manna, *Nat. Mater.*, 2018, **17**, 394–405.

54 S. Ahmad, P. K. Kanaujia, W. Niu, J. J. Baumberg and G. V. Prakash, *ACS Appl. Mater. Interfaces*, 2014, **6**, 10238–10247.
55 T. Leijtens, G. E. Eperon, S. Pathak, A. Abate, M. M. Lee and H. J. Snaith, *Nat. Commun.*, 2013, **4**, 2885.
56 B. Conings, J. Drijkoningen, N. Gauquelin, A. Babayigit, J. Haen, L. D'Olieslaeger, A. Ethirajan, J. Verbeeck, J. Manca, E. Mosconi, F. D. Angelis and H.-G. Boyen, *Adv. Energy Mater.*, 2015, **5**, 1500477.
57 E. J. Juarez-Perez, Z. Hawash, S. R. Raga, L. K. Ono and Y. Qi, *Energy Environ. Sci.*, 2016, **9**, 3406–3410.
58 A. Ho-Baillie, M. Zhang, C. F. J. Lau, F.-J. Ma and S. Huang, *Joule*, 2019, **3**, 938–955.
59 H. Chen, S. Xiang, W. Li, H. Liu, L. Zhu and S. Yang, *Sol. RRL*, 2018, **2**, 1700188.
60 C. C. Stoumpos, C. D. Malliakas and M. G. Kanatzidis, *Inorg. Chem.*, 2013, **52**, 9019–9038.
61 C. C. Stoumpos, C. D. Malliakas, J. Peters, Z. Liu, M. Sebastian, J. Im, T. C. Chasapis, A. C. Wibowo, D. Y. Chung and A. J. Freeman, *Cryst. Growth Des.*, 2013, **13**, 2722–2727.
62 H. L. Wells, *Z. Anorg. Chem.*, 1893, **3**, 195.
63 B. Tang, H. Dong, L. Sun, W. Zheng, Q. Wang, F. Sun, X. Jiang, A. Pan and L. Zhang, *ACS Nano*, 2017, **11**, 10681–10688.
64 X. Tang, Z. Hu, W. Chen, X. Xing, Z. Zang, W. Hu, J. Qiu, J. Du, Y. Leng, X. Jiang and L. Mai, *Nano Energy*, 2016, **28**, 462–468.
65 H. Zhou, S. Yuan, X. Wang, T. Xu, X. Wang, H. Li, W. Zheng, P. Fan, Y. Li, L. Sun and A. Pan, *ACS Nano*, 2017, **11**, 1189–1195.
66 D. Pan, Y. Fu, J. Chen, K. J. Czech, J. C. Wright and S. Jin, *Nano Lett.*, 2018, **18**, 1807–1813.
67 T. Yang, Y. Zheng, Z. Du, W. Liu, Z. Yang, F. Gao, L. Wang, K.-C. Chou, X. Hou and W. Yang, *ACS Nano*, 2018, **12**, 1611–1617.
68 W. J. Yin, Y. F. Yan and S. H. Wei, *J. Phys. Chem. Lett.*, 2014, **5**, 3625–3631.
69 P. Cottingham and R. L. Brutchey, *Chem. Mater.*, 2016, **28**, 7574–7577.
70 J. Liang, P. Zhao, C. Wang, Y. Wang, Y. Hu, G. Zhu, L. Ma, J. Liu and Z. Jin, *J. Am. Chem. Soc.*, 2017, **139**, 14009–14012.
71 J.-P. Correa-Baena, A. Abate, M. Saliba, W. Tress, T. Jesper Jacobsson, M. Grätzel and A. Hagfeldt, *Energy Environ. Sci.*, 2017, **10**, 710–727.
72 Z. Cheng and J. Lin, *CrystEngComm*, 2010, **12**, 2646–2662.
73 W. A. Dunlap-Shohl, Y. Zhou, N. P. Padture and D. B. Mitzi, *Chem. Rev.*, 2019, **119**, 3193–3295.
74 W. Travis, E. N. K. Glover, H. Bronstein, D. O. Scanlon and R. G. Palgrave, *Chem. Sci.*, 2016, **7**, 4548–4556.
75 B. Saparov and D. B. Mitzi, *Chem. Rev.*, 2016, **116**, 4558–4596.
76 C. Li, X. Lu, W. Ding, L. Feng, Y. Gao and Z. Guo, *Acta Crystallogr., Sect. B: Struct. Sci.*, 2008, **64**, 702–707.
77 Y. Zhou and Y. Zhao, *Energy Environ. Sci.*, 2019, **12**, 1495–1511.
78 N. Aristidou, C. Eames, I. Sanchez-Molina, X. Bu, J. Kosco, M. S. Islam and S. A. Haque, *Nat. Commun.*, 2017, **8**, 15218.
79 N. Arora, M. I. Dar, A. Hinderhofer, N. Pellet, F. Schreiber, S. M. Zakeeruddin and M. Grätzel, *Science*, 2017, **358**, 768–771.
80 E. H. Anaraki, A. Kermanpur, M. T. Mayer, L. Steier, T. Ahmed, S.-H. Turren-Cruz, J. Seo, J. Luo, S. M. Zakeeruddin, W. R. Tress, T. Edvinsson, M. Grätzel, A. Hagfeldt and J.-P. Correa-Baena, *ACS Energy Lett.*, 2018, **34**, 773–778.
81 B. O'Regan and M. Gratzel, *Nature*, 1991, **353**, 737–739.
82 W. Zhang, M. Saliba, S. D. Stranks, Y. Sun, X. Shi, U. Wiesner and H. J. Snaith, *Nano Lett.*, 2013, **13**, 4505–4510.
83 J. J. Choi, X. Yang, Z. M. Norman, S. J. L. Billinge and J. S. Owen, *Nano Lett.*, 2014, **14**, 127–133.
84 M. Kulbak, D. Cahen and G. Hodes, *J. Phys. Chem. Lett.*, 2015, **6**, 2452–2456.
85 G. E. Eperon, G. M. Paterno, R. J. Sutton, A. Zampetti, A. A. Haghighirad, F. Cacialli and H. J. Snaith, *J. Mater. Chem. A*, 2015, **3**, 19688–19695.
86 X. Chang, W. Li, L. Zhu, H. Liu, H. Geng, S. Xiang, J. Liu and H. Chen, *ACS Appl. Mater. Interfaces*, 2016, **8**, 33649–33655.
87 P. Luo, Y. Zhou, S. Zhou, Y. Lu, C. Xu, W. Xia and L. Sun, *Chem. Eng. J.*, 2018, **343**, 146–154.
88 J. Liang, C. Wang, Y. Wang, Z. Xu, Z. Lu, Y. Ma, H. Zhu, Y. Hu, C. Xiao, X. Yi, G. Zhu, H. Lv, L. Ma, T. Chen, Z. Tie, Z. Jin and J. Liu, *J. Am. Chem. Soc.*, 2016, **138**, 15829–15832.
89 J. Duan, Y. Zhao, B. He and Q. Tang, *Angew. Chem., Int. Ed.*, 2018, **57**, 3787–3791.
90 Y. Li, J. Duan, H. Yuan, Y. Zhao, B. He and Q. Tang, *Sol. RRL*, 2018, **2**, 1800164.
91 J. Ding, Y. Zhao, J. Duan, B. He and Q. Tang, *ChemSusChem*, 2018, **11**, 1432–1437.
92 J. Ding, J. Duan, C. Guo and Q. Tang, *J. Mater. Chem. A*, 2018, **6**, 21999–22004.
93 H. Yuan, Y. Zhao, J. Duan, B. He, Z. Jiao and Q. Tang, *Electrochim. Acta*, 2018, **279**, 84–90.
94 G. Liao, J. Duan, Y. Zhao and Q. Tang, *Sol. Energy*, 2018, **171**, 279–285.
95 H. Xu, J. Duan, Y. Zhao, Z. Jiao, B. He and Q. Tang, *J. Power Sources*, 2018, **399**, 76–82.
96 H. Li, G. Tong, T. Chen, H. Zhu, G. Li, Y. Chang, L. Wang and Y. Jiang, *J. Mater. Chem. A*, 2018, **6**, 14255–14261.
97 J. Duan, Y. Zhao, X. Yang, Y. Wang, B. He and Q. Tang, *Adv. Energy Mater.*, 2018, **8**, 1802346.
98 J. Duan, D. Dou, Y. Zhao, Y. Wang, X. Yang, H. Yuan, B. He and Q. Tang, *Mater. Today Energy*, 2018, **10**, 146–152.
99 Y. Zhao, J. Duan, H. Yuan, Y. Wang, X. Yang, B. He and Q. Tang, *Sol. RRL*, 2019, **3**, 1800284.
100 H. Yuan, Y. Zhao, J. Duan, Y. Wang, X. Yang and Q. Tang, *J. Mater. Chem. A*, 2018, **6**, 24324–24329.
101 G. Tong, T. Chen, H. Li, W. Song, Y. Chang, J. Liu, L. Yu, J. Xu, Y. Qi and Y. Jiang, *Sol. RRL*, 2019, **3**, 1900030.
102 X. Li, Y. Tan, H. Lai, S. Li, Y. Chen, S. Li, P. Xu and J. Yang, *ACS Appl. Mater. Interfaces*, 2019, **11**, 29746–29752.

103 G. Tong, T. Chen, H. Li, L. Qiu, Z. Liu, Y. Dang, W. Song, L. K. Ono, Y. Jiang and Y. Qi, *Nano Energy*, 2019, **65**, 104015.

104 Q. S. Ma, S. J. Huang, X. M. Wen, M. A. Green and A. W. Y. Ho-Baillie, *Adv. Energy Mater.*, 2016, **6**, 1502202.

105 C. F. J. Lau, X. Deng, Q. Ma, J. Zheng, J. S. Yun, M. A. Green, S. Huang and A. W. Y. Ho-Baillie, *ACS Energy Lett.*, 2016, **1**, 573–577.

106 C. Liu, W. Li, J. Chen, J. Fan, Y. Mai and R. E. I. Schropp, *Nano Energy*, 2017, **41**, 75–83.

107 Y. Guo, X. Yin, J. Liu and W. Que, *J. Mater. Chem. A*, 2019, **7**, 19008–19016.

108 W. Zhu, Z. Zhang, W. Chai, Q. Zhang, D. Chen, Z. Lin, J. Chang, J. Zhang, C. Zhang and Y. Hao, *ChemSusChem*, 2019, **12**, 2318–2325.

109 N. Li, Z. Zhu, J. Li, A. K.-Y. Jen and L. Wang, *Adv. Energy Mater.*, 2018, **8**, 1800525.

110 Z. Wang, X. Liu, Y. Lin, Y. Liao, Q. Wei, H. Chen, J. Qiu, Y. Chen and Y. Zheng, *J. Mater. Chem. A*, 2019, **7**, 2773–2779.

111 Y. Jiang, J. Yuan, Y. Ni, J. Yang, Y. Wang, T. Jiu, M. Yuan and J. Chen, *Joule*, 2018, **2**, 1–13.

112 W. Zhou, Y. Zhao, X. Zhou, R. Fu, Q. Li, Y. Zhao, K. Liu, D. Yu and Q. Zhao, *J. Phys. Chem. Lett.*, 2017, **8**, 4122–4143.

113 C. Lau, M. Zhang, X. Deng, J. Zheng, J. Bing, Q. Ma, J. Kim, L. Hu, M. A. Green, S. Huang and A. Ho-Baillie, *ACS Energy Lett.*, 2017, **2**, 2319–2325.

114 J. K. Nam, S. U. Chai, W. Cha, Y. J. Choi, W. Kim, M. S. Jung, J. Kwon, D. Kim and J. H. Park, *Nano Lett.*, 2017, **17**, 2028–2033.

115 C. Chen, H. Lin, K. Chiang, W. Tsai, Y. Huang, C. Tsao and H. Lin, *Adv. Mater.*, 2017, **29**, 1605290.

116 D. Bai, J. Zhang, Z. Jin, H. Bian, K. Wang, H. Wang, L. Liang, Q. Wang and S. Frank Liu, *ACS Energy Lett.*, 2018, **3**, 970–978.

117 L. Yan, Q. Xue, M. Liu, Z. Zhu, J. Tian, Z. Li, Z. Chen, Z. Chen, H. Yan, H. Yip and Y. Cao, *Adv. Mater.*, 2018, **30**, 1802509.

118 J. S. Niezgoda, B. J. Foley, A. Z. Chen and J. J. Choi, *ACS Energy Lett.*, 2017, **2**, 1043–1049.

119 J. Zhang, D. Bai, Z. Jin, H. Bian, K. Wang, J. Sun, Q. Wang and S. Liu, *Adv. Energy Mater.*, 2018, **8**, 1703246.

120 C. Liu, W. Li, C. Zhang, Y. Ma, J. Fan and Y. Mai, *J. Am. Chem. Soc.*, 2018, **140**, 3825–3828.

121 S. Mariotti, O. S. Hutter, L. J. Phillips, P. J. Yates, B. Kundu and K. Durose, *ACS Appl. Mater. Interfaces*, 2018, **10**, 3750–3760.

122 Q. Zeng, X. Zhang, X. Feng, S. Lu, Z. Chen, X. Yong, S. A. T. Redfern, H. Wei, H. Wang, H. Shen, W. Zhang, W. Zheng, H. Zhang, J. S. Tse and B. Yang, *Adv. Mater.*, 2018, **30**, 1705393.

123 H. Bian, D. Bai, Z. Jin, J. Zhang, Q. Wang and S. Liu, *Joule*, 2018, **2**, 1500–1510.

124 W. Chen, H. Chen, G. Xu, R. Xue, S. Wang, Y. Li and Y. Li, *Joule*, 2019, **3**, 191–204.

125 S. S. Mali, J. V. Patil and C. K. Hong, *Nano Lett.*, 2019, DOI: 10.1021/acs.nanolett.9b02277.

126 H. Sun, J. Zhang, X. Gan, L. Yu, H. Yuan, M. Shang, C. Lu, D. Hou, Z. Hu, Y. Zhu and L. Han, *Adv. Energy Mater.*, 2019, **9**, 1900896.

127 Y. Zhang, C. Wu, D. Wang, Z. Zhang, X. Qi, N. Zhu, G. Liu, X. Li, H. Hu, Z. Chen, L. Xiao and B. Qu, *Sol. RRL*, 2019, DOI: 10.1002/solr.201900254.

128 A. Swarnkar, A. R. Marshall, E. M. Sanehira, B. D. Chernomordik, D. T. Moore, J. A. Christians, T. Chakrabarti and J. M. Luther, *Science*, 2016, **354**, 92–95.

129 Y. Hu, F. Bai, X. Liu, Q. Ji, X. Miao, T. Qiu and S. Zhang, *ACS Energy Lett.*, 2017, **2**, 2219–2227.

130 L. A. Frolova, D. V. Anokhin, A. A. Piryazev, S. Y. Luchkin, N. N. Dremova, K. J. Stevenson and P. A. Troshin, *J. Phys. Chem. Lett.*, 2017, **8**, 67–72.

131 T. S. Ripolles, K. Nishinaka, Y. Ogomi, Y. Miyata and S. Hayase, *Sol. Energy Mater. Sol. Cells*, 2016, **144**, 532–536.

132 T. Zhang, M. I. Dar, G. Li, F. Xu, N. Guo, M. Grätzel and Y. Zhao, *Sci. Adv.*, 2017, **3**, e1700841.

133 P. Luo, W. Xia, S. Zhou, L. Sun, J. Cheng, C. Xu and Y. Lu, *J. Phys. Chem. Lett.*, 2016, **7**, 3603–3608.

134 Q. Wang, X. Zheng, Y. Deng, J. Zhao, Z. Chen and J. Huang, *Joule*, 2017, **1**, 371–382.

135 F. Li, Y. Pei, F. Xiao, T. Zeng, Z. Yang, J. Xu, J. Sun, B. Peng and M. Liu, *Nanoscale*, 2018, **10**, 6318–6322.

136 J. Liao, H. Rao, B. Chen, D. Kuang and C. Su, *J. Mater. Chem. A*, 2017, **5**, 2066–2072.

137 Y. Wang, T. Zhang, M. Kan, Y. Li, T. Wang and Y. Zhao, *Joule*, 2018, **2**, 2065–2075.

138 B. Li, Y. Zhang, L. Fu, T. Yu, S. Zhou, L. Zhang and L. Yin, *Nat. Commun.*, 2018, **9**, 1076–1084.

139 P. Wang, X. Zhang, Y. Zhou, Q. Jiang, Q. Ye, Z. Chu, X. Li, X. Yang, Z. Yin and J. You, *Nat. Commun.*, 2018, **9**, 2225–2232.

140 Y. Wang, T. Zhang, M. Kan and Y. Zhao, *J. Am. Chem. Soc.*, 2018, **140**, 12345–12348.

141 K. Chen, Q. Zhong, W. Chen, B. Sang, Y. Wang, T. Yang, Y. Liu, Y. Zhang and H. Zhang, *Adv. Funct. Mater.*, 2019, **29**, 1900991.

142 X. Ling, S. Zhou, J. Yuan, J. Shi, Y. Qian, B. W. Larson, Q. Zhao, C. Qin, F. Li, G. Shi, C. Stewart, J. Hu, X. Zhang, J. M. Luther, S. Duhm and W. Ma, *Adv. Energy Mater.*, 2019, **9**, 1900721.

143 H. Zhao, J. Xu, S. Zhou, Z. Li, B. Zhang, X. Xia, X. Liu, S. Dai and J. Yao, *Adv. Funct. Mater.*, 2019, **29**, 1808986.

144 Y. Wang, M. I. Dar, L. K. Ono, T. Zhang, M. Kan, Y. Li, L. Zhang, X. Wang, Y. Yang, X. Gao, Y. Qi, M. Grätzel and Y. Zhao, *Science*, 2019, **365**, 591–595.

145 J. Zhang, G. Hodes, Z. Jin and S. Liu, *Angew. Chem., Int. Ed.*, 2019, DOI: 10.1002/anie.201901081.

146 Q. Chen, H. Zhou, Z. Hong, S. Luo, H.-S. Duan, H.-H. Wang, Y. Liu, G. Li and Y. Yang, *J. Am. Chem. Soc.*, 2014, **136**, 622–625.

147 L. Etgar, P. Gao, Z. Xue, Q. Peng, A. K. Chandiran, B. Liu, M. K. Nazeeruddin and M. Grätzel, *J. Am. Chem. Soc.*, 2012, **134**, 17396–17399.

148 D. Liu and T. L. Kelly, *Nat. Photonics*, 2013, **8**, 133–138.

149 Y. Tong, E. Bladt, M. F. Ayggler, A. Manzi, K. Z. Milowska, V. A. Hintermayr, P. Docampo, S. Bals, A. S. Urban, L. Polavarapu and J. Feldmann, *Angew. Chem., Int. Ed.*, 2016, **55**, 13887–13892.

150 L. Protesescu, S. Yakunin, M. I. Bodnarchuk, F. Krieg, R. Caputo, C. H. Hendon, R. X. Yang, A. Walsh and M. V. Kovalenko, *Nano Lett.*, 2015, **15**, 3692–3696.

151 L. Huang, Q. Gao, L.-D. Sun, H. Dong, S. Shi, T. Cai, Q. Liao and C.-H. Yan, *Adv. Mater.*, 2018, **30**, 1800596.

152 G. R. Yettapu, D. Talukdar, S. Sarkar, A. Swarnkar, A. Nag, P. Ghosh and P. Mandal, *Nano Lett.*, 2016, **16**(8), 4838–4848.

153 T. Shi, W.-J. Yin, F. Hong, K. Zhu and Y. Yan, *Appl. Phys. Lett.*, 2015, **106**, 103902.

154 J. Kang and L.-W. Wang, *J. Phys. Chem. Lett.*, 2017, **8**, 489–493.

155 F. Palazon, S. Dogan, S. Marras, F. Locardi, I. Nelli, P. Rastogi, M. Ferretti, M. Prato, R. Krahne and L. Manna, *J. Phys. Chem. C*, 2017, **121**, 11956–11961.

156 J.-H. Cha, J. H. Han, W. Yin, C. Park, Y. Park, T. K. Ahn, J. H. Cho and D.-Y. Jung, *J. Phys. Chem. Lett.*, 2017, **8**, 565–570.

157 X. Zhang, Z. Jin, J. Zhang, D. Bai, H. Bian, K. Wang, J. Sun, Q. Wang and S. F. Liu, *ACS Appl. Mater. Interfaces*, 2018, **10**, 7145–7154.

158 M. Aamir, T. Adhikari, M. Sher, N. Revaprasadu, W. Khalid, J. Akhtar and J.-M. Nunzi, *New J. Chem.*, 2018, **42**, 14104–14110.

159 Q. Ma, S. Huang, S. Chen, M. Zhang, C. F. J. Lau, M. N. Lockrey, H. K. Mulmudi, Y. Shan, J. Yao, J. Zheng, X. Deng, K. Catchpole, M. A. Green and A. W. Y. Ho-Baillie, *J. Phys. Chem. C*, 2017, **121**, 19642–19649.

160 Q. Zhang, W. Zhu, D. Chen, Z. Zhang, Z. Lin, J. Chang, J. Zhang, C. Zhang and Y. Hao, *ACS Appl. Mater. Interfaces*, 2019, **11**, 2997–3005.

161 R. J. Sutton, G. E. Eperon, L. Miranda, E. S. Parrott, B. A. Kamino, J. B. Patel, M. T. Hörantner, M. B. Johnston, A. A. Haghighirad, D. T. Moore and H. J. Snaith, *Adv. Energy Mater.*, 2016, **6**, 1502458.

162 J. Liang, C. Wang, P. Zhao, Z. Lu, Y. Ma, Z. Xu, Y. Wang, H. Zhu, Y. Hu, G. Zhu, L. Ma, T. Chen, Z. Tie, J. Liu and Z. Jin, *Nanoscale*, 2017, **9**, 11841–11846.

163 Z. Zeng, J. Zhang, X. Gan, H. Sun, M. Shang, D. Hou, C. Lu, R. Chen, Y. Zhu and L. Han, *Adv. Energy Mater.*, 2018, **8**, 1801050.

164 W. Li, M. U. Rothmann, A. Liu, Z. Wang, Y. Zhang, A. R. Pascoe, J. Lu, L. Jiang, Y. Chen, F. Huang, Y. Peng, Q. Bao, J. Etheridge, U. Bach and Y.-B. Cheng, *Adv. Energy Mater.*, 2017, **7**, 1700946.

165 W. Zhu, Q. Zhang, D. Chen, Z. Zhang, Z. Lin, J. Chang, J. Zhang, C. Zhang and Y. Hao, *Adv. Energy Mater.*, 2018, **8**, 1802080.

166 W. Zhua, W. Chai, Z. Zhang, D. Chen, J. Chang, S. Liu, J. Zhang, C. Zhang and Y. Hao, *Org. Electron.*, 2019, **74**, 103–109.

167 W. Zhu, Z. Zhang, W. Chai, D. Chen, H. Xi, J. Chang, J. Zhang, C. Zhang and Y. Hao, *ACS Appl. Energy Mater.*, 2019, **2**, 5254–5262.

168 C. D. Bailie, M. G. Christoforo, J. P. Mailoa, A. R. Bowring, E. L. Unger, W. H. Nguyen, J. Burschka, N. Pellet, J. Z. Lee and M. Grätzel, *Energy Environ. Sci.*, 2015, **8**, 956–963.

169 T. Todorov, T. Gershon, O. Gunawan, C. Sturdevant and S. Guha, *Appl. Phys. Lett.*, 2014, **105**, 1441–1680.

170 P. Löper, S. J. Moon, S. M. de Nicolas, B. Niesen, M. Ledinsky, S. Nicolay, J. Bailat, J. H. Yum, S. D. Wolf and C. Ballif, *Phys. Chem. Chem. Phys.*, 2015, **17**, 1619–1629.

171 R. E. Beal, D. J. Slotcavage, T. Leijtens, A. R. Bowring, R. A. Belisle, W. H. Nguyen, G. F. Burkhard, E. T. Hoke and M. D. McGehee, *J. Phys. Chem. Lett.*, 2016, **7**, 746–751.

172 I. Yokota, *J. Phys. Soc. Jpn.*, 1953, **8**, 595–602.

173 R. Gottesman, L. Gouda, B. S. Kalanoor, E. Haltzi, S. Tirosh, E. Rosh-Hodesh, Y. Tischler, A. Zaban, C. Quarti, E. Mosconi and F. D. Angelis, *J. Phys. Chem. Lett.*, 2015, **6**, 2332–2338.

174 H. Zhu, K. Miyata, Y. Fu, J. Wang, P. P. Joshi, D. Niesner, K. W. Williams, S. Jin and X.-Y. Zhu, *Science*, 2016, **353**, 1409–1413.

175 J. K. Nam, M. S. Jung, S. U. Chai, Y. J. Choi, D. Kim and J. H. Park, *J. Phys. Chem. Lett.*, 2017, **8**, 2936–2940.

176 Y. Wang, T. Zhang, F. Xu, Y. Li and Y. Zhao, *Sol. RRL*, 2018, **2**, 1700180.

177 H. Rao, S. Ye, F. Gu, Z. Zhao, Z. Liu, Z. Bian and C. Huang, *Adv. Energy Mater.*, 2018, **8**, 1800758.

178 A. Marronnier, G. Roma, S. Boyer-Richard, L. Pedesseau, J. M. Jancu, Y. Bonnassieux, C. Katan, C. C. Stoumpos, M. G. Kanatzidis and J. Even, *ACS Nano*, 2018, **12**, 3477–3486.

179 E. M. Sanehira, A. R. Marshall, J. A. Christians, S. P. Harvey, P. N. Ciesielski, L. M. Wheeler, P. Schulz, L. Y. Lin, M. C. Beard and J. M. Luther, *Sci. Adv.*, 2017, **3**, 10–18.

180 Q. Wang, Z. Jin, D. Chen, D. Bai, H. Bian, J. Sun, G. Zhu, G. Wang and S. Liu, *Adv. Energy Mater.*, 2018, **8**, 1800007.

181 J. Wei, H. Li, Y. Zhao, W. Zhou, R. Fu, Y. Leprince-Wang, D. Yu and Q. Zhao, *Nano Energy*, 2016, **26**, 139–147.

182 L. Tan, C. Wang, M. Zeng and L. Fu, *Small*, 2017, **13**, 1603337.

183 S. N. Habisreutinger, T. Leijtens, G. E. Eperon, S. D. Stranks, R. J. Nicholas and H. J. Snaith, *Nano Lett.*, 2014, **14**, 5561–5568.

184 X. Ding, H. Chen, Y. Wu, S. Ma, S. Dai, S. Yang and J. Zhu, *J. Mater. Chem. A*, 2018, **6**, 18258–18266.

185 K. Wang, Z. Jin, L. Liang, H. Bian, D. Bai, H. Wang, J. Zhang, Q. Wang and S. Liu, *Nat. Commun.*, 2018, **9**, 4544.

186 Z. Chen, J. J. Wang, Y. Ren, C. Yu and K. Shum, *Appl. Phys. Lett.*, 2012, **101**, 093901.

187 S. Gupta, T. Bendikov, G. Hodes and D. Cahen, *ACS Energy Lett.*, 2016, **1**, 1028–1033.

188 F. Wang, J. L. Ma, F. Y. Xie, L. K. Li, J. Chen, J. Fan and N. Zhao, *Adv. Funct. Mater.*, 2016, **26**, 3417–3423.

189 M. H. Kumar, S. Dharani, W. L. Leong, P. P. Boix, R. R. Prabhakar, T. Baikie, C. Shi, H. Ding, R. Ramesh, M. Asta, M. Graetzel, S. G. Mhaisalkar and N. Mathews, *Adv. Mater.*, 2014, **26**, 7122.

190 W. Li, J. Li, J. Li, J. Fan, Y. Mai and L. Wang, *J. Mater. Chem. A*, 2016, **4**, 17104–17110.

191 D. Sabba, H. K. Mulmudi, R. R. Prabhakar, T. Krishnamoorthy, T. Baikie, P. P. Boix, S. Mhaisalkar and N. Mathews, *J. Phys. Chem. C*, 2015, **119**, 1763.
192 K. P. Marshall, M. Walker, R. I. Walton and R. A. Hatton, *Nat. Energy*, 2016, **1**, 16178.
193 T. Krishnamoorthy, H. Ding, C. Yan, W. L. Leong, T. Baikie, Z. Zhang, M. Sherburne, S. Li, M. Asta, N. Mathews and S. G. Mhaisalkar, *J. Mater. Chem. A*, 2015, **3**, 23829–23832.
194 Q. Sun, H. Chen and W.-J. Yin, *Chem. Mater.*, 2019, **31**, 244–250.
195 X.-G. Zhao, J.-H. Yang, Y. Fu, D. Yang, Q. Xu, L. Yu, S.-H. Wei and L. Zhang, *J. Am. Chem. Soc.*, 2017, **139**, 2630–2638.
196 W. Zhao, Z. Yao, F. Yu, D. Yang and S. Liu, *Adv. Sci.*, 2018, **5**, 1700131.
197 S. Zou, Y. Liu, J. Li, C. Liu, R. Feng, F. Jiang, Y. Li, J. Song, H. Zeng, M. Hong and X. Chen, *J. Am. Chem. Soc.*, 2017, **139**, 11443–11452.
198 M. Abdi-Jalebi, Z. Andaji-Garmaroudi, S. Cacovich, C. Stavrakas, B. Philippe, J. M. Richter, M. Alsari, E. P. Booker, E. M. Hutter, A. J. Pearson, S. Lilliu, T. J. Savenije, H. Rensmo, G. Divitini, C. Ducati, R. H. Friend and S. D. Stranks, *Nature*, 2018, **555**, 497–501.
199 J.-W. Lee, D.-H. Kim, H.-S. Kim, S.-W. Seo, S. M. Cho and N.-G. Park, *Adv. Energy Mater.*, 2015, **5**, 1501310.
200 J. Liang, Z. Liu, L. Qiu, Z. Hawash, L. Meng, Z. Wu, Y. Jiang, L. K. Ono and Y. Qi, *Adv. Energy Mater.*, 2018, **8**, 1800504.
201 Y. Zhao, Y. Wang, J. Duan, X. Yang and Q. Tang, *J. Mater. Chem. A*, 2019, **7**, 6877–6882.
202 C. F. J. Lau, X. Deng, J. Zheng, J. Kim, Z. Zhang, M. Zhang, J. Bing, B. Wilkinson, L. Hu, R. Patterson, S. Huang and A. Ho-Baillie, *J. Mater. Chem. A*, 2018, **6**, 5580–5586.
203 C. Liu, W. Li, H. Li, H. Wang, C. Zhang, Y. Yang, X. Gao, Q. Xue, H. -L. Yip, J. Fan, R. E. I. Schropp and Y. Mai, *Adv. Energy Mater.*, 2019, **9**, 1803572.
204 Z. Guo, S. Zhao, A. Liu, Y. Kamata, S. Teo, S. Yang, Z. Xu, S. Hayase and T. Ma, *ACS Appl. Mater. Interfaces*, 2019, **11**, 19994–20003.
205 W. Xiang, Z. Wang, D. J. Kubicki, W. Tress, J. Luo, D. Prochowicz, S. Akin, L. Emsley, J. Zhou, G. Dietler, M. Grätzel and A. Hagfeldt, *Joule*, 2019, **3**, 205–214.
206 W. S. Subhani, K. Wang, M. Du, X. Wang and S. Liu, *Adv. Energy Mater.*, 2019, **9**, 1803785.
207 Z. Wang, A. K. Baranwal, M. A. Kamarudin, Y. Kamata, C. H. Ng, M. Pandey, T. Ma and S. Hayase, *J. Mater. Chem. A*, 2019, DOI: 10.1039/C9TA05556H.
208 A. Swarnkar, W. J. Mir and A. Nag, *ACS Energy Lett.*, 2018, **3**, 286–289.
209 R. E. Brandt, V. Stevanovic, D. S. Ginley and T. Buonassisi, *MRS Commun.*, 2015, **5**, 265.
210 M. I. Saidaminov, J. Kim, A. Jain, R. Quintero-Bermudez, H. Tan, G. Long, F. Tan, A. Johnston, Y. Zhao, O. Voznyy and E. H. Sargent, *Nat. Energy*, 2018, **3**, 648–654.
211 J. T.-W. Wang, Z. Wang, S. Pathak, W. Zhang, D. W. deQuilettes, F. Wisnivesky-Rocca-Rivarola, J. Huang, P. K. Nayak, J. B. Patel, H. A. M. Yusof, Y. Vaynzof, R. Zhu, I. Ramirez, J. Zhang, C. Ducati, C. Grovenor, M. B. Johnston, D. S. Ginger, R. J. Nicholas and H. J. Snaith, *Energy Environ. Sci.*, 2016, **9**, 2892–2901.
212 H. S. Kim, C. R. Lee, J. H. Im, K. B. Lee, T. Moehl, A. Marchioro, S. J. Moon, R. Humphry-Baker, J. H. Yum, J. E. Moser, M. Gratzel and N. G. Park, *Sci. Rep.*, 2012, **2**, 591.
213 D. Bai, H. Bian, Z. Jin, H. Wang, L. Meng, Q. Wang and S. Liu, *Nano Energy*, 2018, **52**, 408–415.
214 M. Liu, M. B. Johnston and H. J. Snaith, *Nature*, 2013, **501**, 395–398.
215 M. Wang, P. Zeng, S. Bai, J. Gu, F. Li, Z. Yang and M. Liu, *Sol. RRL*, 2018, **2**, 1800217.
216 P. Teng, X. Han, J. Li, Y. Xu, L. Kang, Y. Wang, Y. Yang and T. Yu, *ACS Appl. Mater. Interfaces*, 2018, **10**, 9541–9546.
217 Q. A. Akkerman, M. Gandini, F. D. Stasio, P. Rastogi, F. Palazon, G. Bertoni, J. M. Ball, M. Prato, A. Petrozza and L. Manna, *Nat. Energy*, 2016, **2**, 16194.
218 J. B. Hoffman, G. Zaiats, I. Wappes and P. V. Kamat, *Chem. Mater.*, 2017, **29**, 9767–9774.
219 A. Barrows, A. Pearson, C. Kwak, A. Dunbar, A. Buckley and D. Lidzey, *Energy Environ. Sci.*, 2014, **7**, 2944–2951.
220 X. Xia, W. Wu, H. Li, B. Zheng, Y. Xue, J. Xu, D. Zhang, C. Gao and X. Liu, *RSC Adv.*, 2016, **6**, 14792–14798.
221 X. Liu, X. Tan, Z. Liu, H. Ye, B. Sun, T. Shi, Z. Tang and G. Liao, *Nano Energy*, 2019, **56**, 184–195.
222 W. E. I. Sha, X. Ren, L. Chen and W. C. H. Choy, *Appl. Phys. Lett.*, 2015, **106**, 221104.
223 W. Shockley and H. J. Queisser, *J. Appl. Phys.*, 1961, **32**, 510.
224 T. Tiedje, E. Yablonovitch, G. D. Cody and B. G. Brooks, *IEEE Trans. Electron Devices*, 1984, **31**, 711–716.
225 H. R. Stuart and D. G. Hall, *J. Opt. Soc. Am. A*, 1997, **14**, 3001–3008.
226 R. T. Ross, *J. Chem. Phys.*, 1967, **46**, 4590–4593.
227 A. Braun, E. A. Katz, D. Feuermann, B. M. Kayes and J. M. Gordon, *Energy Environ. Sci.*, 2013, **6**, 1499–1503.
228 W. E. I. Sha, H. Zhang, Z. S. Wang, H. L. Zhu, X. Ren, F. Lin, A. K.-Y. Jen and W. C. H. Choy, *Adv. Energy Mater.*, 2018, **8**, 1701586.
229 P. Zhu, C. Chen, S. Gu, R. Lin and J. Zhu, *Sol. RRL*, 2018, **2**, 1700224.
230 J. Shi, X. Xu, D. Li and Q. Meng, *Small*, 2015, **11**, 2472–2486.
231 Z. Guo, S. Teo, Z. Xu, C. Zhang, Y. Kamata, S. Hayase and T. Ma, *J. Mater. Chem. A*, 2019, **7**, 1227–1232.
232 H. Tan, A. Jain, O. Voznyy, X. Lan, F. P. G. de Arquer, J. Z. Fan, R. Quintero-Bermudez, M. Yuan, B. Zhang, Y. Zhao, F. Fan, P. Li, L. N. Quan, Y. Zhao, Z.-H. Lu, Z. Yang, S. Hoogland and E. H. Sargent, *Science*, 2017, **355**, 722–726.
233 Y. Xiao, G. Han, Y. Li, M. Li and J. Wu, *J. Mater. Chem. A*, 2014, **2**, 16856–16862.
234 S. Ito, S. Tanaka, K. Manabe and H. Nishino, *J. Phys. Chem. C*, 2014, **118**, 16995–17000.
235 G. S. Han, H. S. Chung, B. J. Kim, D. H. Kim, J. W. Lee, B. S. Swain, K. Mahmood, J. S. Yoo, N. G. Park, J. H. Lee and H. S. Jung, *J. Mater. Chem. A*, 2015, **3**, 9160–9164.
236 Y. Ogomi, K. Kukihara, Q. Shen, T. Toyoda, K. Yoshino, S. Pandey, H. Momose and S. Hayase, *ChemPhysChem*, 2014, **15**, 1062–1069.

237 M. Cha, P. Da, J. Wang, W. Wang, Z. Chen, F. Xiu, G. Zheng and Z.-S. Wang, *J. Am. Chem. Soc.*, 2016, **138**, 8581–8587.
238 Q. Li, J. Bai, T. Zhang, C. Nie, J. Duan and Q. Tang, *Chem. Commun.*, 2018, **54**, 9575–9578.
239 G. Wang, W. Dong, A. Gurung, K. Chen, F. Wu, Q. He, R. Pathak and Q. Qiao, *J. Power Sources*, 2019, **432**, 48–54.
240 Y. Liu, B. He, J. Duan, Y. Zhao, Y. Ding, M. Tang, H. Chen and Q. Tang, *J. Mater. Chem. A*, 2019, **7**, 12635–12644.
241 Y. Zhao, T. Liu, F. Ren, J. Duan, Y. Wang, X. Yang, Q. Li and Q. Tang, *Mater. Chem. Front.*, 2018, **2**, 2239–2244.
242 G. Liao, Y. Zhao, J. Duan, H. Yuan, Y. Wang, X. Yang, B. He and Q. Tang, *Dalton Trans.*, 2018, **47**, 15283–15287.
243 J. Tian, Q. Xue, X. Tang, Y. Chen, N. Li, Z. Hu, T. Shi, X. Wang, F. Huang, C. J. Brabec, H. -L. Yip and Y. Cao, *Adv. Mater.*, 2019, **31**, 1901152.
244 J. Feng, X. Zhu, Z. Yang, X. Zhang, J. Niu, Z. Wang, S. Zuo, S. Priya, S. Liu and D. Yang, *Adv. Mater.*, 2018, **30**, 1801418.